UCLA
UCLA Electronic Theses and Dissertations

Title

Characterization of the Interface of Optical Contact-Bonded Bulk Silicon

Permalink

Author

Pan, Frank

Publication Date

2020

Peer reviewed|Thesis/dissertation

UNIVERSITY OF CALIFORNIA

Los Angeles

Characterization of the Interface of Optical Contact-Bonded Bulk Silicon

A thesis submitted in partial satisfaction

of the requirements for the degree Master of Science

in Materials Science and Engineering

by

Frank Xuefeng Pan

2020

ABSTRACT OF THE THESIS

Characterization of the Interface of Optical Contact-Bonded Bulk Silicon

by

Frank Xuefeng Pan

Master of Science in Materials Science and Engineering

University of California, Los Angeles, 2020

Professor Bruce Dunn, Chair

Historically, silicon contact bonding has been used for silicon-on-insulator fabrication. However, there is little published research on contact bonding for bulk silicon applications. For these applications to be successful, contact bonding must be mechanically stable for bulk objects and a non-destructive characterization technique must be designed to evaluate bond quality. This report analyzes the tensile strength of two bonding processes, an alcohol-assisted (AA) and a direct-bonded (DB) process, and the potential of acoustic microscopy (AMI) to evaluate bond quality. Samples were aged in ambient for extended durations. In addition, some were annealed at 150ºC for 30 minutes to determine low-temperature annealing effects. DB samples held significantly higher loads than AA samples and consistently held above 2 MPa at room-temperature, which increased to 4 MPa after annealing. A linear correlation was ultimately found between AMI results and the tensile strengths of DB samples but not AA samples.

The thesis of Frank Xuefeng Pan is approved.

Jaime Marian

Mark S. Goorsky

Bruce Dunn, Committee Chair

University of California, Los Angeles

2020

Table of Contents

List of Figures

List of Tables

Acknowledgements

1. Introduction

Traditionally, the optical community has relied on optical adhesives to join optical components, such as beamsplitters and other multi-component assemblies. The ideal optical adhesive would be transparent in the wavelength range of interest, have a refractive index that minimizes reflection, and possess thermal and mechanical properties that are compatible with the optical assembly. Although many optical adhesives exist for the visible spectrum, few are compatible for the infrared (IR) spectrum due to excessive vibrational absorptions and low refractive index [1]. The lack of non-mechanical joining methods outside of the visible spectrum is a limiting factor in optical design. Contact bonding has the potential to remedy this issue. It is a technique that provides adhesion without additional adhesives between many classes of oxides, metals, and semiconductors [2], but is particularly effective between silica and silica-like surfaces. The lack of additional adhesives avoids vibrational absorption bands in the IR spectrum and eliminates issues with thermal and mechanical compatibility. A mixture of van der Waal's forces, hydrogen bonds, and/or capillary action provide initial adhesion [2] [3] [4]. Over time and with sufficiently high temperature, covalent bonds can form across the interface to provide near-bulk strengths [2] [5].

Contact bonding, also known as direct bonding, wafer bonding, and fusion bonding, has been used extensively in the semiconductor industry since the 1980s for semiconductor-on-insulator (SOI) fabrication [2] [6] [7]. The astronomy and space industries have also found use for contact bonding in the past. The Gravity Probe B used a form of this method, deemed hydroxide-catalyzed bonding, to bond its fused silica lenses [8]. This method has also found successful use in quasimonolithic mirror suspensions for ground-based gravitational wave (GW)

detectors, such as GEO600 and Advanced LIGO [9] [10]. Hydroxide-catalyzed bonding was also used in the ESA LISA Pathfinder mission for its optical bench interferometer [11]. There is currently commercial interest to expand the use of contact bonding to materials other than fused silica, such as silicon, to facilitate monolithic infrared optical assemblies, such as beamsplitters and beam combiners [12]. There is also interest in the development of silicon bonding for novel X-ray mirrors for space applications [13] [14]. In addition, a relatively new method deemed the alcohol-assisted (AA) method has gained traction in the space community [15]. This method utilizes alcohol on contacting surfaces to provide lubrication for alignment and reduce particulate matter on the surfaces. In all these methods, annealing steps were typically involved at temperatures ranging from 150-400°C to ≥800°C to achieve the highest bond strengths [2] [5] [16]. However, many optics applications often involve sensitive optical coatings that must avoid high temperature exposures to prevent degradation in optical properties. Thus, room- and low-temperature methods are essential for these applications.

Many of the applications for bulk silicon contact bonding are profoundly expensive and require confidence of successful operation over long lifetimes. For contact bonding to be widely adopted by the space and astronomy communities, a non-destructive evaluation technique is key. Characterization techniques for contact bonds have historically relied on acoustic microscopy, IR transmission, and x-ray reflectometry (XRR) [2]. However, IR transmission requires specific sample geometry to provide an entrance and exit for infrared light, which means it cannot be used as a general characterization tool for contact-bonded parts. Meanwhile, XRR is limited by the penetrating power of the instrument and cannot sample buried interfaces of bulk parts [17]. Acoustic microscopy remains a promising method. Like XRR, it has shown successful qualitative characterization of interfacial defects such as trapped particles, gas bubbles, and voids

in bonded silicon wafers. However, it also has the capability of sampling buried interfaces well below the surface.

For contact-bonded silicon assemblies to be used in space, it is critically important that they reliably meet strength capabilities to survive launch and avoid degradation over the lifetime of the satellite. This thesis will compare the tensile load capacity of an alcohol-assisted (AA) process to the traditional direct-bond (DB) process for bulk silicon parts to assess the viability of contact bonding for infrared sensor applications. Each process is examined over several weeks of aging to determine strength trends over time. A short, low-temperature annealing procedure is also performed for each process to ascertain whether significant strength increases can be obtained in a temperature range that is tolerable for coated optics. Acoustic microscopy is used as a non-destructive characterization technique to probe interface quality. A spring model of the bonded interface was used to quantify acoustic microscopy results in terms of interfacial stiffness. Acoustic microscopy results were then compared to sample tensile strength to determine whether there was sufficient correlation to recommend use of this non-destructive method to assess high-value optical assemblies. Through these experiments, we hope to answer pertinent questions on the reliability and mechanical stability of two contact bond methods for bulk silicon parts and demonstrate an effective non-destructive method of evaluating tensile strengths of these parts.

2. Background and Theory

2.1 Contact Bonding

2.1.1 Reported Strengths in Literature

Due to the prevalence of contact bonding for silicon wafers, most of the existing body of literature focuses on strengths of thin wafers. In this regard, Maszara's method of crack propagation by razor blade is considered the standard for evaluating the strength of the contact bond [18]. His method applied existing equations for crack propagation in a cleaved sample of linearly elastic solid to experimentally find the surface energy of the contacted interface. Figure 1 and the following equation show this methodology.
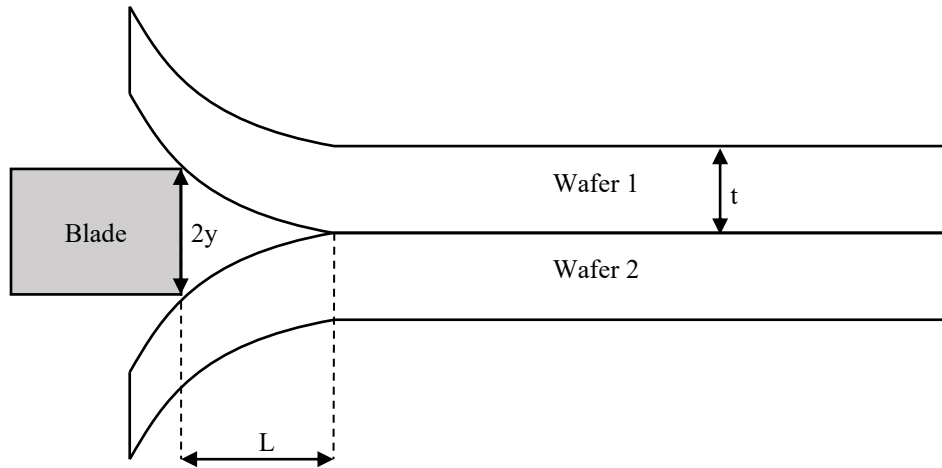
Figure 1. Graphic representation of Maszara's crack propagation method for evaluation of contact-bonded silicon wafers.

$$\gamma = \frac{3Et^3y^2}{8L^4}$$

1

where γ is the surface energy of the bonded part, E is the elastic modulus, t is wafer thickness, 2y is blade height, and L is crack length [18].

As the wafer thickness, blade height, and elastic modulus are known values, crack length is the only unknown value, which can be easily found by image analysis. Conveniently, bonding

energy can also be calculated for van der Waals force, capillary force, and other contributions through established theory, allowing for meaningful comparison and discussion. Through surface energy experiments, reports have shown that contact-bonded hydrophilic silicon wafers exhibited low strengths without a high-temperature annealing step [2] [4].

Unfortunately, the Maszara crack method cannot be easily applied to bulk samples due to differences in sample stiffness. In addition, the crack propagation method does not adequately answer questions on bulk mechanical stability as it involves a different failure mode from those likely experienced in space applications. Instead, this report will rely on standard flatwise tension pull tests. There is some literature measuring the tensile strength of contacted silicon wafers [13] [19]. Muller and Stoffel analyzed the tensile strengths of bonded silicon wafers as a function of annealing temperature and annealing time. They found that increasing annealing time at 200°C from 1 hour to 4 hours resulted in a ~10 MPa increase in bond strength [19]. Although Muller did not examine room-temperature bonds, they did find that samples annealed at 200°C for merely 30 minutes achieved tensile loads of ~5 MPa (1.45 ksi). Similarly, preliminary results from Girou *et al.* showed a ~4x increase in tensile strength of contacted silicon wafers upon annealing at 200°C for 65 hours in comparison to room temperature samples [13].

2.1.2   Surface Requirements

Contact bonding requires three conditions of the sample surfaces: cleanliness, flatness, and smoothness. Organic contamination can be particularly detrimental as it limits the areas of intimate silicon-silicon contact and can contribute to the development of interfacial bubbles, or voids, over time**.** Muller and Stoffel showed that standard wafer cleaning methods, like RCA, are suitable for addressing contamination [19]. Low-power plasma treatments have also been very

effective in reducing carbon contamination [20]. These surface treatments also have the added

benefit of turning the silicon surface hydrophilic, resulting in a silanol-saturated surface that

forms the basis for eventual covalent bond formation across the contacted interface [21].

Smoothness and flatness requirements are determined by the need for intimate contact to

facilitate the formation of covalent bonds. Maszara *et al.* suggests typical surface roughness

values of prime grade silicon wafers is adequate for intimate wafer contact [22]. In wafer

research, flatness was less of a concern due to the flexible nature of thin wafers. However, bulk

samples are rigid, thus requiring a certain degree of flatness. Tong *et al.* experimentally showed

that a flatness of $\lambda/10$ (~63 nm), as measured in an optical interferometer, was sufficient to

establish contact for 20mm-thick Si parts of 100mm diameter [23]. Even with strict surface

roughness and flatness parameters, it is likely improbable for a contacted sample to experience

intimate contact across the whole surface. Although previous literature has cited large areas of

contact through various evaluation techniques, contact mechanics dictates distinct points of

intimate contact and non-contact due to microscopic surface topography [2] [24].
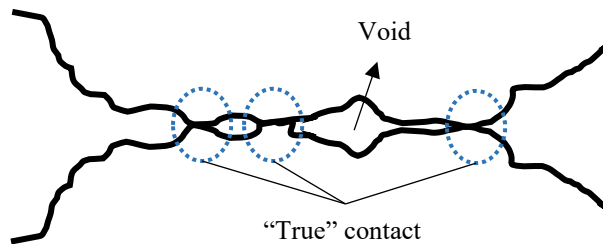
Figure 2. Graphic representation of "true" contact between surfaces with inherent micro-roughness.

It is commonly understood that the area of "true" contact is significantly smaller than the

apparent area of contact [24]. This behavior must be considered in subsequent discussion

regarding adhesion mechanisms that rely on contact area. In addition, it prevents the

extrapolation of tensile strength from measured tensile loads, as the area of true contact cannot be accurately measured.

2.1.3   *Influence of Particles*

Bulk silicon differs from silicon wafers in several key mechanical ways due to different elastic deformation and stiffness considerations from their thicknesses. One important impact of thickness is in the way contacting surfaces behave with gaps and particles. Tong and Gosele laid out the relevant theory in several reports [23]. Gaps may occur from surface waviness, which is a quasi-periodic element of surface roughness that is commonly caused by machining and processing, or particles residing in the interface. These gaps may close only if there is sufficient surface energy from the bonded pair to match the elastic deformation required to do so. Figure 3, below, shows the relevant geometric considerations involved.
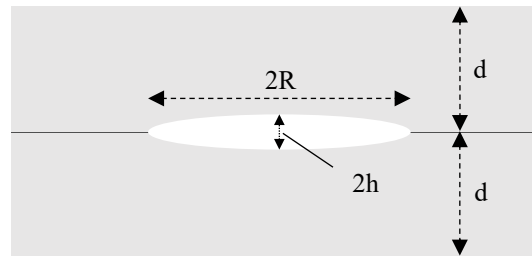
Figure 3. Graphic representation of an interfacial gap between two contacted silicon parts.

Following Figure 3, if the radius of the gap is less than the total thickness of the bonded pair $(R < 2d)$, then the maximum height of a gap that can be closed can be found with the following inequality:

$$h < 2.6 \sqrt{\frac{R\gamma}{E}} \qquad\qquad 2$$

where h is half the gap height, E is Young's modulus, and γ is the surface energy of the bonded pair [23].

7

However, if $R > 2d$, then gap closure depends on sample thickness [23]:

$$h = \frac{R^2}{\sqrt{\frac{1.2Ed^3}{\gamma}}}$$

3

For very thick parts, the ratio of height to radius for closeable gaps becomes smaller. Since many gaps are controlled by surface waviness and micro-roughness, Figure 4, which uses the equations above, can provide an indication to the surface quality necessary for bulk parts of certain thicknesses. In this report, silicon parts had an individual thickness of 0.25", or ~6 mm. Thus, to close gaps smaller than 0.1 mm in radius, gap heights must be $< 0.06\ \mu m$ (60 nm) from the figure below. Hence, surface flatness requirements are crucial to ensure well-contacted parts.
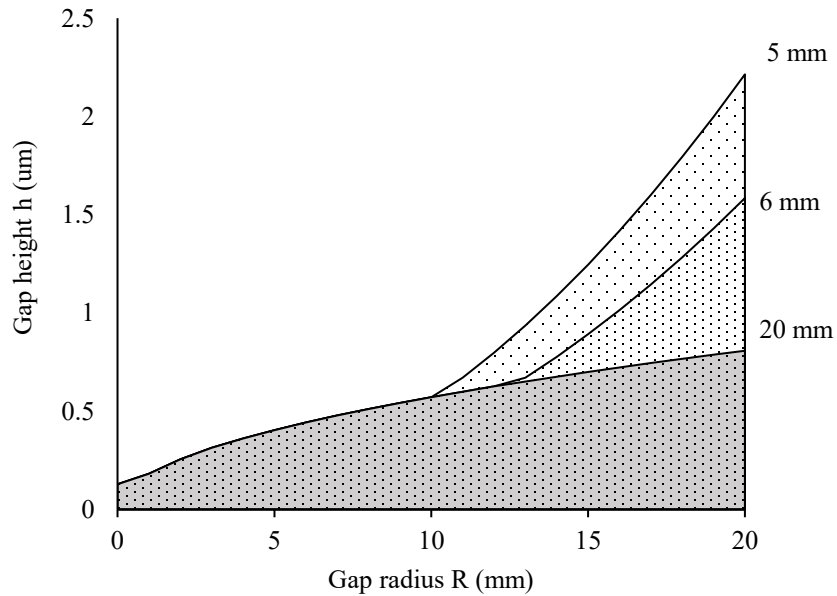
Figure 4. Plot of maximum gap height for given gap radii and sample thicknesses. Shaded regions represent gaps that can be closed by a silicon sample with $E = 1.66 \times 10^{11}\ \left[\frac{N}{m^2}\right]$ and $\gamma = 0.8\ \left[\frac{J}{m^2}\right]$ [23] [25].

2.2   Interface Interactions

For both direct-bonded and alcohol-assisted processes, a mixture of van der Waals forces, hydrogen bonds, and capillary action provide adhesion upon initial contact of smooth, flat surfaces [2]. Over time, several reactions can occur at the interface that lead to the development of siloxane (Si-O-Si) bonds, interfacial water, and hydrogen gas. Siloxane bonds theoretically provide bulk strengths. Facilitating their development generally requires annealing at $\geq 150°C$ for long periods [2]. The initial mechanisms for adhesion will be discussed first, followed by a discussion on siloxane bond development.

2.2.1   Van der Waals Force

Intimate contact of any two surfaces involves van der Waals forces. In an ideal parallel plate model, the adhesive pressure can be found by the following [26]:

$$F_{vdW} = -\frac{A}{6\pi d^3} \left[\frac{N}{m^2}\right] \qquad 4$$

where F_{vdW} is van der Waals force, A is the Hamaker constant and d is the gap distance.

Negative force indicates attraction and positive force indicates repulsion. In the case of contact bonding, the two plates can be taken as silica due to the native oxide layer present on contacting silicon surfaces, and the adjoining medium may either be approximated by air or water. The plot below shows attractive force for both media.
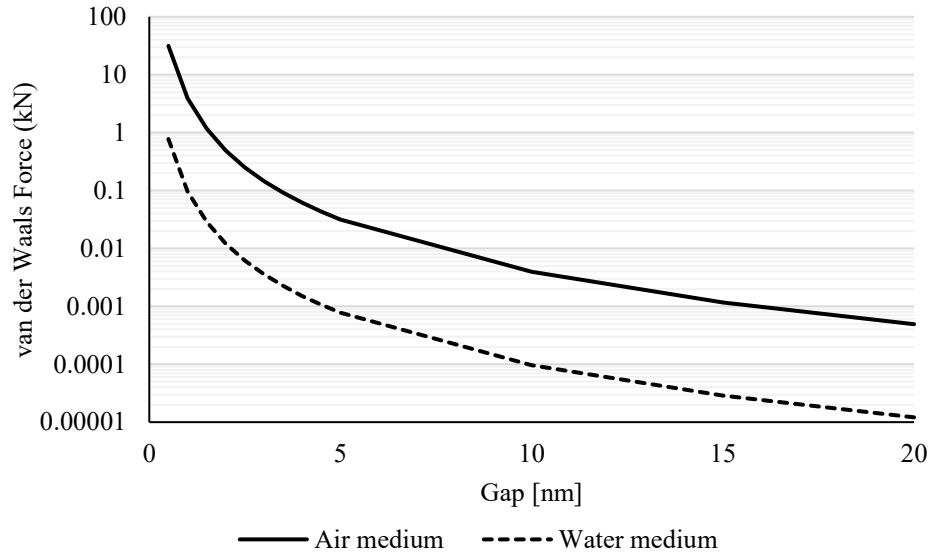
Figure 5. Log plot of van der Waals force over gap distance with area of 38 mm (1.5") diam. samples used in this study. Force axis is plotted in log scale. $A_{air} = 6.5 * 10^{-20}[J]$ [26]. $A_{water} = 1.6 * 10^{-21}[J]$ [27].

Figure 5 shows the attractive force in an air medium is an order of magnitude larger than the force in a water medium. It also shows the large reduction in force with increasing gap distance. At 2 nm, assuming a 38 mm (1.5") diam surface, van der Waals force would only be ~500 N (110 lbf.) in air. However, if the surfaces are only separated by 1 nm, van der Waals forces can account for a significant ~4000 N (885 lbf.) in air, but only 100 N (21 lbf.) in water. At the length scale of angstroms, the contacting surfaces can no longer be considered perfectly flat. Thus, this estimation should not be applied directly to contact-bonded parts. However, it does provide insight into the strength contributions that van der Waals forces may provide. Given that there is likely several monolayers of adsorbed water on the contacting surfaces, it is likely safer to approximate the interface with a water medium than an air medium. This suggests the strength contributions of van der Waals forces may be minimal compared to other contributors for hydrophilic samples.

10

2.2.2 Capillary Force

Capillary forces also likely play a role in hydrophilic samples. Due to the natural presence of water, hydrophilic silicon surfaces have an abundant amount of adsorbed -OH groups on the surface. These -OH groups can either come from surface water that is naturally present in ambient atmosphere, or from a purposeful DI water rinse after cleaning and activating the surface [28]. Farrens *et al.* and Asay *et al.* have shown several monolayers of water exist on hydrophilic silicon surfaces in an ambient environment [20] [28]. The interfacial water that is present may contribute capillary forces that keep the bonding surfaces together [29]. In the ideal case of two parallel plates and a flooded interface, capillary force is inversely proportional to the height of the gap that separates the two plates [30] [31].
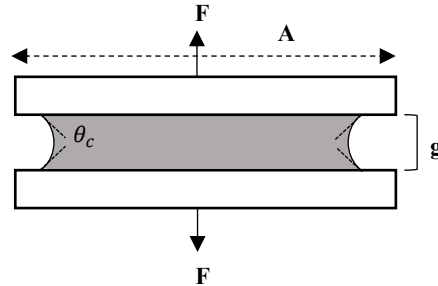
Figure 6. Graphic of capillary force for two parallel plates.

$$F_c = -\Delta p_{la} A = \frac{2A\gamma_{la}\cos(\theta_c)}{g} \ [N] \qquad\qquad 5$$

where F_c is capillary force, A is contact area, g is gap distance, γ is surface tension of liquid-air interface, and θ_c is the contact angle [30].

As contact bonding requires a high degree of surface smoothness and flatness, the gap height is most likely on the order of single nanometers. For plasma-cleaned samples, the contact angle can be assumed to be negligible. Thus, the capillary force is dependent on area of contact,

11

gap height, and the liquid-gas interface. As the gap height is only a few nanometers, capillary

force can be substantial and may explain some behavior shown in the results. The plot below

assumes a gap of 2 nm and takes water-air and isopropyl alcohol-air as the two liquid-gas

environments. The maximum sample area is the surface area of the 38 mm (1.5") dia. silicon

samples used in this study. If the whole surface is wetted, capillary force could attribute up to

25,000 N (5600 lbf) for isopropyl alcohol or 82,000 N (18,000 lbf) for water.
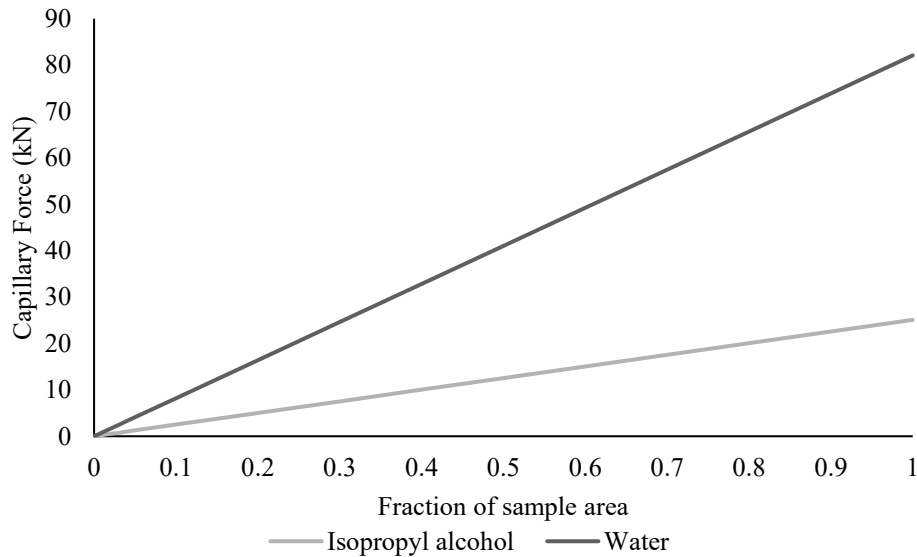
Figure 7. Plot of capillary force over wetted area assuming a gap of 2 nm. 38 mm (1.5") dia. samples were used to

determine max sample area. $\gamma_{IPA} = 0.022 \left[\frac{N}{m}\right] at\ 25^oC$ [32]. $\gamma_{water} = 0.072 \left[\frac{N}{m}\right] at\ 25^oC$ [32].

Although capillary force is a straightforward calculation for the ideal case, literature has

shown that nanochannel gap distances like those seen in contact bonding adds further complexity

[28] [33] [34]. These complexities will be discussed in Section 7.1.

2.2.3 Hydrogen Bonds and Siloxane Formation

At angstrom gap scales with a small volume of water, it becomes more pertinent to

discuss the interactions of water and contacting surfaces in terms of hydrogen bonds rather than

capillary forces. When two hydrophilic silicon surfaces are placed into contact, hydrogen bonds form across the interface between the silanol groups on the surface and the monolayers of water in the interface. However, these bonds may not be in their most stable positions. Over time, even at room temperature, they may adjust to reach their most stable structures [2]. Existing literature has surmised that hydrogen bonds are responsible for the strength of silicon contact bonds at room temperature [2].

Given sufficient time and elevated temperature, a condensation reaction can occur among the intimately contacted silanol groups at the bond surfaces that leads to siloxane bonding across the interface. It is important to note that this reaction most likely occurs only at points where silanol groups are in appropriate proximity for bonding.

$$Si - OH + HO - Si \leftrightarrow Si - O - Si + HOH \qquad\qquad 6$$
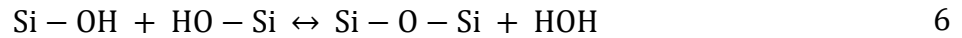
At room temperature, adsorbed interfacial water is present that limits the forward reaction. Below ~400°C, this reaction is reversible [2] [5]. Thus, excess water in the interface can react with siloxane and negatively affect bond strength.

However, some interfacial water will diffuse away from the interface, either through the native oxide or laterally across the interface [2] [16] [35]. As the water diffuses out of the interface, the reaction is driven forward, creating more siloxane bonds across the interface. Water that diffuses through the native oxide reacts with native silicon and creates additional oxide as well as hydrogen gas:

$$Si + 2HOH \leftrightarrow Si - O - Si + 2H_2 \qquad\qquad 7$$
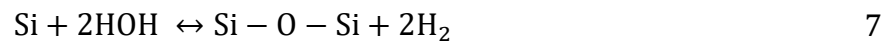
It is important to note that the siloxane in the above reaction is below the native oxide layer of a silicon sample, not across the interface. Hydrogen gas created from this reaction can

diffuse quickly up through the native oxide and enter the bond interface, creating bubbles that deform contacting surfaces out of contact. However, not all samples develop distinct bubbles. Tong suggests hydrocarbon contamination in the interface may also desorb at elevated temperatures and act as nucleation points for bubble development [21].
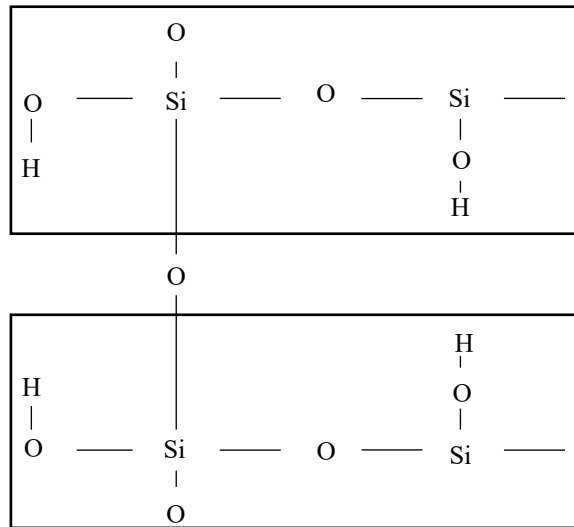
Figure 8. Graphic representation of siloxane bonds forming from two silica surfaces with adsorbed -OH groups.

2.3   Contact Bonding Methods

A large portion of recent work regarding bulk contact bonding has focused on silica glass using a hydroxide-catalyzed bond method. This involves a solution of hydroxide ions to etch contacting oxide surfaces and saturate the bond surfaces with –OH groups [5]. These surfaces are thought to undergo Equation 6 and form an oxide bond between surfaces. The presence of silanol groups at the bond surfaces is crucial for the development of siloxane bonds and thus the strength of the contact bond. The Gravity Probe B, a-LIGO, and GEO600 gravitational-wave detectors all used this method to bond fused silica [9] [10] [11].

For silicon samples, much of the contact bonding literature has stemmed from silicon wafer bonding [2]. In these applications, the traditional bonding method has been named the

"direct bond" method, wherein the surfaces are cleaned either by traditional RCA methods or by a low-power oxygen plasma and contacted in a cleanroom environment [21]. Plasma-treated surfaces showed higher bond strengths at low temperatures compared to RCA cleaned surfaces [16]. Typically, this was followed by annealing $\geq 150^{o}C$ to facilitate siloxane bond formation by Equation 6 [16]. In this thesis, the plasma treatment variation is referred to simply as the "direct bond" (DB) method.

Recently, there have been reports of a new variation on the direct bond method involving the use of alcohol in the interface [15]. In the traditional method, spontaneous bonding typically occurred immediately upon contact [2] [36]. The exact mechanisms responsible for spontaneous bonding are currently unclear but are likely linked to electrostatic effects [36]. Although spontaneous bonding is advantageous for initial strengths, it leads to difficulties in precision alignment of parts. The introduction of alcohol, like isopropyl alcohol (IPA), addresses this issue by acting as a lubricant that prevents spontaneous bonding. Thus, the alignment step can be greatly simplified. Eventually, the alcohol should evaporate out of the interface and intimate surface contact can be established [15]. In this thesis, the alcohol variation is referred to as the "alcohol-assisted" (AA) method.

In all these methods, the underlying chemistry still relies on siloxane bond formation by Equation 6 to establish the highest bond strengths. Literature has suggested that a low-temperature anneal of 110-150°C can further drive the condensation reaction forward by forcing the existing interfacial water to evaporate out of the interface [2]. However, bulk strengths were not experimentally seen until temperatures of ≥ 800°C [2]. Current literature attributes this high-temperature behavior to the development of larger "true" contact area through viscous flow of the native oxide layer [2] [3]. However, sensitive optical coatings cannot be subjected to high

temperatures, so this paper will only focus on strength at room temperature (RT) and from low-temperature annealing.

2.4 Fourier-Transform Infrared Spectroscopy

FTIR spectroscopy is a common spectral technique that uses unique absorbance signatures in the infrared spectrum to identify chemical species. For silicon contact-bonded samples, a multiple internal transmission (MIT) setup is commonly employed to maximize absorption signals from the thin interface [37]. In an MIT setup, the sample edges are beveled to 45° to allow coupling of infrared light. As the light experience's total internal reflection at the outer surfaces, it passes through the interface multiple times. With each pass, the absorption contributions from the interface increase relative to the outer surfaces. In addition, species that are oriented parallel to the interface show weaker absorption signal in comparison to species oriented perpendicular to the interface [38]. Thus, the chemical species at the interface that contribute to bonding can be discerned. The sample geometries can be optimized to increase the amount of passes infrared light makes through the interface [37] [38]. Weldon *et al.* showed optimal geometries that maximize the signal intensity from the interface [38]. In this study, 1mm thick, 50x20 mm^2 silicon parts were joined together to allow 25 passes through the interface.
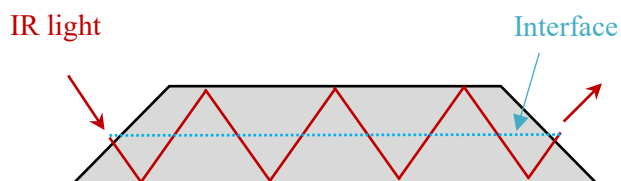
Figure 9. Graphic representation of a silicon sample in an MIT configuration.

Hydrophilic silicon samples should display absorption bands in the interface that correspond to several chemical species. Specifically, there should be silanol and adsorbed water

16

upon initial contact. In addition, there may be isopropyl alcohol, interstitial oxygen in the silicon lattice, and silicon hydride (Si-H). As discussed earlier, over time water can diffuse away from the interface and react with silicon to form hydrogen gas. At sufficient temperatures, silanol groups should also react with each other to form siloxane and additional water molecules. All these chemical species have distinct absorption bands in the infrared spectrum. Thus, FTIR can be used to distinguish interface evolution over time and annealing temperature.

Literature has already assigned many of the relevant absorption bands. However, the correct interpretation of these bands remains non-trivial. One of the more complex interactions involves the absorption bands of adsorbed surface water and silanol. These two chemical species share a broad absorption band at ~3300 cm^{-1} due to their shared -OH groups [39]. This broad band has been assigned to several -OH stretch modes that correspond to hydrogen-bonded, internal, terminal, and isolated -OH groups [39]. Furthermore, hydrogen bonding interactions add more complexity by shifting peak locations [37]. Although there is a large region of overlap between the two, Gallas *et al*. showed the two chemical species still have unique peaks that do not overlap with each other [39]. Silanol displays a broad absorption band from 4800-4200 cm^{-1} due to a combination of -OH stretching and bending modes. Meanwhile, water has a weak but sharp band at 1630 cm^{-1} due to its scissor mode [37] [39] [40].

Given the importance of siloxane bond formation, it would be ideal to follow the formation of siloxane bonds in the interface. However, the absorption bands associated with siloxane occur below 1000 cm^{-1}, which is beyond the transmission window of silicon that cuts off at ~1500 cm^{-1} [41]. Since these bands cannot be directly observed, the presence of siloxane in a bonded interface must be inferred. Following Equation 6, a decrease in silanol concentration may correspond to an increase in siloxane concentration.

Alcohol-assisted samples also have an additional layer of complexity due to the initial presence of isopropyl alcohol (IPA), which has its own -OH group that further complicates silanol and water interpretation. However, its hydrocarbon groups lead to very distinct absorption bands that do not conflict with the other chemical species of interest. Figure 10, taken in-house from IPA on a silicon surface, shows these hydrocarbon bands around ~2900-2800 cm^{-1} [42].

Table 1. Absorption bands of silanol, water, and IPA [39] [42].

	3520 cm^{-1}	Hydrogen-bonded OH stretch
ν(OH) [stretch]	3670 cm^{-1}	Internal OH stretch
	3710 cm^{-1}	Terminal OH stretch
	3745 cm^{-1}	Isolated OH stretch
$(\nu + \delta)$OH [stretch + bend]	4800-4200 cm^{-1}	Combination -OH stretch + bend. Specific to silanol
δH_2O [scissor]	1630 cm^{-1}	H-OH scissor bend. Specific to water
ν(CH$_x$) [stretch]	2900-2800 cm^{-1}	Hydrocarbon (CH$_2$, CH$_3$) stretch. Specific to isopropanol
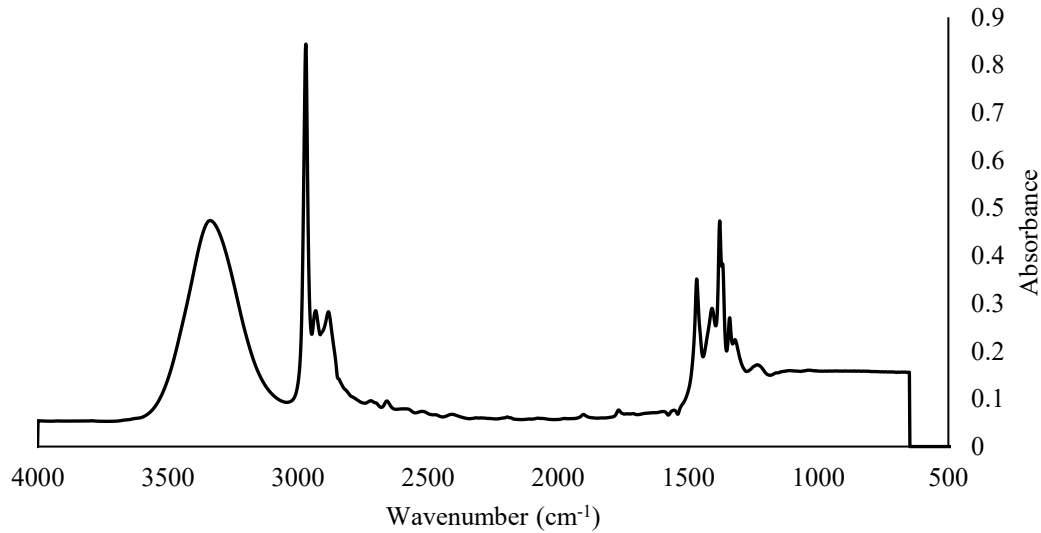
Figure 10. IR spectrum of IPA on silicon from 4000-400 cm^{-1}. The broad band centered around 3300 cm^{-1} is associated with the -OH group. The bands from 2900-2800 cm^{-1} are due to hydrocarbons and the bands from ~1500-1300 cm^{-1} are combination bands of -OH twist, C-O stretch, and CH$_3$ rocking modes [42].

2.5   Acoustic Microscopy

Acoustic microscopy is a common non-destructive evaluation technique that has been well-researched and commercialized for many years [7] [43]. In the existing contact bond literature, it has been used to image interfaces for trapped particles, interfacial bubbles, and areas out of contact [2]. In this technique, an acoustic pulse of a certain frequency is generated by a transducer and directed towards the sample. Water is typically used as a coupling medium for the acoustic wave. Due to the large refractive angle that occurs when the acoustic pulse transitions from water to silicon, there is a natural focal point that can be used to image the plane of the interface. The transmitted acoustic pulse will generate reflections whenever it encounters an impedance change. In a single transducer-receiver setup, the transducer transmits an acoustic signal and receives reflection signals from the top surface, the bonded interface, and the bottom

19

surface [21]. A full sample image can be generated by moving the transducer in a raster pattern. Each pixel in the raster corresponds to a finite area of the sample. The area size is dependent on the radius of the acoustic beam at the focal point. In other words, the resolution of this technique depends on the radius of the acoustic beam at the focal point.

Return signals for each surface are naturally discriminated in time as the velocity of the acoustic waves are constant but the distance from the reflecting surface to the transducer is not. Thus, by gating in time, it is simple to find the signal corresponding to the bonded interface. In Figure 11, the top surface reflection is green, the bond interface reflection is blue, and the bottom surface reflection is grey. In the case of a well-contacted sample, meaning intimate contact between surfaces and strong acoustic coupling, the reflected amplitude from the interface is minimal. However, for unbonded regions, either from gaps caused by trapped particles or gas bubbles, the reflection amplitude from the interface can be large. The amplitude of the reflection is dependent on any factors that impact impedance, such as gap height and the presence of liquid or gas.
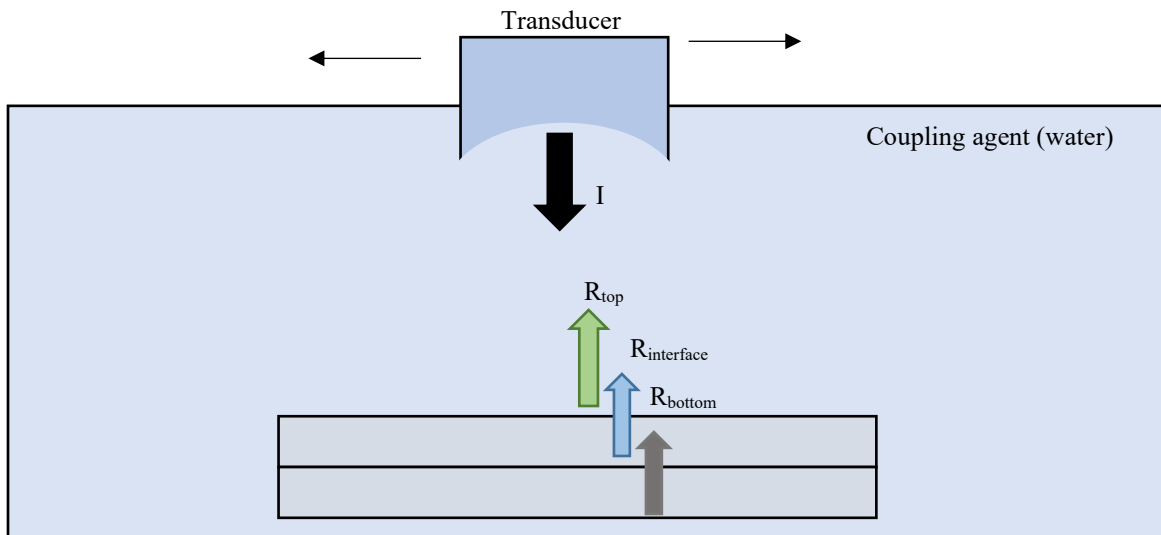
Figure 11. Graphic representation of acoustic microscopy in a single transducer setup.

The reflection signal from the bonded interface can be further separated into three separate signals that correspond to a pure longitudinal wave, a longitudinal-shear wave, and a pure shear wave. Shear waves are only supported in acoustically-solid materials, whereas longitudinal waves can be supported in liquids as well. The velocity of each is solely dependent on the material and is thus a fixed quantity. However, it is important to note that material crystal orientation does impact the velocity. Thus, orientation must be uniform across a bonded silicon interface to minimize any reflection signal derived from crystal orientation mismatch. Pure longitudinal waves travel faster than pure shear waves in solid materials, meaning time can still be used as a discriminant to assign the three reflection signatures from the interface.

In this study, a normalized color scale for reflected amplitude was used for qualitative sample evaluation. This color scale was normalized to the reflection amplitude of the top surface. In other words, the red areas (0 dB) represent areas where the signal amplitude from the bond interface matched the signal amplitude of the top surface. The black regions (-60 dB) represent areas that only had a return signal of 0.1% from the bonded interface, which translates to areas with good acoustic coupling between surfaces and may imply good contact.
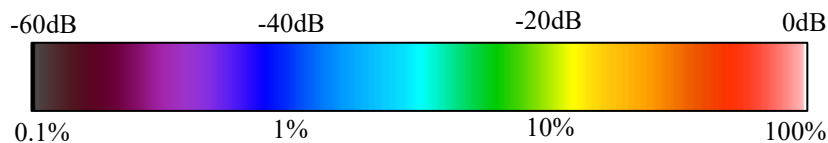
Figure 12. 60dB color scale for reflected amplitude normalized to the reflectance of a silicon-water interface. Darker regions correlate to well-contacted areas. Red regions correlate to poor or no contact. Regions in between suggest some form of acoustic coupling between surfaces, possibly through weak adhesion.

The normalized color scale was developed for simple qualitative inspection and is used here to represent the existing way in which acoustic microscopy has been used to characterize

contact-bonded samples. Any defects, such as particulates, create gaps that reflect acoustic

energy, making them easily identifiable with the color scale. However, its lack of quantitative

rigor makes sample comparison difficult.

2.5.1 Spring Model

The spring model explained here uses the longitudinal reflection signal from the interface

to quantify the degree of contact between surfaces. For a perfectly bonded interface of two

materials, the reflection coefficient is a simple calculation dependent on the impedance of the

two bonded materials [44] [45] [46]. Acoustic impedance is an inherent property of a medium

that is dependent on material density and speed of sound and commonly expressed in terms of

rayls: $z = \rho c \ [rayl]$, where a rayl is $\left[\frac{Pa*s}{m}\right]$ [44].

$$R = \frac{z_1 - z_2}{z_1 + z_2} \qquad\qquad 8$$

where R is reflection coefficient from the interface and z_x is acoustic impedance of the contacting materials.

If the two materials have the same acoustic impedance, as is the case of silicon-to-silicon

(of the same crystal orientation) contact bonding, then $z_1 = z_2$ and R= 0, so there will be no

acoustic return from the interface. However, if the interface is not perfectly bonded, this simple

equation must be modified to accommodate scatter from air gaps. To address this, Tattersall

developed a spring system to model a bonded interface [44].
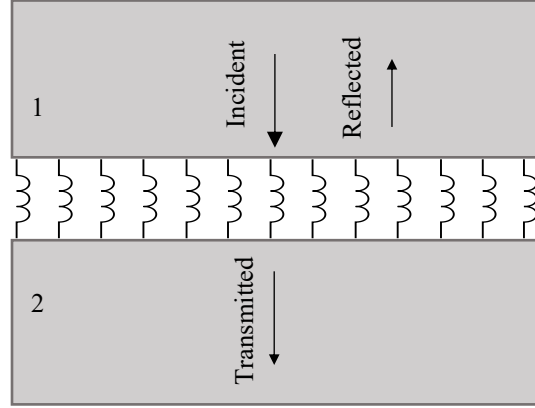
Figure 13. Graphic representation of spring model of a bonded interface wherein the springs are responsible for the reflected and transmitted acoustic waves.

Physically, the springs represent how the interface reacts to compressive stress. Tattersall recognized that an incident longitudinal wave would provide compressive stress that must be transmitted or reflected in the interface [44]. Assuming the springs are light and transmit stress instantaneously, the only parameter in a spring model that affects stress transmission is spring stiffness. Physically, wave transmission and reflection are dependent on the degree of contact between surfaces. The degree of contact is likely related to the degree of bonding present in the interface. Thus, the theoretical stiffness of the springs may correspond to the physical degree of bonding present in the interface. Stiffer springs correspond to a well-contacted interface and may possibly correspond to a well-bonded interface. Assuming stress from an incident longitudinal wave must be conserved between the two media and the interface ($\sigma_1 = \sigma_2 = \sigma_{int}$), Tattersall derived a new equation for reflection coefficient that includes spring stiffness [44].

$$R = \frac{z_1 - z_2 + i\omega(\frac{z_1 z_2}{K})}{z_1 + z_2 + i\omega(\frac{z_1 z_2}{K})} \qquad\qquad 9$$

where ω is the angular frequency of the wave and K is interfacial stiffness per unit area.

One may notice that for an infinitely stiff spring, Equation 9 simply becomes Equation 8, meaning infinite stiffness represents perfect bonding. Using the above equation, Drinkwater *et al.* showed that the amplitude of the reflection coefficient for identical materials ($z_1 = z_2$) can be simplified to the following [45]:

$$|R| = \frac{1}{\sqrt{1 + \left(\frac{2K}{\omega z}\right)^2}}$$

10

Thus, a given reflection amplitude from acoustic microscopy can be used to directly calculate interfacial stiffness.

If a perfectly bonded interface is defined physically as siloxane bonds bridging the entire interface, this model can be taken further by defining the siloxane bonds as a "thin film" between the two contacting surfaces. This "thin film" model can also be used to approximate the stiffness of other materials, such as liquid water.
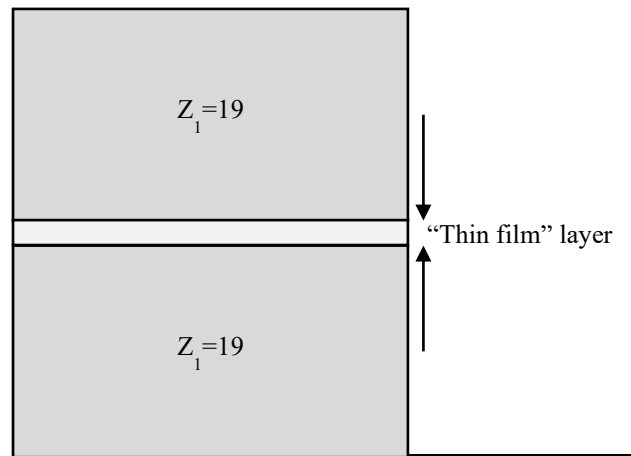
Figure 14. Graphic representation of a contact-bonded silicon sample with a "thin film" representing the interface.

By doing so, a realistic upper bound on interfacial stiffness per unit area can be found using the expression below [46] [47].

$$K_{max} = \frac{\rho c^2}{h} = \frac{B}{h} \qquad 11$$

Where K is the spring stiffness per unit area, h is the film thickness, c is speed of sound in the layer, ρ is the layer density, and B is the bulk modulus of the layer.

For a layer of siloxane, bulk silica values can be used to approximate density and speed of sound. Assuming an ideal siloxane layer thickness of 4.5 Å as a conservative estimate, max stiffness per unit area is $3.682 * 10^{20}$ $[\frac{Pa}{m}]$. At this stiffness, the lowest reflection amplitude should be roughly 0.0003%, which is essentially zero reflection given the sensitivity of most acoustic microscopy instruments. Thus, siloxane bonds likely correspond to near-zero reflection. However, near-zero reflection may not strictly correspond solely to siloxane bonds. The presence of van der Waals force, hydrogen bonds, and capillary forces may also correspond to near-zero reflection. Therefore, this method of acoustic analysis cannot be used to determine which areas of a contacted interface have siloxane bonds and which do not simply by mapping reflectance.

The stiffness found in Equation 10 represents the stiffness of a specific pixel. Since each pixel samples a different area of the interface, it follows that the total stiffness of the interface may be a summation of the stiffness of each pixel. Within each pixel, there are likely various interface features like voids, liquid, and asperity contact. Thus, the total stiffness may be thought of as a summation of the types of contact that exist in different areas of the interface

$$K_{total} = aK_{asperity} + bK_{liquid} + cK_{void} \qquad 12$$

The coefficients in Equation 12 represent fractional areal coverage of the interface for each term: thus, $a + b + c = 1$. Due to the unassigned coefficients, it is difficult in the current iteration of this method to determine the contribution of each term to the overall stiffness.

However, a simple ratio can be taken of measured stiffnesses from non-zero reflections and the maximum stiffness of a perfectly-bonded interface to determine the overall degree of slackness, or imperfection, in the interface. For a 25 MHz transducer and the impedance of silicon (~19.6 Mrayls [$\frac{MN*s}{m^3}$]), stiffness was calculated for a range of reflection amplitudes using Equation 10. A ratio of these stiffnesses to the maximum stiffness calculated earlier is plotted with reflectivity below.
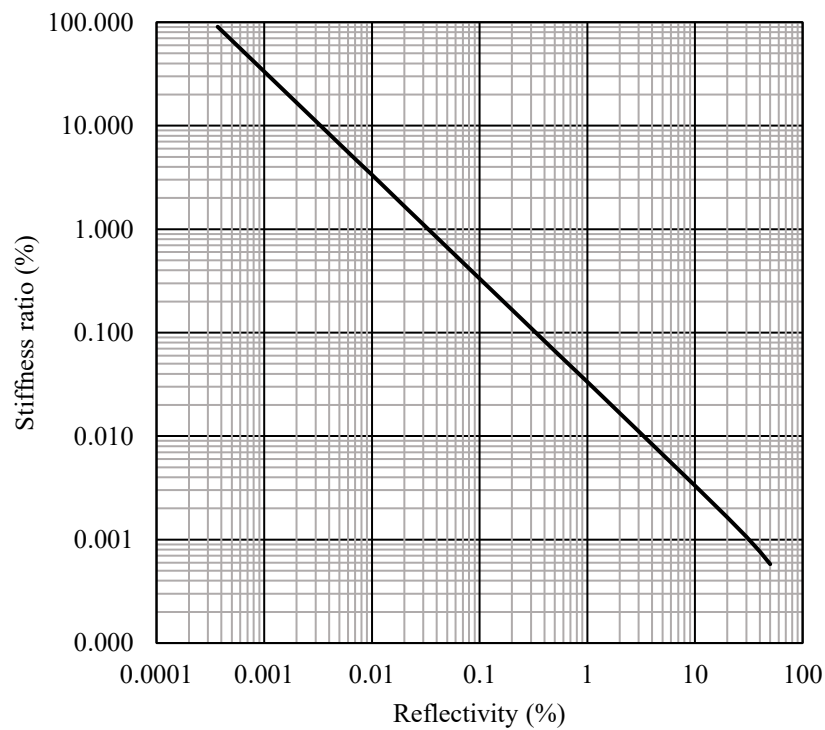
Figure 15. Log-log plot of a ratio of calculated stiffness to max stiffness over reflectivity.

3. Experimental

3.1 Surface Characterization

Czochralski (CZ) grown (100) silicon (38 mm dia., 6.35 mm thickness) specified to a flatness of $\lambda/10$ (~63 nm) RMS were obtained for bulk silicon experiments. A 4D Technology AccuFiz E100S Fizeau interferometer was used to characterize the silicon surfaces. Roughly one-third of the samples were slightly convex, and the rest were slightly concave. The deviation from flat was measured to be 2-20 nm RMS and the peak-to-valley was 40-160 nm. Figure 16 shows a sample surface pattern that was commonly seen in the batches used for this experiment. The high peak-to-valley is due to large-scale surface waviness rather than fine-scale surface micro-roughness.
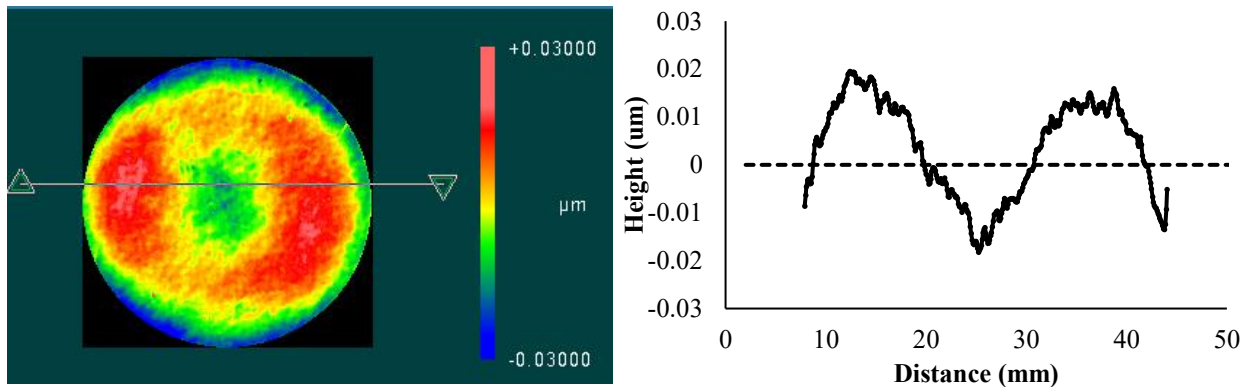
Figure 16. (Left) A visualization obtained from surface interferometry of a sample surface from directly above the surface. (Right) The cross-section view of the left image, where the x-axis follows the left image.

Previous experience with bulk silica suggests that only minimal pressure is needed to close 100 nm gaps over large spans between bonding surfaces. However, surface micro-roughness can cause fine-scale gaps that are more difficult to overcome. As a result, the "apparent contact" area may be much larger than the "true contact" area. This limits the amount

27

of siloxane bonds that can form across the interface [24]. Therefore, sample micro-roughness may provide better insight into the area of "true contact." A Zygo NewView 6300 3D optical surface profiler was used to measure the surface topography of the silicon bonding surface. MetroPro software was used to correct the raw data for system errors and "flatten" the surface mathematically by subtracting the closest-fit spherical component, which allowed the determination of fine-scale roughness. At a magnification of 25x of the system, the surface RMS micro-roughness was ~1 nm.
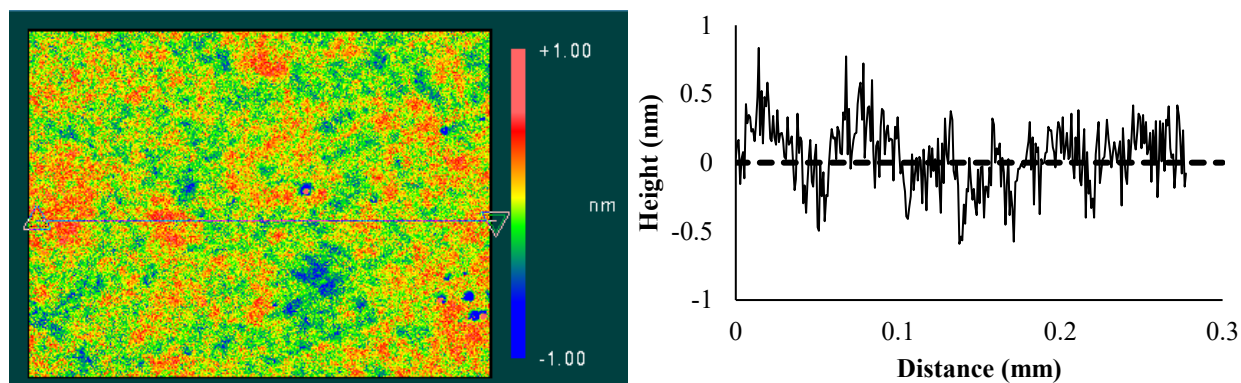
Figure 17. (Left) A visualization obtained from surface profilometry of a bulk silicon sample surface from directly above the surface. This image was taken with a 50x objective at 0.5x digital zoom. System error was subtracted from the sample. (Right) Cross-section view of the left image, where the x-axis follows the left image.

Surface micro-roughness was also measured by a Schmitt Measurement Systems (SMS) μ-scan scatterometer at 670 nm. It uses a bidirectional reflectance distribution function (BRDF) at two angles to determine equivalent surface roughness from optical scatter. The equivalent surface micro-roughness for the samples used in this study was found to be ~0.5 nm .

CZ-grown (100) silicon wafers (76 mm diam., 1 mm thickness, double-side polished) were used for FTIR spectroscopy experiments probing bonded interface chemistry. The wafers were diced in-house to 50x20 mm^2 rectangles and the short edges were polished at 45° for

multiple internal transmission. The Zygo NewView 6300 3D optical surface profiler was again used for surface topography measurements. At a magnification of 25x of the system, surface micro-roughness of the wafers was ~1.5 nm.

3.2 Cleaning Procedure

Following literature on the advantages of plasma treatment to chemical RCA treatment, the bonding surfaces were plasma-treated by a Glow Research AutoGlow Plasma system [16]. The surfaces were exposed to a 100W RF plasma treatment for 2 minutes with a base vacuum of 0.22 torr before introducing 1 torr of O_2. X-ray photoelectron spectroscopy (XPS) data verified surface contamination of organics and metals was reduced to < 2%. Sessile drop experiments showed that the plasma treatment reduced the water contact angle to negligible levels ($\leq 5^\circ$). The samples were then placed under a class 100 laminar flow bench and cleaned with methanol-saturated TX404 Absorbond® polyester wipes to remove visible particulates. XPS was again used to confirm that surface contamination did not increase after this procedure. Although contamination did not rise on average, XPS showed the methanol wipes pushed the existing surface contamination around, as carbon contamination increased in some sampling areas but decreased in others.

3.3 Initial Contact

After the cleaning procedure, the samples were immediately vertically aligned by two standard optical posts and manually placed into contact. In the DB case, spontaneous bonding occurred after a brief 'float' period due to trapped air that quickly leaves the interface [2]. However, previous experience with bulk silica had shown non-uniform propagation of the bonding front in DB samples.

Figure 18. Fused silica sample displaying a bond-front with trapped particles. The transparent region represents well-contacted areas. The cloudy region displays interference fringes that suggest non-contacted areas.

To help illustrate the contacting process, an image of a partially-contacted fused silica sample imaged under a monochromatic mercury lamp is shown in Figure 18. The "bonding front" is marked by the transition from the transparent region to the cloudy region. The interference fringes seen in the cloudy region are representative of Newton's rings, suggesting there is a significant amount of air present between the two surfaces. In addition, Figure 18 also shows the influence of particulates in that they seem to inhibit the progression of the bonding front. To facilitate full propagation of the bonding front, pressure was applied manually across the surface to assist in contact uniformity of DB samples. The slow evaporation of alcohol in AA samples theoretically assists in contact uniformity as capillary forces bring the surfaces into intimate contact. Therefore, pressure was not required for AA samples.

In the alcohol-assisted process, 10 μL of HPLC grade isopropyl alcohol (IPA) was placed on one bond surface before contact. After initial contact, the alcohol-assisted samples were left undisturbed for 72 hours. A minimum of four samples were tested for each aging period, bond method, and temperature condition. Samples that underwent an anneal step did so after a designated aging period in ambient and were subjected to 150°C for 30 minutes.

3.4   Acoustic Microscopy Parameters

The contact-bonded samples were characterized by acoustic microscopy using the commercial Sonoscan C-SAM D9500. The samples were scanned one week after contact and again upon completion of their designated aging period. Annealed samples were also scanned immediately before and after annealing. A 25 MHz transducer was used with a focal length of 2.5" and water was used as a coupling medium. The acoustic beam radius at the focus was 0.3 mm. The gain setting was 60 dB. The transducer had a raster speed of 6 in/sec across a 1.69"x1.69" scan area at a 512x512 resolution. Tedjini *et al.* and Rieutord *et al.* have shown water can readily infiltrate room-temperature direct-bonded interfaces [48] [49]. To protect bonded samples submerged in the water bath, the bonded interface was protected by two layers of Kapton tape.

3.5   Flatwise Tension

Figure 19. A silicon sample epoxy-bonded to custom aluminum fixtures made in-house for flatwise tension experiments.

After the designated aging periods and annealing conditions, bulk silicon contact-bonded samples were bonded to aluminum fixtures designed for tensile experiments. Loctite 9309.3NA was used as a room-temperature epoxy to bond the silicon samples to aluminum fixtures shown in Figure 19. The fixtures featured a machined-flat surface that matched the silicon circumference. A 10 kN (~2250 lbf.) load cell on an Instron 5966 frame was used for the majority of the tensile tests until samples exceeded the load limit. A 600 kN (~135,000 lbf.) load cell on an Instron 5989 frame was used for the remainder. The samples that reached the load limit are noted in the relevant figures. The samples were pulled at a constant rate of 0.04 mm/sec until failure.

4. Direct Bond (DB) Results

In this section, tensile load capacity and acoustic microscopy data of direct-bond samples will be shown. Load capacity is shown instead of tensile strength in acknowledgement of the unknown "true" area of contact for each contacted sample, as discussed earlier in Section 2.1.2. Room-temperature results will be shown first, followed by annealing effects. A handful of samples were aged in an ambient environment well beyond 4 weeks. For simplicity of scale, DB samples aged for at least 4 weeks are all grouped together into one age set of "4+" in subsequent graphs. Figure 20 shows that DB samples aged significantly past 4 weeks showed no significant changes in the interface compared to the 4-week set. AA samples were not strength-tested beyond 4 weeks.
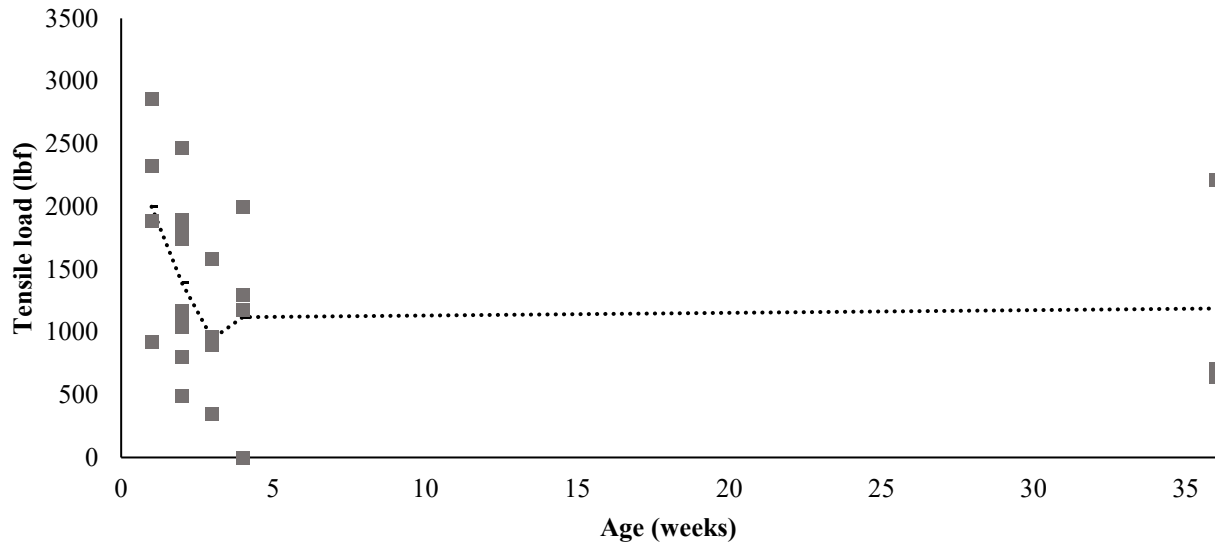
Figure 20. Direct-bonded, RT (100) bulk silicon samples sorted by age for tensile load capacity. Load capacity did not seem to deviate between 1 month through 9 months.

Acoustic microscopy characterization showed all samples displayed a bright ring of reflection around the silicon circumference, which indicates a gap. This is likely due to the

surface morphology shown in Figure 16. Many samples showed edges that rounded convex, meaning opposing surfaces curled away from each other around the edges.

4.1 Room temperature DB

Results from acoustic microscopy showed effective qualitative characterization of the contact-bonded interface. Using the color scale from Figure 12, particulates and points of non-contact were easily discernible. As the color scale is a log scale, red areas are more reflective than black areas by several orders of magnitude. Acoustic microscopy of DB samples typically showed particulates in the interface. Despite best efforts to clean sample surfaces and use of a class 100 laminar flow bench, small particulates remained on many bonding surfaces. Figure 21 shows a typical sample in the DB set, wherein small points of reflection can be seen on the left image. These reflective points likely correspond to fine particulates, as particulates cause gaps in the interface, which lead to acoustic reflection. Furthermore, previous analysis from optical imaging and acoustic microscopy of bonded fused silica samples, like the one shown in Figure 18, showed correlation between particulate locations in optical images and reflection points in acoustic microscopy raster images.

The particular sample in Figure 21 also had a significant area of un-bond displayed in red. The sample also showed interfacial bubble development after 4 weeks of ambient aging. Across the room temperature DB sample set, bubble development was seen after 4 weeks of age.
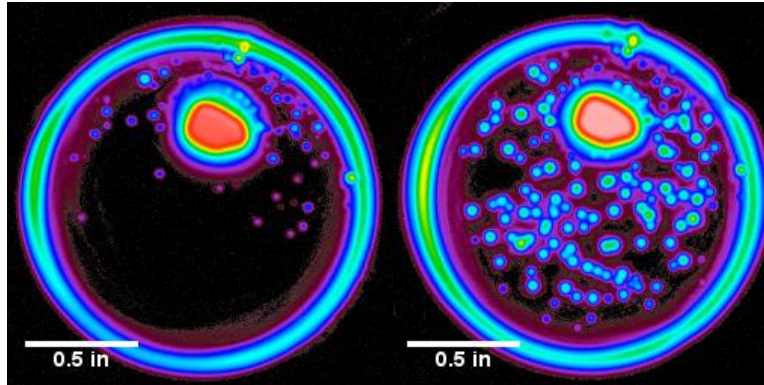
Figure 21. Acoustic microscopy images of the same DB silicon sample at 1 week (L) and 4 weeks (R) of aging at room temperature (RT). These images correspond to longitudinal reflections from the interface.

Strength tests (Figure 22) show that the DB samples were very strong at the outset. Following the weekly average load line, load capacity seems to decrease from the 1-week set through the 3-week set and then increase between the 3 and 4-week age sets. However, it is difficult to draw steadfast conclusions due to the limited number of samples in each age group and the large degree of scatter seen in each group.

A simple regression model using a least-squares fit was used to determine whether the trend shown by the average load capacity is statistically significant. The linear downward trend seen from weeks 1-3 held a statistically significant slope of 0.0319, suggesting that this trend is a real trend. However, attempts at linear and quadratic fits including week "4+" were not statistically significant, suggesting that the "leveling off" seen by the averages plot may not be indicative of true behavior. Though the data set may lack statistical rigor, Figure 22 follows the general trend shown in literature for hydroxide-catalyzed contact bonds, which suggests that a more robust data set may yield similar behavior [9].

It is unclear why the DB samples held higher loads at 1 week compared to the following weeks, as literature suggests that interfacial strength should generally improve with time,

followed by strength stabilization [2] [19]. Regardless of the overall trend, the room temperature DB samples were able to generally hold at least 1000 lbf. (~4 MPa for a 38 mm diam. sample) on average within each age group.
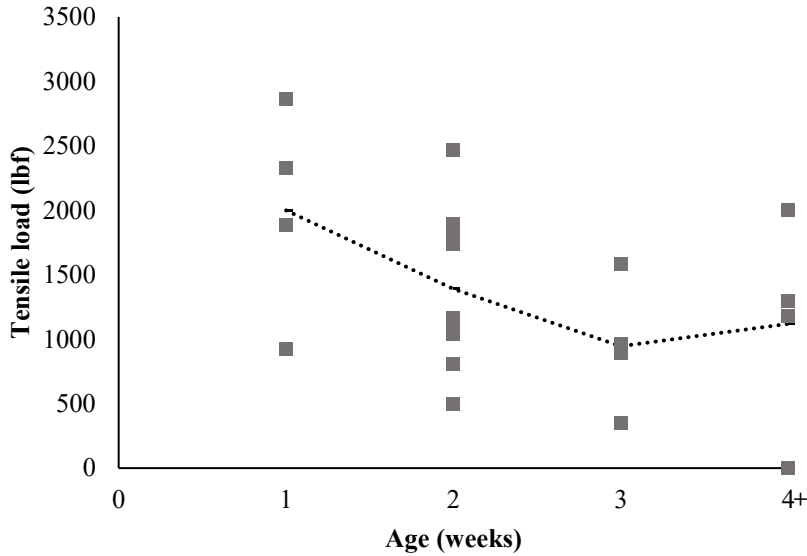
Figure 22. Direct-bonded, RT (100) bulk silicon samples sorted by age for tensile load capacity. Dotted line represents average load capacity within each age group. Samples aged for longer than 4 weeks were grouped into one column as no interfacial changes were detected.

4.2 Annealed Direct-Bond Samples

Low-temperature annealing at 150°C for 30 minutes impacted the direct-bond samples in terms of tensile strength and interface behavior. Acoustic microscopy results are shown first to highlight differences in interface behavior, followed by tensile strengths.

Results from acoustic microscopy showed annealing the DB samples produced an unexpected effect across the entire sample set. The DB samples did not show dramatic bubble formation from annealing, deviating from the literature expectation described in Section 2.2.3. Instead, acoustic microscopy showed the development of a consistent reflection signature that

was seen in all annealed samples regardless of age. Figure 23 shows this signature, which appears as a bright purple reflection by color scale interpretation that corresponds to ~0.5% reflectivity. The cause of this reflection is unclear, and several possibilities are discussed in Section 7. However, the reflection signature would seem to indicate a change in the interface condition, which may impact the overall strength of the samples in comparison to the room temperature data set.
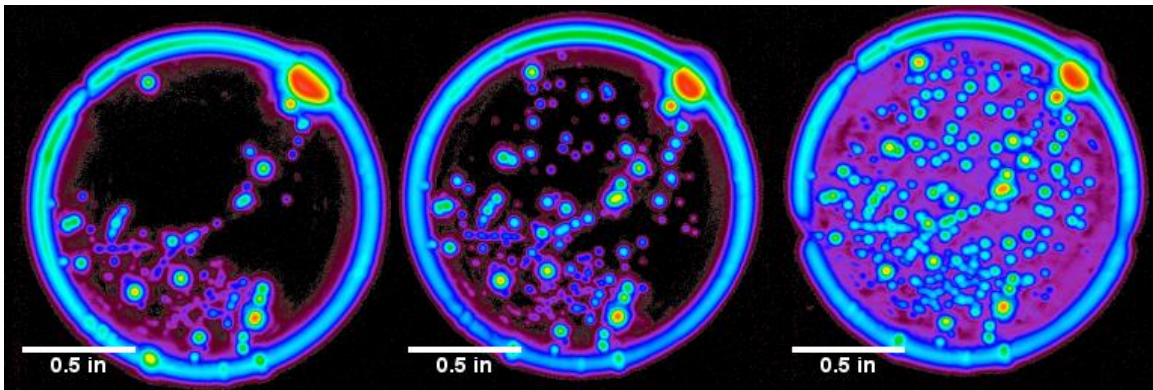
Figure 23. Acoustic microscopy images of the same DB silicon sample at 1 week of aging at RT (left), at 6 months before an 150ºC, 30-minute anneal treatment (middle) and after the annealing treatment (right). These images correspond to longitudinal reflections in the interface.

Flatwise tension data in Figure 24 clearly shows a change in strength trends over time when compared to the room temperature DB set. It is important to note that the average strength values at 2 and 4 weeks of age do not reflect the true strengths of the groups, as several samples reached the load limit of the 10 kN (~2250 lbf.) load cell initially used in this experiment. Subsequent samples were tested in a larger load cell.

Annealing seems to have eliminated the downwards strength trend shown in Figure 22. In some ways, this may have been expected as the reflection signature shown in Figure 23 was consistent across the entire annealed set, indicating a uniform change in the interface for all

samples. Though loads are still inconsistent across age groups, average strength stays above 1500 lbf. (~5.8 MPa for a 38 mm diam. sample) across the board and consistency improved within each age group. Though consistency improved in comparison to the room temperature set, strength still deviates by ~1000 lbf. (~4 MPa for a 38 mm diam. sample) between the weakest and strongest samples within an age group. This behavior is discussed in Section 7.
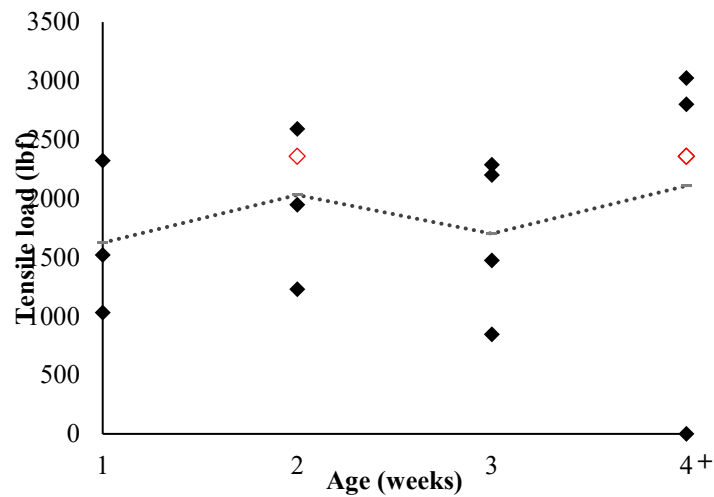
Figure 24. Annealed direct bonded (100) bulk silicon samples sorted by age for tensile load capacity. Dotted line represents average load capacity within each age group. Samples aged for longer than 4 weeks were grouped into one column as no strength changes were seen. The red diamond markers indicate annealed samples that reached the 10 kN (~2250 lbf.) load cell limit and are not indicative of the actual tensile capacities of the samples.

Annealing DB samples resulted in a higher tensile load capacity for every age group except the 1-week group. Figure 25 presents tensile strength for RT and 150°C annealed samples and the trend is clear. By 4 weeks, the average strength of the annealed samples is nearly double that of the room temperature samples, from ~1400 lbf (~5.5 MPa for a 38 mm diam. sample) to ~2600 lbf. (~10 MPa for a 38 mm diam. sample). Again, due to the skewed data from the 10 kN (~2250 lbf.) load cell, the difference in the averages should likely be even greater.
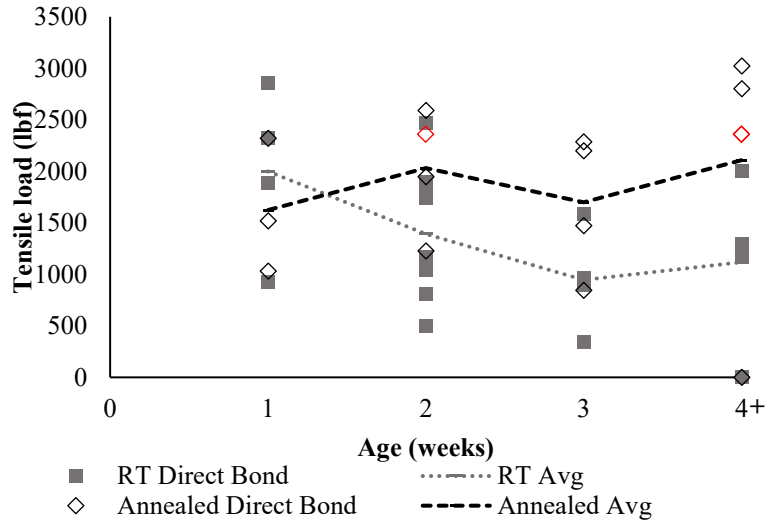
Figure 25. RT vs annealed direct-bonded (100) bulk silicon samples sorted by age for tensile load capacity. Samples aged for longer than 4 weeks were grouped into one column as no strength changes were seen. The red diamond markers indicate annealed samples that reached the 10 kN (~2250 lbf.) load cell limit and are not indicative of the actual tensile capacities of the samples.

4.3   Tensile Load v Stiffness (Direct Bond)

The tensile results of direct-bond samples displayed a great degree of scatter within each age group. Although average tensile strengths of room-temperature samples were over 1000 lbf. (~4 MPa for a 38 mm diam. sample), many samples were surprisingly weak. The large degree of strength scatter places more emphasis on the need for an effective non-destructive evaluation of the bonded parts. As such, the following results explore the ability of acoustic microscopy to accurately describe sample strength.

Using the spring model shown in Section 2.3, interfacial stiffness of bonded interfaces was calculated from reflectivity measurements, by Equation 10, for each direct-bonded sample. Instead of calculating stiffness of each pixel in a raster image, an average sample reflectivity across 38 mm (1.5") diam. surfaces was used to find average stiffness. Section 2.3 showed that

interfacial stiffness may be correlated to the degree of bonding present in an interface. Uncoupled surfaces should exhibit low or no stiffness. Highly coupled surfaces, such as covalently-bound surfaces, should exhibit very high stiffnesses. The "maximum" stiffness of a contact-bonded sample was determined by using a "thin film" model of siloxane bonds filling the interface. Ratios were then taken of average sample stiffness to the "maximum" stiffness to express the "quality" of a contact bond. The ratio is used in all subsequent figures regarding acoustic microscopy results.

Figure 26 shows all the samples, room temperature and annealed, plotted together for tensile load and interfacial stiffness. Upon first glance, two details stand out: a linear trend seems to exist between tensile load to stiffness, but there is a great deal of scatter. However, tensile data indicated strength dependencies on aging time and temperature. Acoustic microscopy also showed interfacial differences over time by way of bubble formation, and thermal condition by way of raised sample reflectivity after annealing. Thus, the large scatter shown in Figure 26 may be reduced by controlling for both variables.
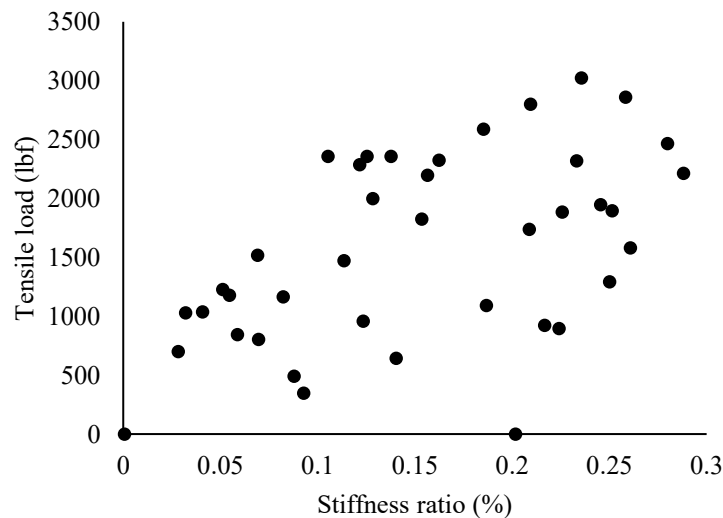
Figure 26. All direct-bonded bulk silicon samples plotted for tensile load against interfacial stiffness. Pre-annealed stiffness values were used for the annealed samples.

40

Results will first be shown for the room temperature set, followed by the annealed set. Individual age groups will also be shown for each sample set. Simple linear regression models are used to determine statistical correlation between load and stiffness. Note that the trendlines shown in the following graphs are not best-fit lines as the intercepts have been forced to 0 to better model a realistic system.

4.3.1   Room-temperature DB Stiffness

Analysis of the entire room-temperature set for stiffness shows a promising linear trend of load to stiffness. The R-squared value for the simple linear model shown in Figure 27 is 36%, suggesting statistical significance. However, there is a large degree of deviation away from the trendline. A portion of this deviation may be a result of age considerations. As such, separate age groups will be considered to discern whether discriminating in time improves the scatter. The 2-week and 4-week age groups will be used for individual age group analysis of the room-temperature direct-bonded samples as these groups contained the most data points.
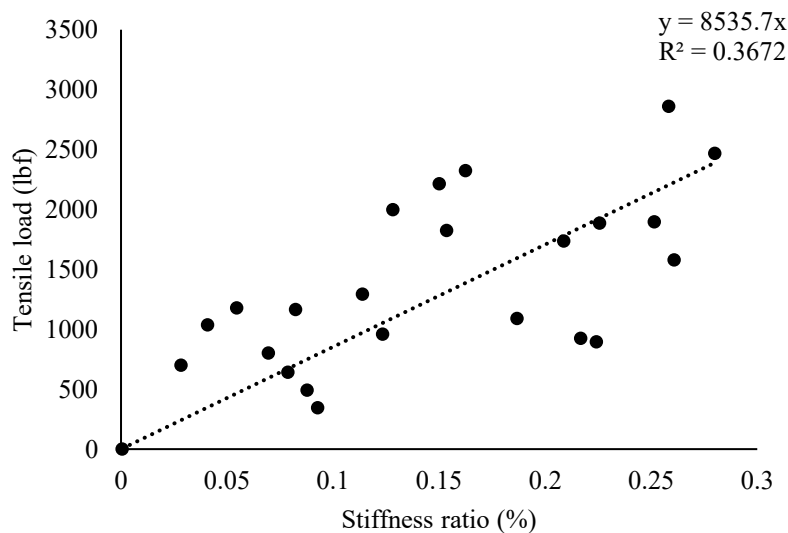
Figure 27. Entire room temperature bulk (100) contact-bonded silicon sample set plotted for tensile load against interfacial stiffness. Avg deviation from trendline: 464 lbf.

41
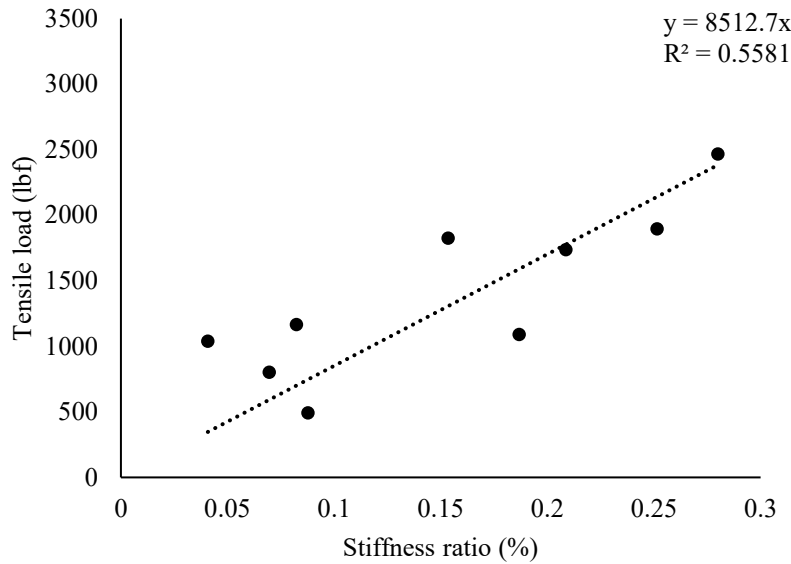
Figure 28. Room temperature bulk silicon direct-bonded samples aged for 2 weeks and plotted for tensile load against interfacial stiffness. Average deviation from trendline: 333 lbf.

Within the 2-week sample set, Figure 28 shows significant improvement compared to Figure 27 in terms of scatter. In this sample set, acoustic microscopy did not show bubble development that lowered the average stiffness values. In this case, the average deviation is 333 lbf, which is still lower than the deviation seen in Figure 27. Furthermore, the linear model shown in Figure 28 shows a R-squared value of 55%, which suggests statistical significance.

The 4-week data group showed similar results as the 2-week set. Figure 29 shows a tight linear correlation between interface stiffness and tensile load. The linear model shown here has an R-squared value of 82%, which is statistically significant. This age group includes samples that developed bubbles in the interface, which lowered the average calculated stiffness value in the interface. The impact of the bubbles on stiffness can be seen in Figure 29 by the grouping of sample stiffness at the low end of the x-axis. The bubble development in this age group likely increased the scatter shown in Figure 27. Within the 4-week group, the average deviation from the trendline is 257 lbf. At the lower end of stiffness values, this deviation is quite large, as the

samples failed at around 1000 lbf. However, towards the high end of stiffness, the samples failed around 2500 lbf., making a deviation of ~250 lbf. much less severe.
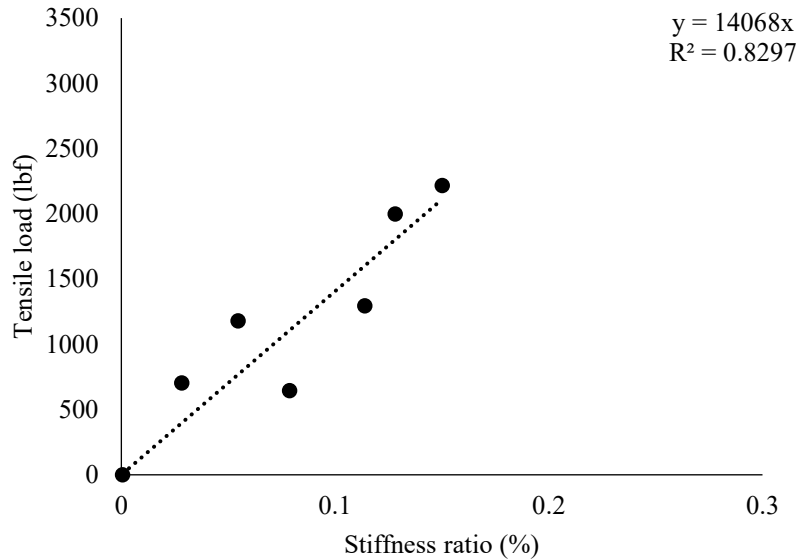
Figure 29. Room temperature bulk silicon direct-bonded samples aged for a minimum of 4 weeks plotted for tensile load against interfacial stiffness. Average deviation from trendline: 257 lbf.

4.3.2   Annealed DB Stiffness

Annealed samples were evaluated by acoustic microscopy both before and after the annealing procedure to determine immediate interface changes. Figure 23 showed the appearance of a uniform bright purple reflection after annealing. As stiffness is calculated from reflectivity, analysis of the annealed direct-bonded samples for stiffness showed two incredibly different sets of stiffness values from pre-annealed and post-annealed interface characterization. After the low-temperature annealing treatment, stiffness values decreased severely in comparison to the pre-annealed stiffness values. Again, this is likely due to the bright purple reflection found in acoustic microscopy. The large reduction in stiffness can easily be seen in Figure 30, which shows all annealed direct-bond samples for both pre-annealed and post-annealed stiffness. As a

reminder, these samples were characterized twice by acoustic microscopy, once before and once after annealing, before undergoing the tensile pull test. From strength trends shown earlier in Figure 25, there was clearly no decrease in strength between the annealed and room temperature sample sets. Therefore, the dramatic reduction in interfacial stiffness is not an accurate reflection of the physical interface. Instead, the reduction is simply due to the increase in overall sample reflectivity.
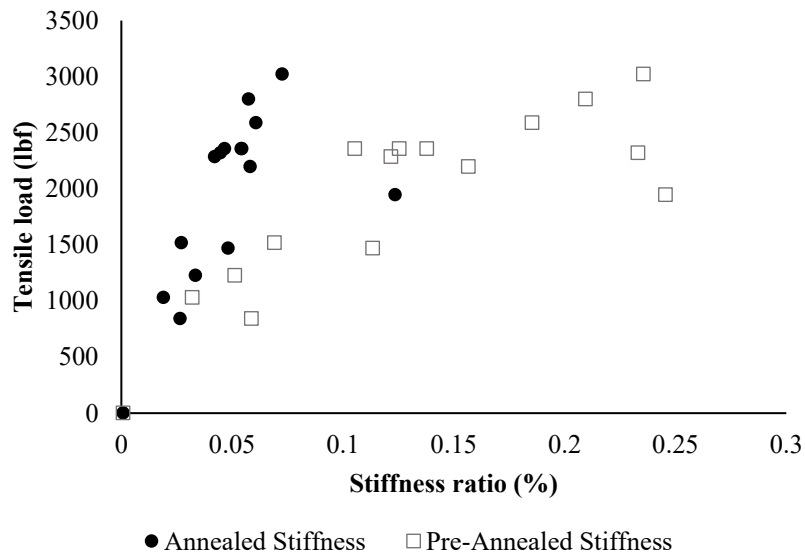
Figure 30. All annealed, direct-bonded bulk silicon samples plotted for tensile load against interfacial stiffness. Samples were annealed at 150°C for 30 minutes. Both pre-annealed and post-annealed stiffnesses are shown for each sample to show stiffness reduction.

Interestingly, analysis using pre-annealed stiffness values yields different results than using post-stiffness values. Analysis of the pre-annealed stiffness values in Figure 31 shows an average deviation from the trendline of 450 lbf. and a R-squared value of 43%.
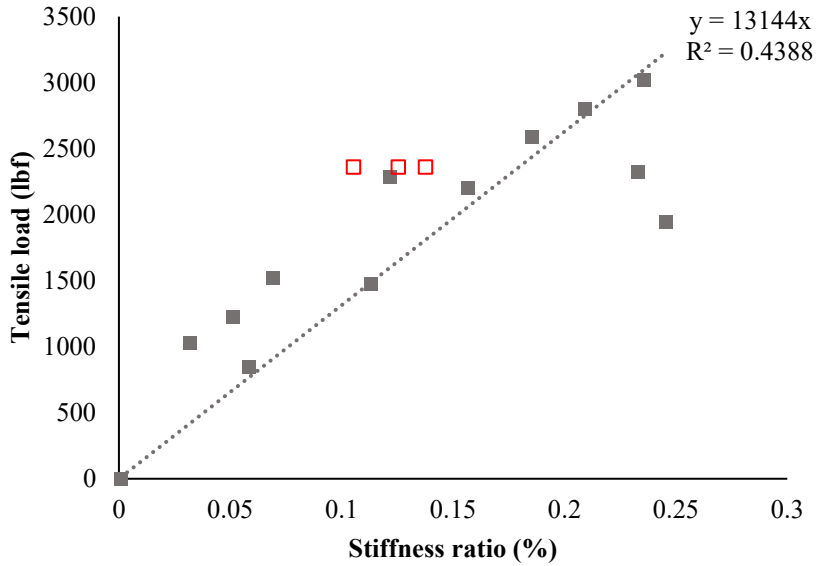
Figure 31. Entire annealed bulk silicon direct-bonded samples plotted for tensile load against interfacial stiffness values taken before annealing at 150°C for 30 minutes. Average deviation from trendline: 452 lbf. The red squares indicate samples that reached the 10 kN (~2250 lbf.) load cell limit that was initially used for tensile tests and are thus not indicative of "true" strengths.
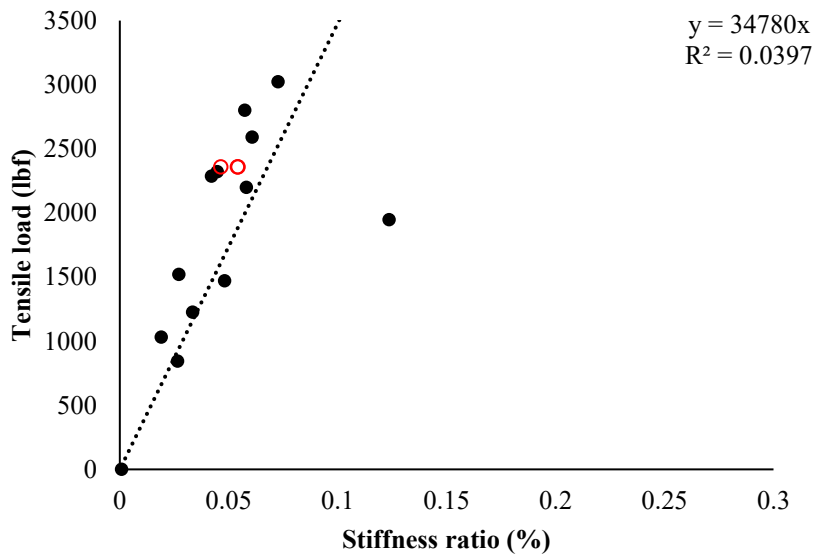
Figure 32. Entire annealed bulk silicon direct-bonded samples plotted for tensile load against interfacial stiffness values taken after annealing at 150°C for 30 minutes. Average deviation from trendline: 557 lbf. The red circles indicate samples that reached the 10 kN (~2250 lbf.) load cell limit that was initially used for tensile tests and are thus not indicative of "true" strength.

Analysis of the entire annealed set using post-annealed stiffness values yields a considerably different trendline than that for pre-annealed stiffness values. Figure 32 shows trendline deviation using post-annealed values is 557 lbf., which is approximately 25% higher than the pre-annealed stiffness deviation. Furthermore, the R-squared value drops an order of magnitude, from 43% to 4%. However, much of this is due to a single outlier that is clearly visible in Figure 32.

It is important to note that Figure 32 and Figure 31 are likely both affected by the handful of samples that reached the limit of the smaller 10 kN (~2250 lbf.) load cell. These samples are marked in red on both graphs. If these samples are removed, the average deviation increases for both figures. This also limits the analysis of individual age groups within the annealed set. Only 4 samples were tested in both the 1-week and 3-week annealed sets, which limits the data points on hand for analysis.
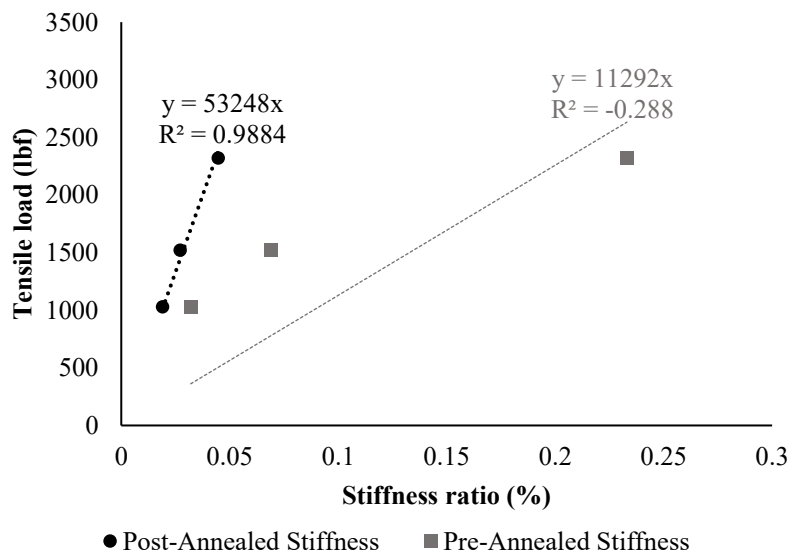
Figure 33. Annealed bulk silicon direct-bonded samples aged for 1 week, plotted for tensile load against interfacial stiffness values taken before and after annealing at 150°C for 30 minutes. Avg deviation from pre-annealed trendline: 573 lbf. From post-annealed trendline: 52 lbf.

Given that there are only 3 samples in the 1-week data set, statistics cannot provide steadfast results for this set. However, analysis of pre- to post-annealed behavior still provides some insight. The 1-week annealed set is shown in Figure 33, which shows inconsistent stiffness reduction between samples In this group, with only three samples, using post-annealed stiffness values significantly improves linear correlation as R-squared changes from negative, which suggests no correlation, to 98%, which suggests significant correlation.

In Figure 34, stiffness reduction from annealing can be seen again in the 3-week age group. The degree of reduction from annealing was not consistent between samples, despite similar age and the same annealing environment. Despite very different stiffness values, the R-squared values for both linear models suggest statistical significance regardless of reduction. This behavior is different from that seen in the 1-week age group, wherein only post-annealed stiffness values showed statistical significance.
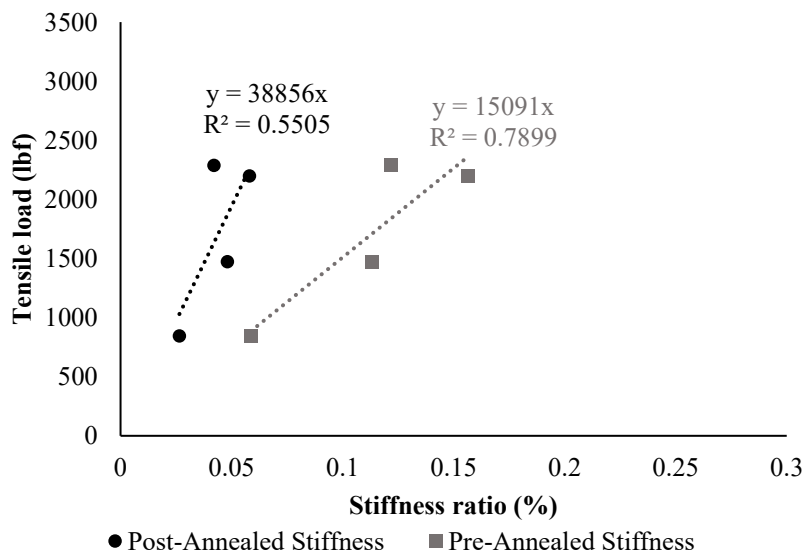
Figure 34. Annealed bulk silicon direct-bonded samples aged for 3 weeks, plotted for tensile load against interfacial stiffness values taken before and after annealing at 150°C for 30 minutes. Average deviation from pre-annealed trendline: 224 lbf. From post-annealed trendline: 323 lbf.

From a scatter standpoint, it is unclear whether pre-annealed or post-annealed stiffness should be used for tighter linear correlation. From a physical standpoint, pre-annealed stiffness likely provides a better picture of the interface as post-annealed stiffnesses would suggest that a low degree of stiffness in the interface still results in high tensile load capabilities.

5. Alcohol-Assisted (AA) Results

In this section, tensile load capacity and acoustic microscopy data of alcohol-assisted samples will be shown. Again, load capacity is shown instead of tensile strength in acknowledgement of the unknown "true" area of contact for each contacted sample, as discussed earlier in Section 2.1.2.

As with the direct-bond samples, acoustic microscopy characterization showed all samples displayed a bright ring of reflection around the silicon circumference. Again, this is likely due to the surface morphology shown in Figure 16 as contacting surfaces deviated from each other at the edge. Results will first be shown for the room temperature sample set, followed by the annealed sample set.

5.1   Room Temperature Alcohol-Assisted

Acoustic microscopy of the AA samples 1 week after initiating contact showed very few particulates. Figure 35 shows a raster image of a sample interface that was indicative of all AA samples at 1 week of age in several aspects. First, the left image depicts a uniform interface in terms of distinct points of reflectivity. Second, alcohol-assisted samples consistently showed non-zero reflectivity across the interface at 1 week of age. In Figure 35, this is shown as a dark purple reflection, which indicates a ~0.2% reflection that may be explained by the remaining presence of alcohol in the interface. By 4 weeks of age. most alcohol-assisted samples showed larger areas of near-zero reflectivity. In the color scale, this is shown as black areas. Near-zero reflectivity suggests strong acoustic coupling between surfaces, which is a sign of intimate contact. This may be due to alcohol evaporation out of the interface over time. As the area of non-zero reflectivity decreased over time, other distinct points of reflectivity often appeared. In

Figure 35, several bright blue dots can be seen in the 4-week raster image. This may be attributed to very fine particulates that may have been previously masked by the presence of alcohol.
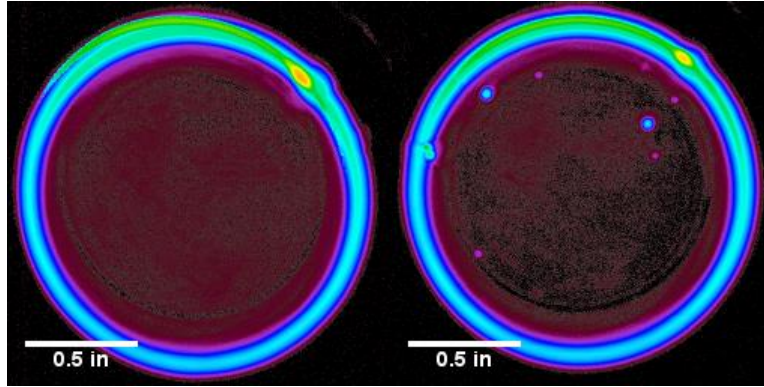
Figure 35. Acoustic microscopy images of the same alcohol-assisted silicon sample at 1 week (L) and 4 weeks (R) of aging at room temperature (RT). These images correspond to longitudinal reflections at the interface.

Acoustic microscopy of 3-week and 4-week aged samples indicates no bubble development. This was surprising as bubbles were seen in the direct-bond samples by 4 weeks of age, as shown in Figure 21. One possibility for the lack of bubble formation is insufficient time for its formation. To address that question, a handful of AA samples were aged for about one year in ambient. Even then, interfacial bubbles did not appear. Possible explanations for the lack of bubble formation are discussed in Section 7.3.

Despite a lack of bubble formation, acoustic microscopy did show a general reduction in reflection amplitude over time (i.e. greater black areas in Figure 35), suggesting that tensile load should vary with time as well. Figure 36 below shows tensile load data for every age group. Between 1 and 2 weeks of age, Figure 36 shows a decrease in strength that could be attributed to the loss of capillary force. The load capacities of the 1-week sample set could be solely attributed to capillary forces as Figure 7 shows that capillary force is theoretically capable of sustaining these loads. Between 2 and 3 weeks of age, sample strength increases. From 3 to 4 weeks of age,

50

strength stayed relatively stable, as the slight slump shown by the dotted average line may not be statistically significant.
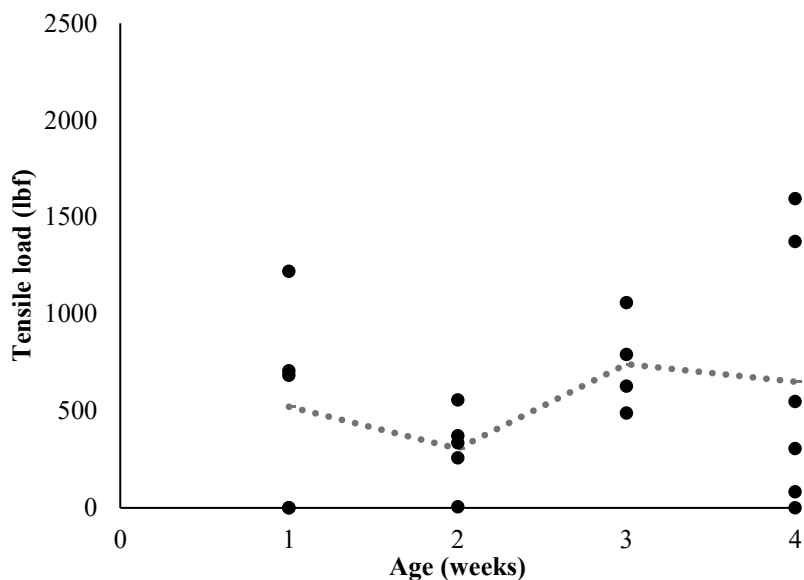
Figure 36. Tensile load capacity of RT alcohol-assisted (100) bulk silicon samples sorted by age. Dotted line represents average load capacity within each age group.

Again, due to the large spread in strength data with only four samples in most age groups, it is difficult to assign statistical significance to many of the trends. The 1-week and 4-week sets, especially, show strength ranges of nearly 2000 lbf. from the weakest to the strongest sample in each group. Thus, the averages shown in Figure 36 should be interpreted with caution.

5.2   Annealed Alcohol-Assisted Method

As with the direct-bond samples, low-temperature annealing was expected to impact the behavior of alcohol-assisted samples compared to their room-temperature sisters. From the literature expectation discussed in Section 2.2.3, annealing at 150°C should increase sample strength by driving covalent siloxane bond formation in the interface. However, the presence of alcohol may lead to different results, as the vapor pressure of alcohol may increase at elevated

temperatures and de-bond portions of the interface. The possible effects of alcohol presence are discussed in detail in Section 7.4. Results from acoustic microscopy are shown first, followed by tensile strength results.

Figure 37, which depicts a typical alcohol-assisted sample, shows significant development in the interface occurred from the annealing process. The development seen here differs to the development seen in annealed DB samples. Interestingly, similar behavior was seen in all annealed alcohol-assisted samples, regardless of age. This suggests the mechanism responsible for this bubble development stays present over time.
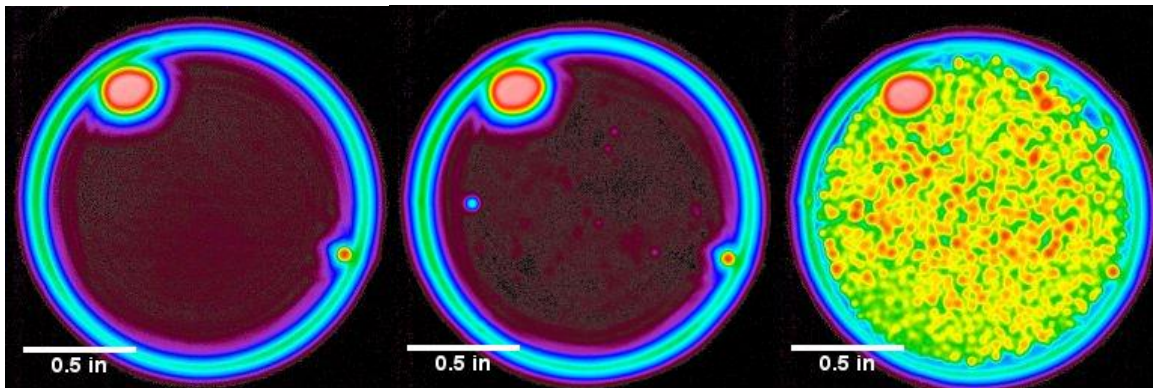
Figure 37. Acoustic microscopy images of the same alcohol-assisted silicon sample at 1 week of aging at RT (left), 4 weeks of aging at RT (middle), and after a 30-minute, 150°C anneal (right). Sample was aged for 4 weeks before annealing. These images correspond to longitudinal reflections from the interface.

Though the behavior shown in Figure 37 was consistently seen in acoustic microscopy over time, Figure 38 shows the effect from low-temperature annealing on tensile load capacity varied between age groups. At 1 week of age, none of the samples survived the annealing treatment. The subsequent age groups all show increases in average tensile load capacity.
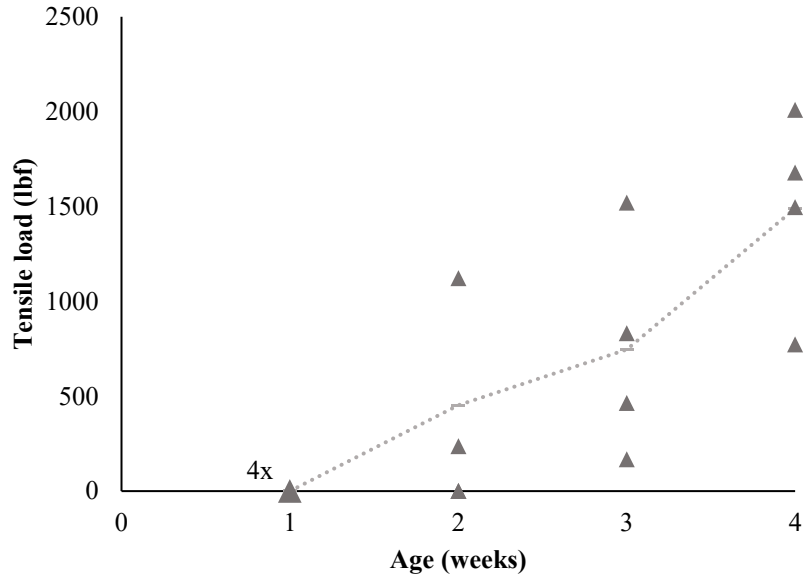
Figure 38. Tensile load capacity of annealed alcohol-assisted (100) bulk silicon samples sorted by age. Dotted line represents average load capacity within each age group. The large marker for the 1-week set represents 4 separate samples that all failed during the annealing process.
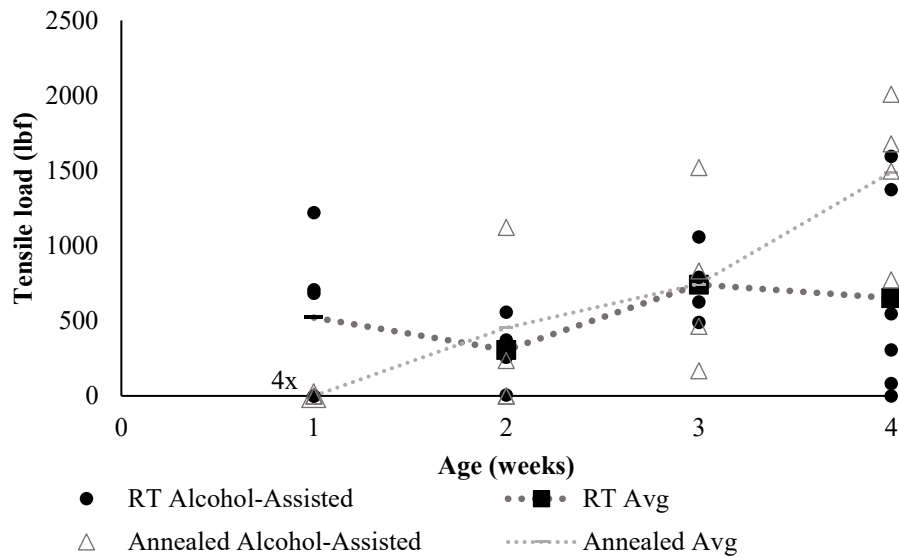
Figure 39. Impact of annealing on alcohol-assisted (100) bulk silicon samples sorted by age for flatwise tension. The large marker for the 1-week annealed set represents 4 separate samples that all failed during the annealing process.

A comparison of the room temperature set to the annealed set in Figure 39 shows the RT samples were significantly stronger than annealed samples at 1 week of age, but by 4 weeks of

age, the RT samples were significantly weaker than annealed samples. The strength difference in the 1-week age group may be attributed to the presence and disappearance of alcohol in the RT and annealed sets, respectively. At 2 and 3 weeks of age, it is difficult to determine whether strength significantly changed between the two sets as the difference between the two may not be statistically significant. The 4-week annealed set shows a sharp increase in strength in comparison to the room temperature set. In all sets except for the 1-week set, annealing resulted in a higher maximum load capacity as well. Given these results, it seems that beyond the 1-week set, annealing increased overall load capacity.

5.3   Tensile Load v Stiffness (Alcohol-Assisted)

Like the tensile results of direct-bond samples, the tensile results shown above for alcohol-assisted samples also displayed a great degree of scatter within each age group. Within each age group, some samples were unable to hold any load (0 lbf) while others held above 1000 lbf. (~4 MPa for a 38 mm diam. sample). As such, the importance of accurate non-destructive evaluation is equally relevant for alcohol-assisted samples as for direct-bond samples. The following results explore the ability of acoustic microscopy to accurately predict sample strength of alcohol-assisted samples. The spring model of the interface used to analyze the direct-bonded sample set was again used to analyze the alcohol-assisted sample set. Again, the relevant background was provided in Section 2.5.

Unlike the direct-bonded set, which showed a reasonable linear correlation between tensile load capacity and interfacial stiffness ratio, Figure 40 shows no discernible correlation. Interestingly, the majority of AA samples had a stiffness ratio that clustered within 0.15-0.25%, but the tensile load capacity seemed to randomly vary from 0-2000 lbf. (~8 MPa for a 38 mm

diam. sample). Because interfacial stiffness is a function of measured sample reflectivity, the lack of particulates, voids, and other reflective points (shown in Figure 37) may correspond to relatively similar stiffnesses between samples. This may explain the relatively tight grouping of interfacial stiffness in alcohol-assisted samples in comparison to the direct-bond samples. Although Figure 40 does not show a discernible pattern, it has been shown in the direct bond samples that separating variables of time and thermal history improved scatter.
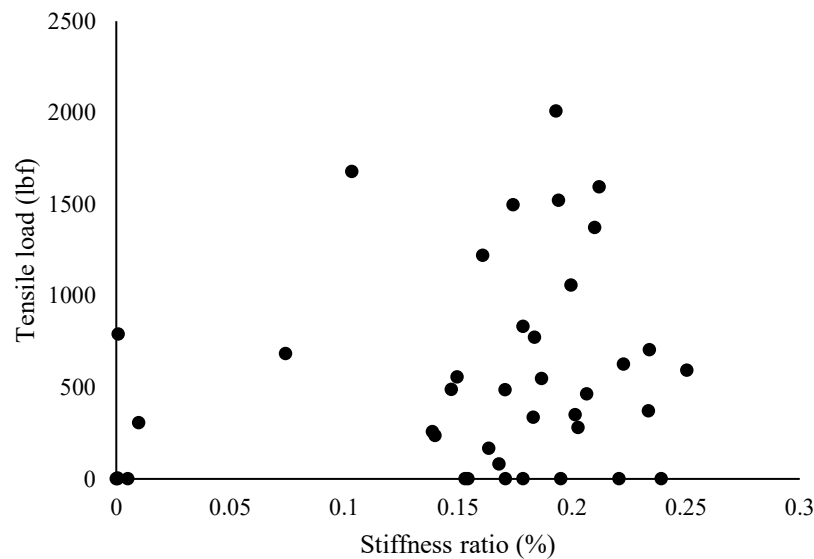
Figure 40. All alcohol-assisted bulk silicon samples plotted for tensile load against interfacial stiffness. Pre-annealed stiffness values were used for the annealed samples.

Separating for time and thermal history did not improve any correlation between stiffness and tensile load. The following figures are provided for completeness to highlight that scatter does not improve by separating for time and thermal history. In a few of the age groups, there seemed to be a potential linear correlation akin to the direct-bond samples, but these are likely statistical flukes as there are only a handful of data points within each age group.

5.3.1 Room Temperature AA Stiffness
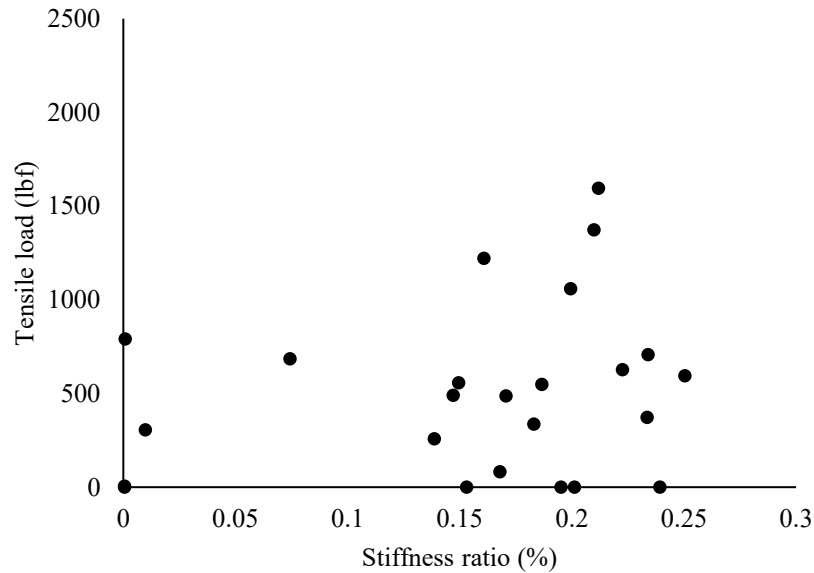
Figure 41. Room-temperature alcohol-assisted bulk silicon samples plotted for tensile load against interfacial stiffness.

Figure 41 shows all room-temperature AA samples. Clearly, there is still no discernible correlation between sample stiffness and load capacity. However, time has not been isolated in Figure 41.
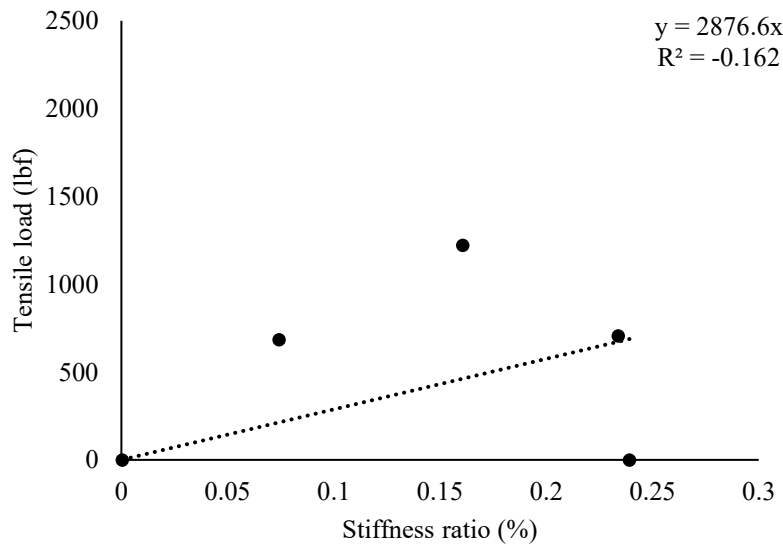
Figure 42. Tensile load vs interfacial stiffness for room-temperature alcohol-assisted bulk silicon samples aged for 1 week in ambient atmosphere. Avg deviation from trendline: 390 lbf.

Analysis of the 1-week group does not yield any statistically significant trends. Figure 42 shows a linear model merely as a reference. The average deviation is ~400 lbf. for the age group. Although this is similar to the deviation seen in Figure 27 for room temperature DB samples, the linear model in this age group yields a negative R-squared value, which implies the current linear model is worse than the null hypothesis of a horizontal line. A horizontal line fit represents the null hypothesis wherein load is not correlated to stiffness. Simply put, this age group shows no correlation between load and stiffness.
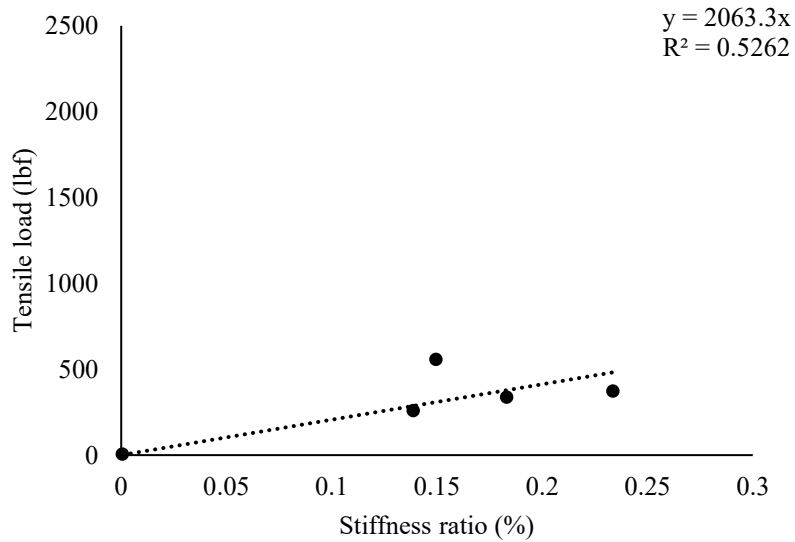
Figure 43. Tensile load vs interfacial stiffness for room-temperature alcohol-assisted bulk silicon samples aged for 2 weeks in ambient atmosphere. Avg deviation from trendline: 86 lbf.

Analysis of the 2-week age group yields a linear correlation. Figure 43 displays minimal deviation from the linear model, with average deviation at ~90 lbf. The R-squared value of the linear model shown in Figure 43 suggests this model is statistically significant. However, steadfast conclusions will not be drawn from this age group due to the small sample size.
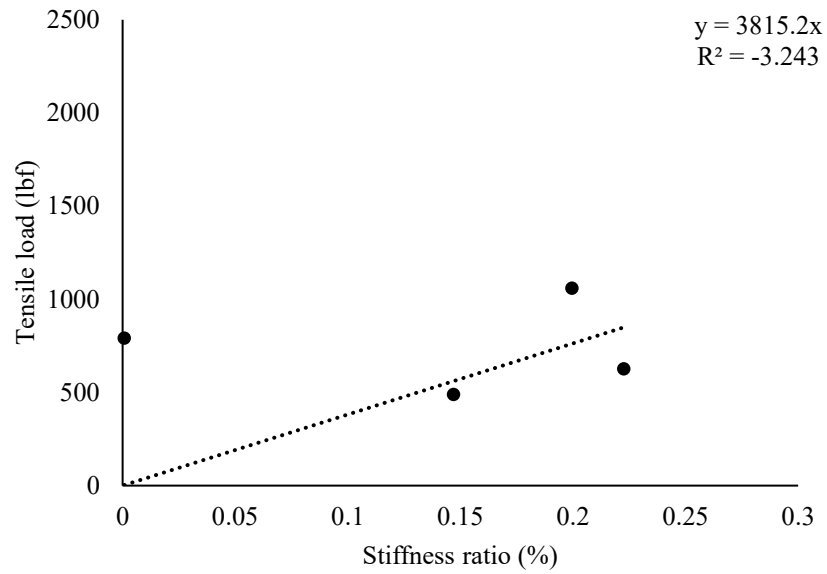
Figure 44. Tensile load vs interfacial stiffness for room-temperature alcohol-assisted bulk silicon samples aged for 3 weeks in ambient atmosphere. Avg deviation from trendline: 345 lbf.

Figure 44 shows the 3-week age group does not display any significant correlation between tensile load and sample stiffness. A simple linear regression model shows a negative R-squared value, which suggests there is no correlation.
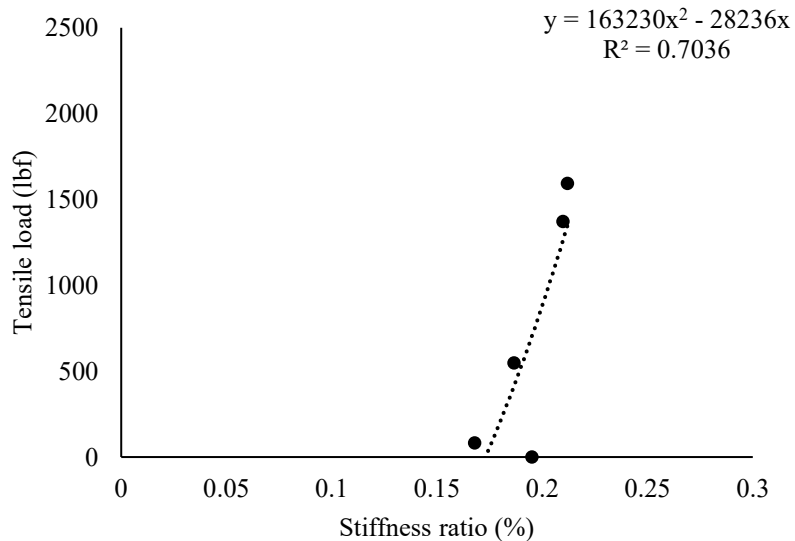
Figure 45. Room-temperature alcohol-assisted bulk silicon samples aged for 4 weeks in ambient atmosphere plotted for tensile load against interfacial stiffness. Avg deviation from trendline: 283 lbf.

Figure 45 shows interfacial stiffness values for the 4-week alcohol-assisted sample set. In this set, it is statistically unclear whether there is a relationship, and the type, between tensile load and stiffness. There is a possible nonlinear correlation between tensile load and stiffness that is plotted in Figure 45. The second-degree polynomial regression model in the figure shows a tight correlation with an R-squared value of 70%. If a realistic simple linear regression model is used, the associated R-squared value is negative, suggesting no statistical significance. Thus, this age group does not show adherence to a model that is both physically realistic and statistically significant.

5.3.2 *Annealed Alcohol-Assisted Stiffness*

Results from acoustic microscopy of annealed direct-bond samples showed an unexpected rise in interface reflectivity that is visible in Figure 23. Since stiffness is derived from measured reflectivity, increases in sample reflectivity are tied to decreases in sample stiffness. Stiffness results shown earlier for annealed direct-bonded samples in Section 4.3.2 showed severe stiffness reduction between pre-annealed and post-annealed values.

Similar behavior was seen in annealed alcohol-assisted samples. Figure 37 showed interface evolution of the alcohol-assisted samples from the annealing process. Like the annealed DB samples, this increase in sample reflectivity upon annealing was tied to stiffness reduction. Again, these samples were characterized twice by acoustic microscopy, once before and once after annealing, before undergoing the tensile pull test. As shown below, stiffness reduction is more severe in the alcohol-assisted set, as Figure 46 shows post-annealed stiffness values decreased to near-zero. Again, as with the earlier figures for alcohol-assisted samples, there is no correlation between stiffness and load.

59
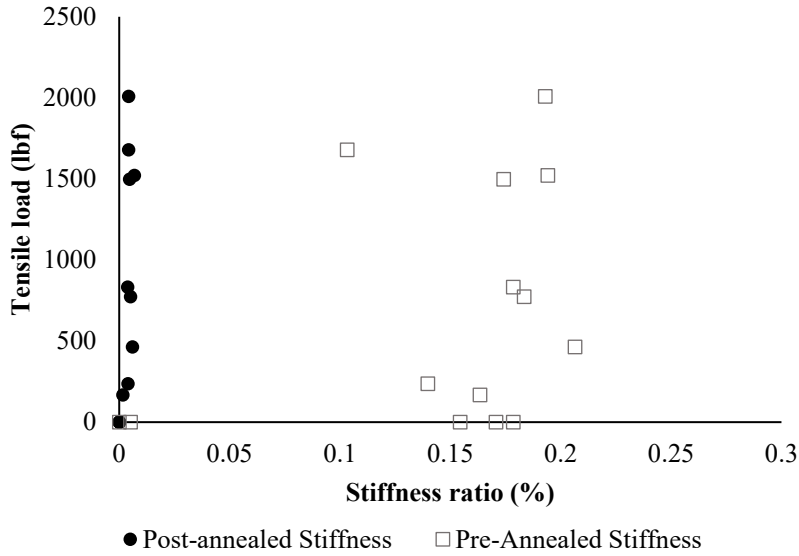
Figure 46. All annealed, alcohol-assisted bulk silicon samples plotted for tensile load against interfacial stiffness. Samples were annealed at 150°C for 30 minutes. Both pre-annealed and post-annealed stiffnesses are shown for each sample to show stiffness reduction.

Further analysis of individual age groups for annealed alcohol-assisted samples is limited to the 3-week and 4-week age groups due to sampling size. None of the four samples in the 1-week age group survived the annealing process, and the 2-week age group showed samples with mismatched silicon crystal orientation. As discussed in Section 2.5, a mismatched crystal orientation results in different acoustic impedance between the two contacting parts, which produces an excessively large acoustic reflection. This resulted in unusable acoustic microscopy data.

Analysis of the 3-week age group in Figure 47 shows that a linear model may be statistically significant. Using pre-annealed stiffness values, the average deviation is 430 lbf. and the R-squared value is low. Taken together, this suggests there is not strong statistical correlation between pre-annealed stiffness values and tensile load. Using post-annealed stiffness values yields a different result. Deviation from the model decreases to 300 lbf. and the R-squared value

is 53%, suggesting statistical significance. However, there are only four data points in this set so statistical conclusions cannot be drawn.
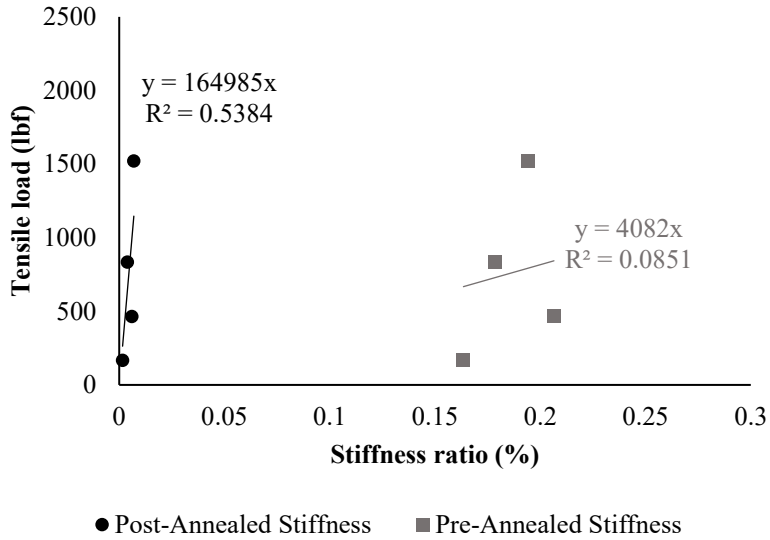
Figure 47. Tensile load vs interfacial stiffness for annealed alcohol-assisted bulk silicon samples aged for 3 weeks in ambient atmosphere. Both pre-annealed and post-annealed stiffness values are shown. Avg deviation from pre-annealed model: 430 lbf. From post-annealed model: 300 lbf.

The 4-week age group does not follow a simple linear model. The R-squared value of the model shown in Figure 48 for pre-annealed stiffness values is negative, suggesting it is not statistically significant. Meanwhile, analysis using post-annealed stiffness values also provides a negative R-squared value. Thus, this sample group does not show any correlation.
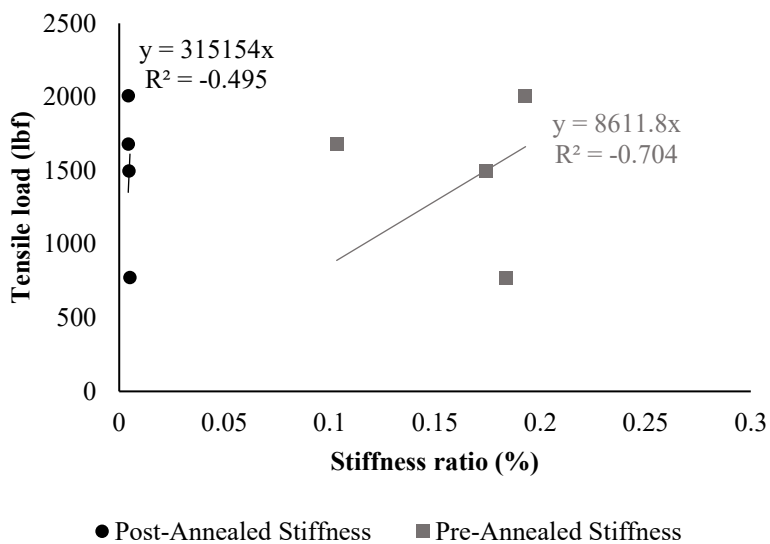
Figure 48. Tensile load vs interfacial stiffness for annealed alcohol-assisted bulk silicon samples aged for 4 weeks in ambient atmosphere. Both pre-annealed and post-annealed stiffness values are shown.

As with the room temperature alcohol-assisted samples, annealed samples did not show any correlation between stiffness from acoustic microscopy and tensile load. The 3-week age group that showed statistical correlation is likely a fluke of statistics, as only four samples were analyzed in that set. These results indicate that acoustic microscopy cannot be used to reliably characterize the strengths of alcohol-assisted samples.

6. Failure Types

In terms of failure type, the two sample sets showed different trends as well. Two main failure types were observed across all samples: adhesive failure at the bonded interface and cohesive failure through bulk silicon. Figure 49 shows an example of failure through the bulk, wherein bulk silicon transferred from one contacted puck to the other. Interestingly, the prevalence of bulk silicon failure neither increased with time nor annealing condition. The only trend seen was that the alcohol-assisted samples almost exclusively failed at the bonded interface, whereas the DB samples readily saw both types. The pattern of bulk-silicon failure also did not show single-origin crack propagation. This behavior of bulk failure was not more prevalent at higher tensile loads. Several samples that held upwards of 2,000 lbf. (7.8 MPa for a 38 mm diam. sample) failed cleanly at the interface, whereas the sample in Figure 49 only held 640 lbf. (2.5 MPa for a 38 mm diam. sample) and failed through the bulk material. The two failure types may have contributed to the large spread of tensile loads seen across all the data sets. Previous literature has reported similar scatter [19] [20].
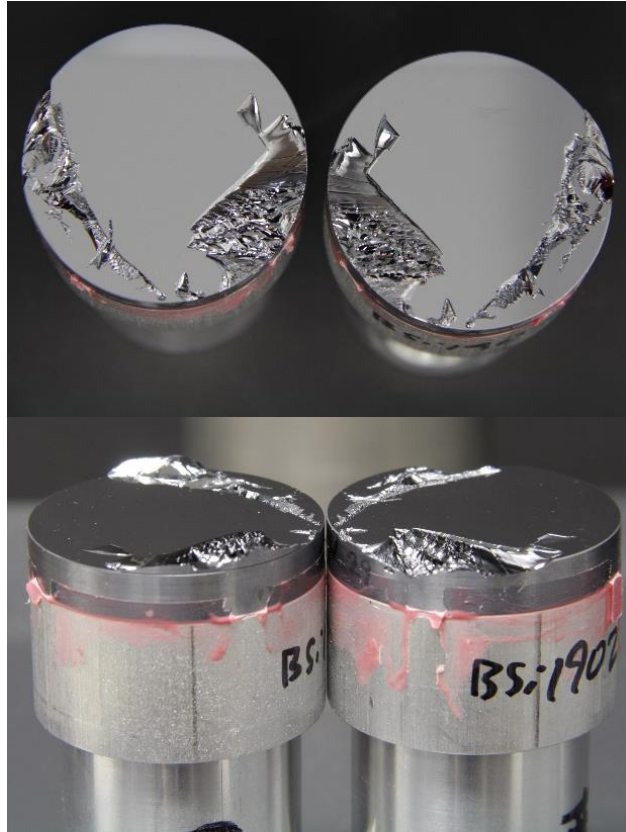
Figure 49. Image of bulk silicon transfer (cohesive failure) in a direct-bonded room temperature sample from a top-down view (upper) and a side view (lower). This sample failed at a relatively low load: 643 lbf. Sample was aged for 36 weeks.

7. Discussion

7.1 Room Temperature Direct Bond

Although the results have already shown reasonable tensile strengths for direct-bond samples and a clear linear relationship between interfacial stiffness and tensile load, several pertinent questions remain. Figure 20 shows the strength of room-temperature samples steadily decreased until approximately 1 month of age, after which strength stabilized. A model of the interface is described below to describe the strength trends in Figure 20.

In addition, acoustic microscopy showed the appearance of bubbles after one month of age. Although literature often cites hydrogen gas as the source of bubbles at elevated temperatures, the source of bubbles at room temperature is still unclear [2].

7.1.1 RT Bubble Development (Direct-Bond)

Acoustic microscopy consistently showed bubble formation in room temperature DB samples, like the one in Figure 21, by 1 month of aging. Assuming the interface is filled with adsorbed water, two hypotheses are posed as the source of these bubbles: hydrogen gas development, or water cavitation. The hydrogen gas hypothesis stems from literature expectation of annealed behaviors, as Mack *et al.* showed bubbles from annealing at 400°C were mainly composed of hydrogen formed through Equation 7 [50]. However, it is unclear whether the process can readily occur at room temperature. The water cavitation hypothesis stems from capillary pressures in the interface, as Duan *et al.* have shown that capillary action in thin nanochannels can cause extremely high negative pressures (-10^2 atm) within the nanochannel

[51]. If the negative pressures become high enough, liquid water may cavitate and form a vapor bubble. This may provide a fitting description of the room temperature process.

Cavitation typically occurs in liquids when the pressure within the liquid drops below its saturated vapor pressure [51] [52] [53]. As water evaporates out of the interface, the remaining liquid may cavitate due to the immense negative pressures associated with capillary forces. Duan *et al*. showed the occurrence of water cavitation in silica nanochannels of gaps ranging from 20-120 nm as water evaporated away [51]. A separate study by Bao *et al.* also found liquid cavitation in silicon nanochannels smaller than 100 nm [53]. The research from Duan *et al.* utilized hydrophilic silica surfaces treated with oxygen plasma and exhibited a surface roughness of < 1 nm. These features resemble the surface conditions of bulk silicon used in this study [51]. Their report showed several key bubble behaviors, regardless of channel height. Namely, in their study, micrometer-sized bubbles nucleated very quickly once water began to evaporate. However, in this report, acoustic microscopy of direct-bonded silicon did not indicate bubble formation until approximately one month of aging in ambient. The time scale may be explained by the growth rate of bubbles in the interface and the comparatively coarse resolution of our acoustic microscopy.

As adsorbed water in a contact-bonded interface evaporates or diffuses away, the remaining water in the interface experiences continually higher tensile forces until it reaches equilibrium or it may cavitate to form water vapor bubbles of nanometer size. However, the acoustic beam radius at the focus of the acoustic microscope was 0.3 mm, meaning a nanometer-sized or micrometer-sized bubble is below the resolution capabilities of the acoustic microscopy setup. In this case, the presence of microscale bubbles would slightly increase acoustic reflectance. Over time, the micrometer-sized bubbles may laterally migrate along the interface

and combine to form larger bubbles. Eventually, the bubbles may become large enough to be resolved by acoustic microscopy.

Another hypothesis is based on research from Mack *et al.* that showed bubble formation at 400°C was due to hydrogen gas by way of water reacting with silicon, as described in Equation 7 [50]. While the work of Mack *et al.* was performed at 400°C rather than at room temperature, it seems reasonable to speculate that bubble formation at room temperature is due to the same mechanism but over longer time spans. This process of bubble formation is as follows. Trapped water in the interface diffuses through native oxide until it reaches the silicon surface. Diffused water then reacts with silicon by Equation 7 to form hydrogen gas and more silicon oxide. Hydrogen diffuses back through the slightly thicker native oxide and coalesces in the interface to form distinct bubbles [2] [50] [54]. To address the rather slow time-scale for bubble development, which was not seen by acoustic microscopy in this study before 1 month of aging, one may argue this process is either diffusion-limited, wherein water slowly diffuses through the oxide layer, or reaction rate-limited, wherein water does not readily react with silicon. If this hypothesis is correct, then either the rate of water diffusion or the reaction rate of silicon oxidation by water must be able to explain bubble formation after several weeks.

To model water diffusion through the native oxide to elemental silicon, two main variables must be determined: diffusivity and boundary conditions. Diffusion coefficients for water in native oxide at room temperature were difficult to find, so the following discussion will assume it behaves like bulk silica glass. Research from Davis and Tomozawa showed that the diffusivity of molecular water in silica glass at low temperatures approaches the Fickian diffusion model [55]. They also showed that the diffusivity of molecular water in silica found by Doremus at higher temperatures could be extrapolated as an upper limit for low temperatures

67

[55] [56]. In regard to diffusion boundary conditions, in the contact-bonding case, the total concentration of water within a bonded sample can be assumed constant at room temperature, but surface concentration decreases with time. Thus, assuming Fickian diffusion, this case can be approximated by using classical drive-in diffusion equations from the semiconductor industry shown below [57]. Classical drive-in diffusion also assumes an infinite substrate thickness, which is not true for a native oxide layer on silicon. Thus, the discussion below should not be taken as a completely accurate model, but it is still instructive.

$$C(x,t) = \frac{S}{\sqrt{\pi D t}} \exp\left[-\frac{x^2}{4Dt}\right] \ [cm^{-3}] \qquad\qquad 13$$

where C(x,t) is the concentration of water at position x and time t, S is the total fixed concentration of water per unit area [57].

To determine surface concentration, the depth can simply be set to 0 $(x = 0)$ in the equation above to lend the following:

$$C(0,t) = C_s(t) = \frac{S}{\sqrt{\pi D t}} \ [cm^{-3}] \qquad\qquad 14$$

where C_s is the surface concentration of water.

The total concentration of water, S, is estimated to be ~$2 * 10^{15} \left[\frac{molec}{cm^2}\right]$ for 3 monolayers. Using research from Davis and Tomozawa, Zouine *et al.* showed the diffusivity of water in silica glass at room temperature is approximately $D = 1.6 * 10^{-17} \left[\frac{cm^2}{s}\right]$ [55] [58]. Figure 50 shows water concentration calculated by Equation 13 using these values.
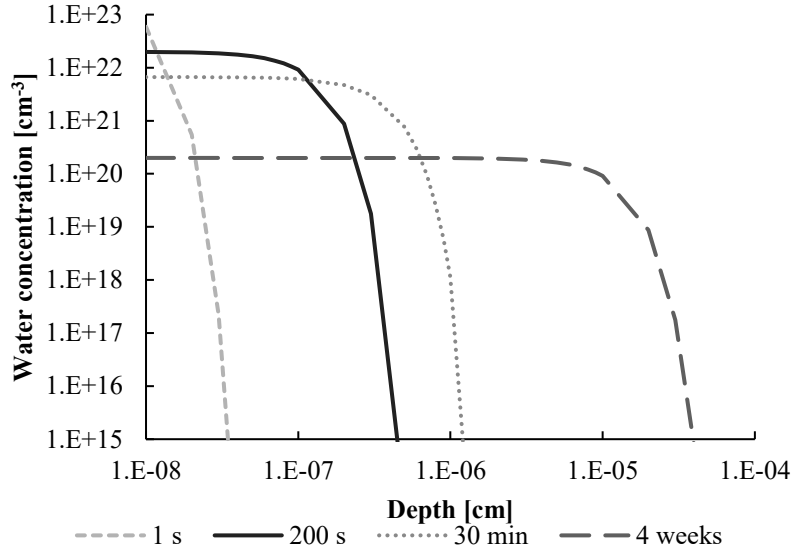
Figure 50. Diffusion profile of water in silica using dopant drive-in diffusion assumptions and a constant diffusivity taken from Zouine *et al.* [58]. Several times are simulated to show changes in water surface concentration. The black line represents the approximate time in this model for water to diffuse through the thickness of the native oxide.

In this approximation, molecular water should diffuse through the native oxide layer (~20 Å) in a matter of minutes at room temperature. However, this approximation likely used a higher diffusivity than what may be seen in the bonded interface. The previous research of water diffusivity in silica glass was performed generally at a pressure of 1 atm [55] [58]. However, the presence of capillary forces in the interface likely induces a negative pressure inside the interface. This may reduce the diffusion rate of water as negative pressure would likely act to draw water into the interface. Thus, the time scales shown above likely over-estimate how quickly water can diffuse through the native oxide. However, the over-estimation of diffusion rate would have to be many orders of magnitude for the time scale to change from minutes to weeks. Since room temperature samples like the one shown in Figure 21 did not exhibit bubble presence until 4 weeks of aging, a diffusion-limited regime is unlikely.

Weldon *et al.* provided an alternative explanation for the time dependency of hydrogen bubbles [38]. They suggest a reaction rate-limited regime below 400°C, wherein silicon oxidation rates by Equation 7 are extremely low. Their analysis extrapolated wet (H_2O) thermal oxidation rates of silicon to room temperature and found the rate constant for oxide growth would be ~10^{-8} $\left[\frac{\mu m}{hr}\right]$ [38] [59]. Over 4 weeks of aging, this would suggest ~0.05 Å of new oxide growth. Since Equation 7 shows an equal amount of hydrogen and silica are produced, this suggests a miniscule amount of hydrogen may develop. Thus, the hydrogen gas hypothesis for interfacial bubbles at room temperature does not seem likely. Though water may diffuse through the oxide quickly, if it cannot react with silicon at room temperature, then hydrogen gas should not form. Furthermore, if water does not react with silicon, then the thin native oxide may likely be saturated with diffused water rather quickly. This may prevent additional water in the interface from diffusing through the oxide.

Instead of hydrogen gas, room-temperature bubbles in the interface may be due to water cavitation. Duan *et al.* demonstrated the occurrence of water cavitation in 20 nm nanochannels [51]. However, future work must be done to determine if this is an accurate model of bubble development, as some research has suggested cavitation may not occur in certain geometries. Tas *et al.* performed a similar experiment to Duan *et al.* and found a lack of water cavitation in their 108 nm nanochannels [52]. The explanation for these contradicting observations is unclear.

7.1.2   *Strength Contributors of RT Direct-bond Samples*

Below 150°C, literature cites a mixture of intermolecular interactions as the basis for adhesion [2] [3] [4]. However, the contribution of each adhesion mechanism to sample strength is unclear. Furthermore, it is unclear how the interplay of these mechanisms translates to strength

trends over time, as Figure 22 showed a clear decrease in strength up to one month, after which strength stabilized.

Individual pixels from the acoustic microscopy raster images will be used to analyze the contributions of capillary forces. Each pixel represents an averaged reflectivity of a finite sampled area of the interface. The sample size is dependent on the radius of the acoustic beam, which was 0.3 mm in this study. If there are several micro-voids and asperities in contact within the pixel, acoustic microscopy is unable to resolve the difference. Thus, individual pixels are likely composed of several interface features. Intuition suggests the possible interface features include surface asperities in contact, water-filled gaps, and void areas that may be filled with gas or vapor.
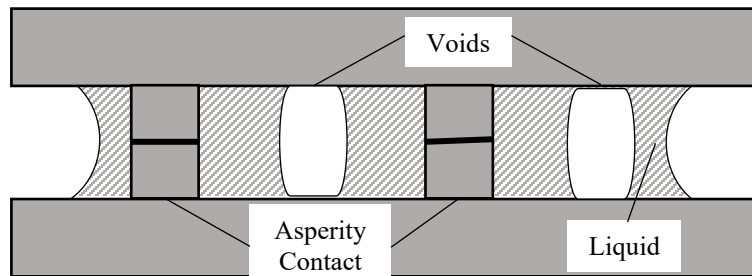
Figure 51. Graphic representation of several micro-features: asperity contact, voids, and liquid-filled gaps (shaded area).

Physically, asperities in contact may be associated with van der Waals forces or hydrogen bonds, while water-filled gaps may be associated with capillary forces and hydrogen bonds. Void areas likely represent areas with no bonding or limited van der Waals forces. Although acoustic microscopy cannot resolve these features outright, analysis with interfacial stiffness can yield insight into the possible features present, which may provide insight into the forces present.

Section 2.5 showed that interfacial stiffness can be derived from acoustic reflectivity of contacting interfaces. Reflectivity of each pixel is tied to the color scale used in this study, shown in Figure 12. Recall that the current interpretation of this scale is dark pixels represent well-contacted areas and very bright pixels represent large void areas of no contact. Thus, dark pixels will be used to determine the interface features that may be present, as very bright pixels (red) likely represent voids. In the color scale, the lowest reflection signal on the scale is 0.1%. Thus, the black pixels shown in acoustic microscopy images, like Figure 21 and Figure 23, correspond to a reflection of 0.1%. Using Equation 10, the associated stiffness for a 0.1% reflection is $K_{black\ pixel} = 1.5 * 10^{18} \left[\frac{Pa}{m^2}\right]$. From the discussion above, this stiffness may be a result of water-filled gaps, voids, and/or contacting surface asperities. Hence, the black pixel stiffness may be represented by the following:

$$K_{black\ pixel} = 1.5 * 10^{18} = aK_{water} + bK_{void} + cK_{asperity} \qquad 15$$

Of the features above, water-filled gaps (capillary forces) will be considered first. Capillary forces arise from adsorbed surface waters on contacting surfaces before they are brought together. The amount of adsorbed water on hydrophilic silicon surfaces increases with higher humidity [28]. In the current experiment, humidity was not strictly controlled but the lab environment was limited to never exceed 50% relative humidity. Literature suggests around 3-4 monolayers per surface as a maximum limit if the relative humidity is below 60% [28]. Thus, a contacted sample would initially have around 6 monolayers of water in the interface. Assuming a monolayer is ~2 Å, that translates to a ~1 nm-thick layer of water in the interface. Furthermore, capillary forces from adsorbed water are expected to pull contacting surfaces together until the interface gap equals the surface roughness of both surfaces. Surface roughness measurements of the samples in this study also showed ~1 nm interface gap should exist. Therefore, it seems

reasonable to approximate a 1 nm-thick water layer in the interface. To determine the theoretical

stiffness that 1 nm of water may provide, we can again turn to the "thin film" model that was

used initially for siloxane in Figure 14. In other words, we may calculate capillary stiffness with

a "thin film" model of water. By doing so, Equation 11 can be used as a theoretical assessment.

Thus, by taking density and speed of sound of water, the stiffness of water can be found.

Table 2. Properties of ice, water, IPA, and air [60] [61] [62] [63].

	$\rho \left[\frac{kg}{m^3}\right]$	$c \left[\frac{m}{s}\right]$	$z = \rho c \left[\frac{MN * s}{m^3}\right]$	$K = \frac{\rho c^2}{h} \left[\frac{Pa}{m^2}\right]$ for 1 nm gap
Ice	~920	~4000	3.68	$1.47 * 10^{19}$
Water	997	~1480	1.48	$2.18 * 10^{18}$
IPA	786	~1200	0.94	$1.13 * 10^{18}$
Air	~1.2	~340	$4.08 * 10^{-4}$	$1.38 * 10^{14}$

Asay *et al.* used IR spectroscopy to show that the first several monolayers of adsorbed

water on hydrophilic silicon are "ice-like" in structure due to the order provided by hydrogen

bonds [28]. Results from Tedjini *et al.* regarding interfacial water diffusion also suggested solid-

like behavior of adsorbed water [48]. Thus, interfacial water may behave more like solid ice than

liquid water in terms of acoustic properties. Acoustically, the water likely behaves as a mix of ice

and water. Although complete ice behavior is unlikely, modeling the water layer as either

complete liquid or complete solid establishes a lower and upper boundary, respectively, for

possible "film" stiffnesses. Table 2 shows the values used in this analysis.

If interfacial water acts completely as liquid water, then $K_{water} = 2.18 * 10^{18} \left[\frac{Pa}{m^2}\right]$. If

interfacial water acts completely as ice, then $K_{ice} = 1.47 * 10^{19} \left[\frac{Pa}{m^2}\right]$. Both values are slightly

higher than $K_{black\ pixel} = 1.5 * 10^{18} \left[\frac{Pa}{m^2}\right]$. Thus, a 1 nm layer of water filling the interface and

some area of voids may account for the dark, "well-contacted" pixels seen in acoustic

microscopy images. An example is shown in Figure 52, below.
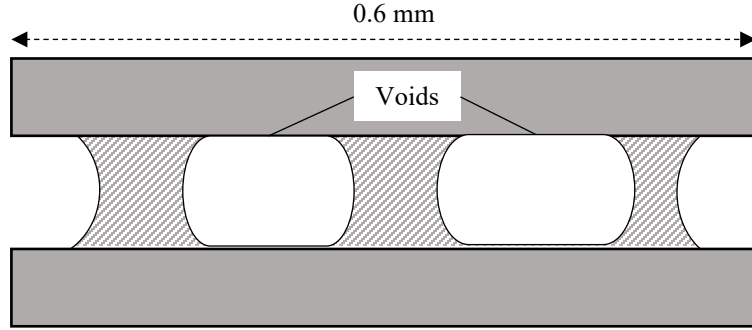
Figure 52. Graphic representation of a single pixel with a water-filled (shaded) interface and several void areas

(white).

      Assuming there are no asperities in contact, then the stiffness of a black pixel can be

simplified to the following:

$$K_{blackpixel} = 1.5 * 10^{18} = aK_{water} + bK_{void} \qquad\qquad 16$$

      The coefficients represent the fraction of the pixel area that is taken by each feature.

Thus, $a + b = 1$. K_{void} will be approximated with density and speed of sound values for air:

$K_{void} \approx K_{air} = 1.38 * 10^{14} \left[\frac{Pa}{m^2}\right]$. Since the stiffness of water has also been determined above,

the coefficients can be found. Using stiffness values for ice, $a_{ice} = 0.1, b_{void} = 0.9$. This

suggests 10% of the pixel area is "ice"-filled gaps and 90% of the pixel area is air-void. Using

stiffness values for water, $a_{water} = 0.69, b_{void} = 0.31$, which suggests 69% of the pixel area is

water-filled gaps and 31% is air-void.

      From a stiffness perspective, the analysis above showed water-filled gaps and voids are

capable of being the only stiffness contributors for dark pixels. As brighter pixels correspond to

larger reflection signals and weaker stiffnesses, they may correspond to sampled areas composed of larger voids and smaller water-filled gaps. Thus, the acoustic microscopy images of room-temperature DB samples, like that shown in Figure 21, may be a combination of only voids and water-filled gaps within each pixel. Therefore, the overall interfacial stiffness of these samples, which was found by taking an average of all pixel stiffnesses, may be a combination of voids and water-filled gaps.

Furthermore, results in Section 4.3.1 showed tight correlation between sample interfacial stiffness and tensile load, which suggests that interfacial water may also be the only strength contributor. Section 2.2.2 showed that the capillary forces associated with water for an ideal parallel-plate model easily exceed 44 kN (10,000 lbf.) for a 38 mm (1.5") diam. sample. If capillary forces still follow the ideal parallel-plate model for strength, then using a 1 nm gap of water suggests 4% of the sample area (for a 38 mm diam. sample) is wetted to reach the sample strengths displayed, which is similar to the pixel area that may be covered by ice-like water (10%). Thus, one could argue that only water is necessary for room temperature direct-bond samples to explain both tensile strengths and acoustic microscopy.

Although the discussion above showed that water-filled gaps and air-voids are the only necessary interface features to explain minimal reflection, asperity contact may also be present in the interface. However, asperity stiffness cannot be found independently by the "thin film model". Physically, asperity contacts likely correspond to van der Waals forces. For hydrophilic silicon surfaces, these forces are likely attractive, rather than repulsive. Therefore, van der Waals forces likely act differently to tensile and compressive forces. Section 2.5 showed that interfacial stiffness is inherently described as the interfacial response to compression that is provided by an incident acoustic pulse. For water and other defined materials, compressive behavior is described

by the bulk modulus, which is used in the "thin film" model for stiffness. However, intermolecular forces like van der Waals forces do not have an easily defined compressive behavior [26]. Therefore, an acoustic (longitudinal) pulse from acoustic microscopy may not be a suitable instrument to describe the tensile strength of van der Waals forces. Though they are excluded in the discussion above, asperity contacts are likely present in the interface, as surface roughness profiles showed surface peaks and valleys that likely result in discrete asperity contacts if surfaces are in intimate contact.

Capillary forces in the interface may force surfaces into intimate contact [29]. Earlier discussion regarding bubble development showed that water may readily diffuse through the native oxide, suggesting some water may leave the interface and saturate the native oxide layer. Recent work from Desomberg *et al.* suggests that water readily diffuses into silicon oxide [35]. Thus, upon initial contact, the interface may be filled with adsorbed surface waters. Over time, some water may diffuse outwards through native oxide and possibly evaporate out of the edges. As the water layer reduces, capillary forces likely draw sample surfaces closer until asperities are in contact. Thus, an interface akin to Figure 51 wherein distinct asperities are in contact may be more appropriate for older samples.

Furthermore, hydrogen bonding likely also plays a role at length scales where capillary forces are more appropriately modeled as hydrogen bonds. However, for similar reasons to van der Waals forces, the stiffness of hydrogen bonds cannot be easily modeled due to their complex behavior in compression [26]. Hydrogen bonding and van der Waals forces may explain the large scatter seen in Figure 27, as they likely are strong in tension but weak in compression. Therefore, acoustic microscopy would be unable to adequately account for their significance in tensile strength. Changes in the prevalence of these forces over time may also be the underlying

reason for the varying results with different age groups. Thus, discriminating by age reduces scatter by restricting the range of variation in stiffness contributors. Analysis of individual age groups, shown in Figure 28 and Figure 29, show scatter reduction.

From the above analysis, the strength of room-temperature direct-bond samples can be attributed to capillary forces of interfacial water, hydrogen bonds where length scales are too small for capillary forces, and van der Waals forces where surface asperities may contact. Although covalent siloxane bonds are not necessarily absent, their presence is not necessary to explain acoustic microscopy and tensile strength results at room temperature.

7.2   Annealed Direct Bond

Annealed samples displayed several characteristics that deviated from the room-temperature samples. From acoustic microscopy, Figure 23 of a sample before and after the annealing process shows an increase in sample reflectivity that was seen in all annealed samples. From tensile tests, Figure 25 showed changes in strength trends over time. Both of these behaviors are addressed below.

7.2.1   Acoustic Microscopy Signature

To drive siloxane bond formation, literature has often cited a low-temperature annealing process [2] [3] [17]. As a consequence, water is also generated that may react with silicon at elevated temperatures to form hydrogen gas. Literature has shown the appearance of hydrogen gas bubbles at elevated temperatures [2] [4] [17]. Our annealing process of 150°C for 30 minutes was expected to yield similar results. Surprisingly, Figure 23 shows there was no new bubble development. Wang *et al.* showed similar behavior for plasma-treated silicon surfaces annealed

at 200°C [64]. However, an unexpected reflection signature did appear that was seen across the entire annealed sample set, regardless of age.

At 150°C, hydrogen-bonded silanol groups in proximity to each other are expected to undergo Equation 6 to form siloxane bonds and water [2]. Over several hours, literature suggests that the water generated by this reaction should dissipate, either by diffusion through native oxide or evaporation out of the edges [2] [3] [4]. Figure 53 shows the interface evolution over time that is proposed in literature, deemed the "dry-out" process [2] [3] [17]. Typically, the dry-out process took place over several hours of annealing at higher temperatures ($\geq 350^oC$) [17]. One hypothesis to explain this dry-out process is that water diffuses out of the interface during the annealing process and leaves void space. The void space, which was previously filled with water, becomes the source of the reflectivity seen in annealed samples. For this to be correct, two parameters must be satisfied: water must be able to diffuse quickly enough at 150°C to leave the interface during the annealing phase, and the resulting void space must be able to account for a 0.5% reflection.
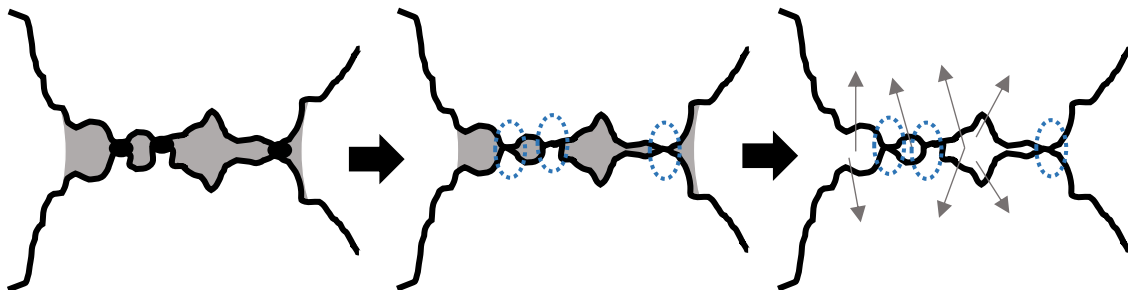
Figure 53. Graphic representation of the understood "dry-out" process when annealing $\geq 150^oC$. Siloxane bonds first form where surface asperities are already in intimate contact. Over time, the interface dries out as water (shown in grey) diffuses through native oxide.

First, the diffusivity of water must be high enough at 150°C for water to diffuse out of the interface in only 30 minutes. The drive-in diffusion models used earlier can be used again to

study this hypothesis. Using the Doremus model for water diffusion in bulk silica glass, the diffusivity of molecular water is estimated to have an upper limit of $D = 3 * 10^{-13} \left[\frac{cm^2}{s}\right]$ at 150°C [56]. Using Equation 13, an approximation of surface concentration of water after 30 minutes can be found. The total concentration of water, S, is still estimated to be $\sim 2 * 10^{15} \left[\frac{molec}{cm^2}\right]$ for 3 monolayers.
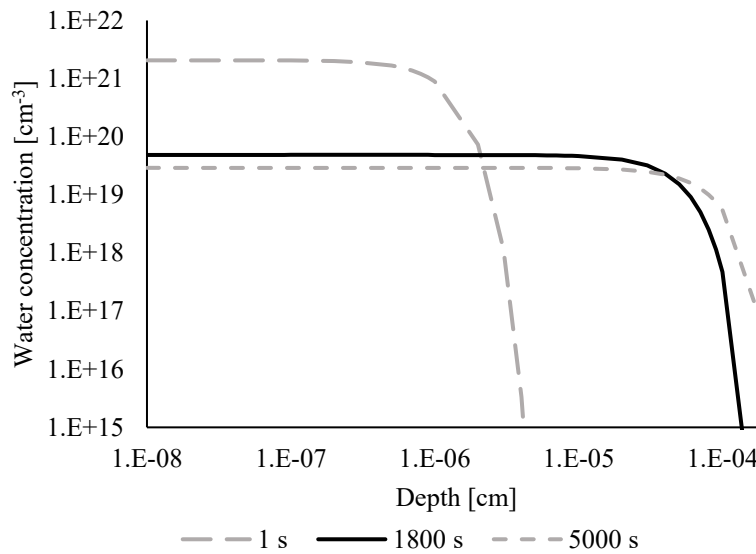
Figure 54. Diffusion profile of water in silica using dopant drive-in diffusion assumptions and a constant diffusivity extrapolated from the Doremus model for 150°C. Several annealing times are simulated to show changes in water surface concentration. The black line represents the annealing time used in this report.

With 30 minutes of annealing, surface concentration reduces to 2% when compared to surface concentration for a 1 second anneal. Figure 54 shows how surface concentration drops from $\sim 2 * 10^{21}$ to $\sim 5 * 10^{19}$ cm^{-3} after 30 minutes of annealing. Thus, a low temperature annealing procedure for 30 minutes can potentially drive a significant amount of water away from the interface. Furthermore, molecular water should have diffused through the entire native oxide layer by the end of the annealing procedure. However, earlier discussion of room-temperature samples suggested that the reaction of water with native silicon does not readily

79

occur at low temperatures [38]. If diffused water cannot react with native silicon, then the solubility limit of water in silica glass at this temperature and interface vapor pressure may limit the amount of water that can diffuse into the native oxide. However, water may also diffuse laterally and evaporate from the edges, so a low solubility may not entirely refute a dry-out process. Future work is necessary to determine if the solubility of water in silica glass is sufficient to store the interfacial water that is driven from the interface.

Water diffusion only satisfies one part of the dry-out hypothesis. Interfacial stiffness must also be considered. It has been shown above that the associated stiffness for a reflection coefficient of 0.005 is $3.08 * 10^{17} \left[\frac{Pa}{m^2}\right]$. To interpret this stiffness value, the spatial resolution of acoustic microscopy is again taken into consideration. As described in the earlier discussion regarding room temperature direct-bond samples, each pixel area likely involves several interface features that cannot be visually resolved by the acoustic microscope. Although there are many complex intermolecular interactions occurring in the interface, the following discussion will take some liberties in approximations and only account for three interface features to model the dry-out process: asperity contacts, water-filled gaps, and voids. Literature suggests that siloxane should form at asperity contacts, water should leave, and void space should increase as samples are annealed [17]. Hence, the interface may follow the equation for spring stiffness per unit area below.

$$K_{total} = 3.08 * 10^{17} = aK_{asperity} + bK_{water} + cK_{void} \qquad 17$$

From a physical point of view, Equation 17 is representative of a pixel area, wherein total stiffness is composed of a fraction of several stiffness contributors. The coefficients are, therefore, fractions of the pixel area that represent the contribution of each parameter to the total

stiffness. Thus, the sum of the coefficients should represent the area of one pixel. For simplicity, the area of a pixel will be represented as unity, shown below.

$$a_{asperity} + b_{water} + c_{void} = 1 \qquad\qquad 18$$

Equation 17 can be constrained further by using the "thin film" model of Equation 11 to calculate each stiffness as independent variables. Asperity stiffness will be approximated with a "thin film" model of siloxane as literature expects asperity contacts to become siloxane bonds at 150°C [2] [3] [17]. Assuming a 1 nm gap: $K_{asperity} \approx K_{siloxane} = 7.8 * 10^{19} \left[\frac{Pa}{m}\right]$. The "thin film" of water used in the discussion of room-temperature samples will be used again for this analysis: $K_{water} = 2.18 * 10^{18} \left[\frac{Pa}{m^2}\right]$. However, earlier discussion also showed interfacial water may behave acoustically like ice, so $K_{ice} = 1.47 * 10^{19} \left[\frac{Pa}{m^2}\right]$ will also be considered to establish an upper boundary for water stiffness. K_{void} will again be approximated with density and speed of sound values for air: $K_{void} \approx K_{air} = 1.38 * 10^{14} \left[\frac{Pa}{m}\right]$. Realistically, voids may be filled with some hydrogen gas as literature expects diffused water to react with elemental silicon at 150°C [2] [3]. At face value, the stiffness of air-void is several magnitudes lower than the total stiffness, suggesting its contribution to stiffness is negligible. Therefore, stiffness is mostly dependent on water-filled gaps and asperity contacts:

$$K_{total} = 3.08 * 10^{17} \approx aK_{siloxane} + bK_{water-ice} \qquad\qquad 19$$

There now remain three undetermined coefficients and only two independent equations, Equation 18 and Equation 19. If either coefficient in Equation 18 can be set to 0, then the problem may be fully constrained. If $a_{siloxane} = 0$, that models a system wherein some water remains in the interface ($0 < b < 1$) and some air-void is present, but siloxane has not formed. If $b_{water} = 0$, that models a system wherein dry-out has completely occurred and the interface is

only air-void and all asperity contacts have become siloxane bonds. Analysis of these two constrained models may provide insight into whether the dry-out process is a reasonable explanation for the increased reflection in annealed samples.

In a complete interface dry-out scenario, Equation 19 is fully constrained as $b_{water} = 0$. In this case, $a_{siloxane} = 0.004$ and $c_{air} = 0.996$. Physically, this suggests that 0.4% of the pixel area is asperity contact in the form of siloxane bonds and 99.6% of the pixel area is air-void. This would suggest very little siloxane can form. Since siloxane likely can only form at asperity contacts, this suggests at least 0.4% of the pixel area is asperity contact. However, surface micro-roughness measurements suggest asperity contacts should cover an area roughly an order of magnitude higher, suggesting that most asperity contacts did not form siloxane bonds. Furthermore, complete water dry-out is also unlikely as ambient storage would likely re-introduce some water. If other stiffness contributors are present, that would result in further reduction of $a_{siloxane}$. Therefore, this suggests siloxane presence may be minimal.

A different scenario can be considered wherein no siloxane bonds form. Equation 19 is again fully constrained as $a_{siloxane} = 0$ in this instance. If interfacial water acts completely as liquid water, $b_{water} = 0.14$ and $c_{void} = 0.86$. Physically, this suggests 14% of the pixel area is water and 86% is air-void. If interfacial water acts as ice, $b_{ice} = 0.02$ and $c_{void} = 0.98$, suggesting 2% of the pixel area is ice-water and 98% is air-void. Recall that analysis of black pixels in room-temperature samples suggested 10% ice coverage or 69% liquid water coverage. Since acoustic microscopy showed black pixels (0.1% reflection) dominated room-temperature samples and purple pixels (0.5% reflection) dominated annealed samples, this analysis suggests interfacial water is reduced in annealed samples compared to room-temperature samples. From

the discussion above concerning the diffusivity rate of water and the solubility limit of water in silica glass, it seems reasonable to surmise that some water must remain in the interface. Thus, this scenario seems reasonable. Furthermore, this suggests siloxane bond formation is not necessary to explain interfacial stiffness.

Through literature values of water diffusivity and analysis of interfacial stiffness, the discussion above has shown that the interface dry-out process in literature is a reasonable explanation for the increased reflectivity seen in annealed direct-bonded samples. However, in a deviation from the dry-out process, the discussion above has shown that siloxane bonds may not be present after a low-temperature annealing process at 150°C for 30 minutes.

7.2.2 Annealed v RT Strength Differences (Direct Bond)

From an acoustic microscopy standpoint, siloxane bond presence is unlikely in annealed samples. However, strength results showed a large difference in load capacities between the annealed and non-annealed sample sets that was shown in Figure 25. In addition, annealed and non-annealed samples show different linear slopes. If siloxane bonds have not formed, there must be a different mechanism responsible for these behaviors. It is possible that van der Waals forces are the culprit. As water is driven out of the interface and is replaced by voids, van der Waals forces likely increase as Figure 5 shows van der Waals forces in air are several orders of magnitude higher than those in water. Furthermore, as surface asperities draw closer together, the local gap distance may fall into single angstroms. Since van der Waals forces grow $F_{vdw} \propto d^{-3}$, reductions in gap distance can result in very high van der Waals forces. For example, an air medium with asperity gap of 5 angstroms leads to ~7000 lbf. (for a 38 mm diam. sample). Though asperity contact likely does not appear across the whole interface, van der Waals forces

are still likely a significant contributor. This model does not, however, explain why strength in annealed samples seems to fluctuate between weeks. It is possible that the fluctuations seen in Figure 24 are simply an artifact of statistics with limited sample size.

The increased reflection in the interface also severely reduced average interfacial stiffness. Figure 30 shows how stiffness values decreased by nearly an entire order of magnitude. As stated earlier, the reduction is likely due to the high reflection across sample interfaces. Since our analysis used an average stiffness value from every pixel in a sample raster, the increased reflection drastically lowered each sample's average. In future works, it may be more applicable to instead track the area of high stiffness regions. This may provide a better indicator of stiffness and strength contributors.

7.3   Room Temperature Alcohol-Assisted

Results from the room-temperature alcohol-assisted samples showed several unexpected behaviors that warrant further analysis. First, acoustic microscopy of the alcohol-assisted samples showed non-zero interface reflectivity in the young samples that seemed to slowly disappear with age. Furthermore, interfacial bubbles did not appear in any of the room-temperature samples, even after multiple months.

7.3.1   RT Bubble Development (Alcohol-Assisted)

As stated earlier, acoustic microscopy showed no bubble development in any of the alcohol-assisted samples without annealing. This remained true for samples aged beyond one year. This result was surprising, as the alcohol-assisted samples were expected to behave similarly to the direct-bond samples. The previous discussion on room temperature direct-bond

samples attributed the eventual appearance of bubbles to liquid water cavitation. The lack of bubbles in alcohol-assisted samples suggests the presence of isopropyl alcohol changed the cavitation environment in the interface. Though the exact changes are unclear at this time, a literature review of isopropyl alcohol behaviors may provide insight.

Semiconductor literature on Marangoni vapor drying suggests that IPA is effective in removing surface waters [65]. This behavior likely arises from the high solubility of water in IPA at room temperature. In alcohol-assisted samples, it is possible the introduction of IPA to the interface mixes with adsorbed surface water to form an alcohol solution. The presence of an alcohol solution likely changes the capillary forces present in the interface. Recall that cavitation typically occurs due to the local pressure within the liquid dropping below the saturated vapor pressure of the species, making the formation of a gas bubble thermodynamically favorable [51] [52]. In Section 2.2.2, it was shown that capillary forces are generally dependent on the surface tension of the liquid-air interface. Since pure water possesses a higher surface tension than an alcohol-water solution, it follows that the capillary forces that arise from an alcohol-water solution are likely reduced. Thus, the presence of alcohol certainly affects the pressure environment within the interface. It is possible the pressure environment in an alcohol-water solution is such that cavitation is suppressed. Research from Tas *et al.* and Duan *et al.* have shown that nano-sized bubble nucleation by cavitation is not an easily quantifiable process [51] [52]. Thus, it is currently unclear how and if an alcohol-water solution reduces cavitation events. Alternatively, it is possible that cavitation does occur on the nanometer scale, but unlike the direct-bond samples, bubbles in an alcohol-assisted sample do not readily migrate along the interface to coalesce into a detectable bubble.

Further work is necessary to probe potential differences between alcohol-assisted samples and direct-bond samples.

7.3.2 Strength Contributors of RT Alcohol-Assisted Samples

To better understand the effects of alcohol presence in the interface, a separate experiment involving Fourier-transform IR (FTIR) spectroscopy was performed to track the presence of IPA in the interface over time. The procedures used by Feijoo *et al.* were utilized in this experiment [37]. The multiple internal transmission (MIT) setup required 1 mm-thick silicon wafers cut to 50x20 mm to allow light to pass through the interface 25 times.
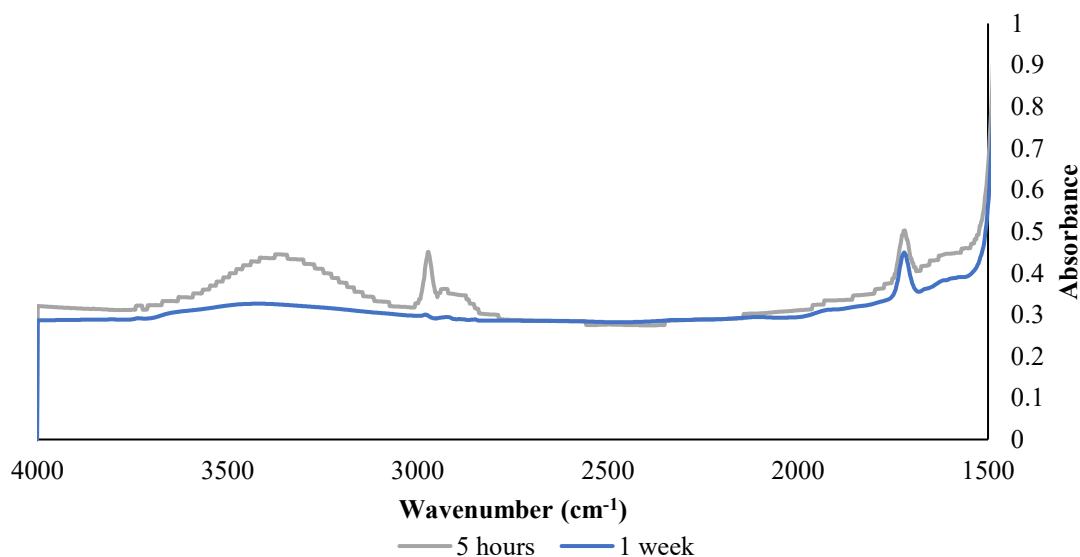
Figure 55. IR spectrum of an alcohol-assisted, bonded (100) silicon wafer at 5 hours after contact and 1 week after contact from 4000-1500 cm^{-1} as silicon is only transparent in IR up to 1500 cm^{-1}. Different background files were used for each scan, which may explain the discrepancy in baseline absorbance.

The infrared absorption bands attributed solely to IPA, namely the hydrocarbon peaks around 2900 cm^{-1}, mostly disappeared over the course of 1 week of ambient aging. Figure 55

also shows the broad band around 3400 cm^{-1} associated with -OH groups also decreases. The decrease is likely associated with IPA evaporation. Although the silicon geometry used in the FTIR was different than the bulk parts, this adds further strength to the claim that interfacial alcohol content in the interface decreases over time. Furthermore, this suggests fluid flow in the interface can occur over several days. However, alcohol may not completely leave. Figure 57 in Section 7.4.1 shows a small hydrocarbon signal remains after 4 weeks of aging.

Analysis of the direct-bond samples utilized interfacial stiffness to approximate the fractional pixel coverage of water-filled gaps and voids by modeling "thin films" of water and air, respectively. However, the same analysis technique should not be applied to alcohol-assisted samples as the results in Section 5.3 showed no correlation between sample strength and interfacial stiffness. Therefore, any conclusions that may be drawn from stiffness analysis of alcohol-assisted samples cannot be correlated to strength. However, based on analysis of the direct-bond samples at room temperature, it seemed that water-filled gaps, voids, and asperity contacts were sufficient to fit the direct-bond data. It seems likely that a similar interface environment exists in room-temperature alcohol-assisted samples. The main difference between the two, which also may explain differences in sample strength, is the presence of IPA. Figure 56 shows a graphic representation of a likely scenario for the room-temperature samples, in which there are discrete asperities in contact to provide van der Waals contributions and liquid-filled voids to provide capillary contributions.
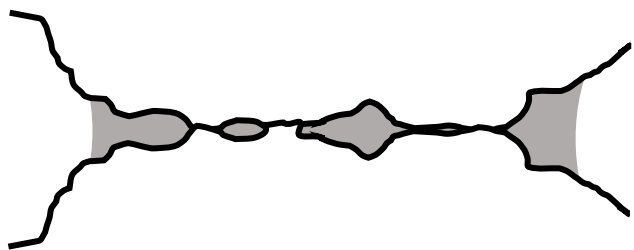
Figure 56. Graphic representation of asperity contacts and liquid in the interface. Shaded grey area represents liquid, which may be an alcohol-water solution for alcohol-assisted samples.

Strength data shown in Figure 36 shows that the 1-week AA age group held higher loads than the 2-week and even 3-week age groups. One hypothesis to explain this strength degradation is changes in capillary strength from decreasing alcohol in the interface. Figure 7 shows that a fully wetted interface with IPA can theoretically sustain up to ~5000 lbf (~19 MPa for a 38 mm diam. sample), which can account for the strength displayed by the 1-week age group. Figure 55 shows alcohol evaporation out of the interface over time. Thus, capillary contributions should intuitively decrease if liquid-filled voids become gas-filled or vapor-filled voids.

Due to the complex interactions occurring at the interface during alcohol evaporation, it is difficult to assign the strength trends shown in Figure 36 to any definitive processes. However, the reported strengths of this sample set can be explained solely by capillary forces.

7.4   Annealed Alcohol-Assisted

Annealing the alcohol-assisted samples resulted in a severe increase in sample acoustic reflectivity. However, the behavior was markedly different than the annealed direct-bond samples in terms of reflection amplitude and reflection uniformity within the interface. Whereas the direct-bond samples showed a uniform increase in reflectivity within each sample after annealing (Figure 23), the alcohol-assisted samples showed a "patchiness" within each interface (Figure 37). Furthermore, the changes from annealing seen in Figure 37 may be correlated to the changes in tensile strengths shown in Figure 39. These behaviors are discussed below.

Analysis of annealed direct-bond samples utilized interfacial stiffness to establish a possible model of the interface. However, as explained in the previous section, this analysis method cannot be applied to alcohol-assisted samples as results in Section 5.3 showed no correlation between stiffness and tensile strength. Therefore, the discussion below draws from other studies done with IR spectroscopy and the model of direct-bond samples to establish possible models of alcohol-assisted samples.

7.4.1   Acoustic Microscopy Signature

Acoustic microscopy of the annealed alcohol-assisted sample set showed large areas of high reflectivity develop throughout the entire set. The degree of reflectivity is more severe than the reflectivity seen in annealed direct-bond samples. A comparison of Figure 23 to Figure 37 shows clear differences. Thus, the underlying mechanism responsible for the behavior of annealed alcohol-assisted samples is also likely different. One hypothesis is interface de-bonding due to increased alcohol vapor pressure at elevated temperatures.
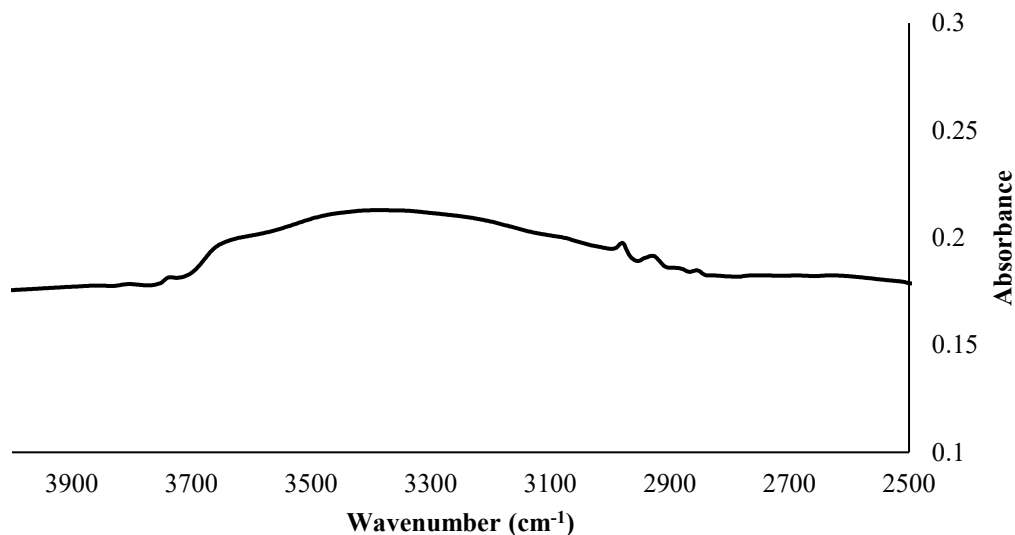
Figure 57. IR spectrum of a RT, alcohol-assisted, bonded (100) silicon wafer 6 months after contact from 4000-2500 cm^{-1}.

Results from IR spectroscopy of alcohol-assisted silicon wafers suggest that a small amount of alcohol can remain in the bonded interface for long periods of time. Figure 57 shows a small absorbance band at ~2950 cm^{-1} that may be attributed to carbon-hydrogen bonds [42]. In contact-bonded wafers, the hydrocarbon contamination on the surfaces prior to contact is minimal. It was found, however, that contamination on the outer surfaces contributed to this absorbance band. To minimize outer surface contamination, the outer surfaces were subjected to the same low power plasma treatment used for the contacting surfaces and the clean sample was immediately placed into the spectrometer. Figure 57 shows the carbon-hydrogen absorbance band is still present after 6 months of aging in an ambient environment. As contamination is minimal, the absorbance band is likely due to alcohol presence. Thus, it is possible that remaining alcohol present in the interface is responsible for the annealing behavior that was seen in all age groups.

IPA has a low boiling point in ambient atmosphere, which predicts a high vapor pressure at 150°C. The alcohol vapor may then contribute to crack growth within the interface by both reducing surface energy of the contacting surfaces and filling and pressurizing the void space in the interface. Literature on Marangoni vapor drying for wafer cleaning purposes suggest that IPA vapor can reduce surface energy [65]. In that application, surface energy reduction was beneficial in removing particulates. In this case, surface energy reduction leads to weaker intermolecular forces that were holding the surfaces in contact. With increased pressure in the interface from the vapor, this may lead to de-bonding.

However, as the annealed samples are cooled to room temperature, the isopropyl alcohol vapor may condense and the pressure at the interface recede. There must then be a reason why the surfaces do not go back into contact upon cooling to room temperature. This may be explained by the lack of attractive forces that initially brought the surfaces together. Namely, capillary forces from the initial alcohol are not nearly as significant as IR spectroscopy has shown most of the alcohol leaves the interfaces. Furthermore, mechanical theory posed by Maszara *et al.* showed that the ability for contacting surfaces to eliminate voids depends on the size of the void [22]. Figure 4 shows the maximum void height to radius ratio that can be closed by contacting surfaces. If the de-bonded area becomes too large, the surfaces may not be able to close again.

This hypothesis depends on vaporization of alcohol at 150°C and sufficiently high alcohol vapor pressure to overcome the bond strengths of contacted areas. At 1 atm and 150°C, alcohol readily vaporizes. However, the pressure environment inside the bonded interface is unclear and it may not be conducive to alcohol vaporization at 150°C. Furthermore, additional experiments are necessary to determine whether and to what degree IPA vapor decreases surface energy to determine the pressure required to de-bond contacting areas.

7.4.2 *Annealed Strength (Alcohol-Assisted)*

Strength tests and acoustic microscopy of annealed alcohol-assisted samples both showed trends over time. In tensile strength, Figure 38 showed the annealed alcohol-assisted samples exhibited a near-linear increase in strength with every week of pre-annealed aging. Figure 58 shows the area of post-annealed de-bonding seen through acoustic microscopy became less severe with older samples. Therefore, the continual increase in strength over time may be

correlated to less severe de-bonding over time from alcohol vapor. The younger samples often showed larger areas of higher reflectivity than the older samples, which corresponds to larger areas of void. Furthermore, the 1-week samples did not survive the annealing treatment, which may be an indication that alcohol vapor pressures in 1-week samples were high enough to completely de-bond the samples. As IR spectroscopy showed decreased alcohol presence over time, it would follow that less alcohol in the interface may lead to varying vapor pressures and less de-bonding.
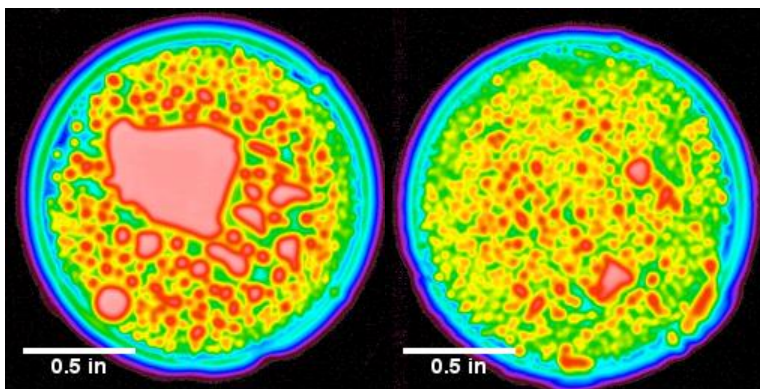
Figure 58. Acoustic microscopy images of two alcohol-assisted samples after annealing at 150°C for 30 minutes. (Left) Sample aged for 3 weeks at RT. (Right) Sample aged for 6 weeks at RT. These images correspond to longitudinal reflections from the interface.

7.5   Alcohol-Assisted vs. Direct Bond

Comparison of the alcohol-assisted samples to the direct-bonded samples yields key differences in behavior. The discussions and results above have already highlighted some differences in strength trends, annealing behavior, and time dependencies. Further comparison of the two may yield a clearer picture of their different behaviors.

7.5.1 Acoustic Microscopy Differences

From acoustic microscopy, it has already been shown that the two methods respond differently in time at room temperature. Interfacial bubbles routinely appear in the direct-bond samples after 4 weeks in ambient atmosphere, whereas the alcohol-assisted samples did not show interfacial bubble development even after 6 months. As the bubbles in direct-bond samples may be due to liquid cavitation, this suggests differences in the pressure environment within the interface that possibly prevent bubble nucleation in alcohol-assisted samples. Acoustic microscopy also showed the two methods, on average, differed in particulate concentration. The alcohol-assisted sample sets showed less particulate coverage than the direct-bond samples. It is possible that the alcohol flushed the particulates as much of the initial 10 μL IPA was squeezed out of the interface during initial contact. In the semiconductor industry Marangoni drying leads to beneficial cleaning effects from the low surface tension of isopropyl alcohol [65] [66]. Reduction in particle presence and removal of adsorbed water are two common characteristics within Marangoni vapor drying [65] [66].

The two sample sets also behaved differently to annealing at 150°C. Images of the annealed sample sets showed distinct behavioral differences between alcohol-assisted and direct bond samples. As mentioned earlier, the alcohol-assisted set showed large bubble formation in the interface that, in severe cases, acted to completely de-bond the interface. Meanwhile, the direct-bond set showed a consistent ~0.5% reflectivity across sample interfaces. The deviation in annealing response is likely a result of isopropyl alcohol in alcohol-assisted samples. IPA may have removed surface water from the interface as it was flushed from the edges and the vapor pressure of the remaining IPA may have increased upon annealing in the alcohol-assisted set.

Meanwhile, dry-out likely occurred in the direct-bond set that led to the consistent reflectivity from the interface.

7.5.2 *Strength Differences*

In theory, particulates should negatively affect the load capacity of contacted samples as it decreases the potential surface area for bonding to occur and increases the potential for peel-failure initiation around a particulate. Peel failure is akin to crack growth and would result in failure at lower loads than a pure tensile failure. It is possible that particulate presence contributed to the large scatter in strength. Despite higher presence of particulates and larger areas of un-bond shown by acoustic microscopy, room temperature direct-bond samples still exhibited larger tensile loads than the room temperature alcohol-assisted samples.

Figure 59. Comparison of RT direct bonded and alcohol-assisted (100) bulk silicon samples by age in terms of flatwise tension. Samples aged for longer than 4 weeks were grouped into one column as no strength changes were seen.

Figure 59 shows the discrepancy in load capacity between the two sample sets. The 1 and 2 week sets, especially, show large differences in load capacity due to the high presence of isopropyl alcohol in the interface of alcohol-assisted samples. By 3 weeks, however, the sample sets seem to converge in load capacity and remain similar at 4 weeks. However, the direct-bond samples display a higher maximum load capacity than the alcohol-assisted samples in all age groups.

The two sample sets also reacted differently to low-temperature annealing. Whereas the alcohol-assisted samples displayed significant bubble development, the direct-bond samples developed an unexpected reflection signature that was uniformly seen in the entire direct-bond sample set. The varied reaction to annealing suggests chemical differences in the interface. These differences likely contributed to significant variation in load capacities.
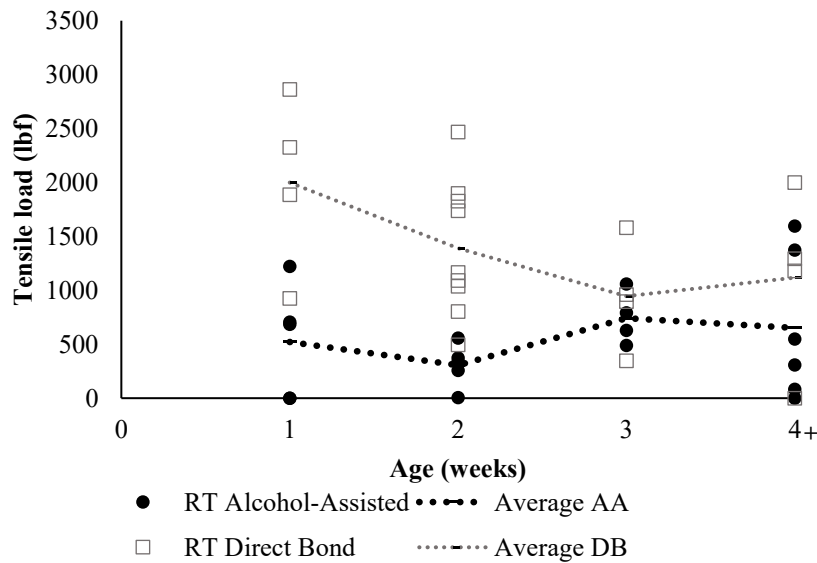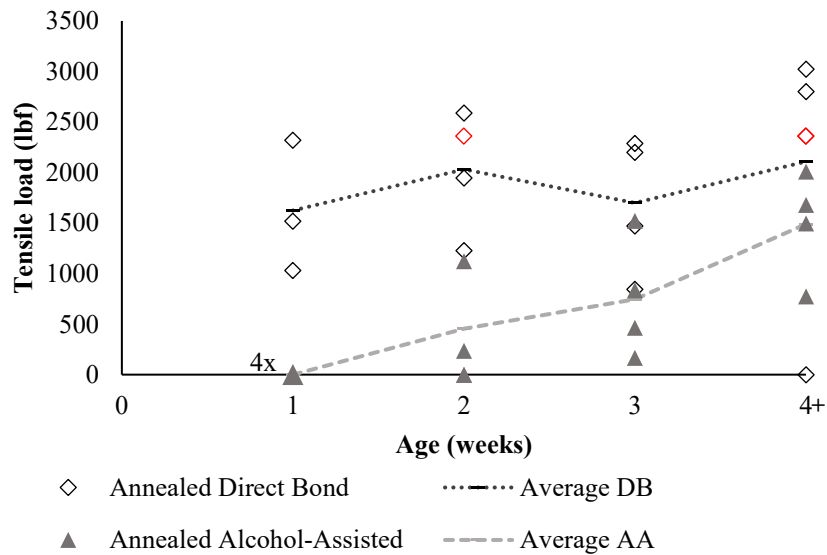

Figure 60. Comparison of annealed direct-bonded and alcohol-assisted (100) bulk silicon samples by age in terms of flatwise tension. Samples aged for longer than 4 weeks were grouped into one column as no strength changes were seen. The red diamond markers indicate annealed samples that reached the 10 kN (~2250 lbf.) load cell limit and are

not indicative of the actual tensile capacities of the samples. The large marker for the 1-week alcohol-assisted set represents 4 separate samples that all failed during the annealing process.

Figure 60 shows the large separation in load capabilities of each sample set. At 1 week, the direct-bond samples exhibited high loads, whereas none of the alcohol-assisted samples could sustain any applied load. The load disparity eventually converges at the 4-week data set, although the direct-bond sample strength is likely larger than what is shown in the graph. As several samples in the 4+ week direct-bond data set were not pulled to failure (red data point), the reported average is skewed lower. The high strengths of the 1-week annealed direct-bond samples in comparison to the 1-week annealed alcohol-assisted samples may be attributed to varying annealing responses. Previous discussion of the annealed alcohol-assisted samples posed the hypothesis that high IPA vapor pressure at 150ºC is responsible for de-bonding large sections of the interface during the annealing process, leading to strength reduction. In contrast, annealing direct-bond samples likely resulted in the interfacial dry-out process seen in literature and shown in Figure 53, with the exception that siloxane may not have formed [17]. Previous analysis in Section 7.2 showed that siloxane bonds would have to cover a miniscule amount of the interface area in order to satisfy the interfacial stiffness of direct-bond samples.

7.6   Suggested Models of Alcohol-Assisted and Direct-Bond Processes

At room temperature, the presence of interfacial siloxane bonds is not necessary in either sample set to fit strength and acoustic stiffness results. The strengths of both sets at room temperature can be modeled just by capillary and van der Waals forces. The suggested model for room-temperature direct-bond samples is capillary force from adsorbed water and van der Waals forces, or hydrogen bonds between silanol groups, where surface asperities are in intimate

contact. Furthermore, bubble presence seen in the room temperature direct-bond samples is attributed to liquid cavitation rather than hydrogen gas, as it has been demonstrated above that water does not readily react with silicon at room temperature. Without this reaction, hydrogen gas does not develop. Similarly, the suggested model for room temperature alcohol-assisted samples is a combination of capillary force from IPA-water solution and van der Waals forces where surface asperities are in intimate contact.

As with the room temperature samples, siloxane bond presence is not required to explain the behavior of samples annealed at $150^{o}C$ for 30 minutes. Discussion in Section 7.2 showed that siloxane bonds would have to cover a miniscule amount of the interface area in order to satisfy the interfacial stiffness of direct-bond samples. Thus, the suggested model for annealed direct-bond samples follows literature of interface dry-out, with the exception of minimal, if any, siloxane formation. Instead, strength increases may come from van der Waals forces. Meanwhile, the vapor pressure of IPA in alcohol-assisted samples may have increased at elevated temperatures and de-bonded sections of the interface. Although siloxane bond formation is not ruled out in alcohol-assisted samples, it is likely further limited than the direct-bond samples due to large de-bonded areas that prevent asperity contact. Therefore, the suggested model for annealed alcohol-assisted samples is increasing IPA vapor pressure expanding void areas as well as a possible increase in van der Waals contributions that mirrors the direct-bond samples.

8. Conclusion & Future Work

Flatwise tensile tests have shown large variability in strength across aging time, bond method, and low-temperature annealing. Although the tensile tests were designed for strict tensile failure at the interface, analysis of failed surfaces and acoustic microscopy suggests other failures occurred that could not be prevented. Some samples failed through the bulk silicon rather than the interface, suggesting local strengths in the interface exceeded the strength of the silicon substrate. Others likely initiated peel failure due to particulates near the edge of the bonded interface and failed cleanly across the bonded interface. The probable presence of significant and varying capillary forces from interfacial water and isopropyl alcohol also added to the variability in load capacity.

Despite large scatter in tensile data, it has been shown that direct-bonded samples can reliably sustain at least 500 lbf. of tensile load (~2 MPa for a 38 mm diam. sample) without any annealing treatment, which can be sufficient to satisfy requirements for bonded silicon optics. Annealing at 150°C for 30 minutes was shown to have a positive effect on the tensile load capacity of both sample sets, with the direct-bond samples reliably exceeding 1000 lbf. (~4 MPa for a 38 mm diam. sample) in all age groups. Although there are benefits in using an alcohol-assisted process, it has been shown to be comparatively weaker than the direct-bond samples for samples aged up to 1 month, including those that underwent a low-temperature anneal. In addition, interfacial bubbles were seen via acoustic microscopy after a 1-month ambient aging period for the direct-bond samples but not for alcohol-assisted samples. In this work, bubbles were attributed to liquid cavitation. The lack of bubbles in alcohol-assisted samples points to different interface chemistry between direct-bond and alcohol-assisted samples. Future work

should be performed to elucidate the exact mechanisms behind alcohol-assisted bonding regarding surface energy reduction and water absorption by isopropyl alcohol. Work should also be pursued to confirm the mechanism responsible for room-temperature bubble development in the direct-bond samples.

Contact quality was assessed with acoustic microscopy. Through classical spring models, we have shown the average acoustic reflectivity of a bonded interface can be used to calculate average interfacial stiffness by established theory. Furthermore, we have shown that an upper boundary for interfacial stiffness can be found by modeling a theoretical perfectly-bonded sample as a thin film of siloxane in the interface. By taking the ratio of average interfacial stiffness to the upper boundary, a common stiffness scale can be used to judge the quality of bonded samples.

We have shown through simple linear regression models that interfacial stiffness plotted on the common stiffness scale is correlated to the tensile load capacity of direct-bond silicon samples but not of alcohol-assisted silicon samples. Future experiments should be performed to understand the failures of this model and develop an effective model for alcohol-assisted samples. We have shown that the spring model can be applied to both room-temperature and annealed direct-bond sample sets. However, annealing condition and age must be separated to reduce deviation from the linear model, as sample strengths showed clear time and temperature dependencies. Isolating for both parameters, direct-bond sample strengths can be correlated to interfacial stiffness within ~250 lbf. (~1 MPa for a 38 mm diam. sample).

Room temperature and low temperature bulk silicon contact bonding are important processes that may allow for the fabrication of complex optical geometries in space and

astronomy applications. It has been shown here that a plasma-activated, direct-bond process can satisfy the tensile load capacities required for numerous space applications and acoustic microscopy may be used in future endeavors as a quantitative non-destructive technique to evaluate critical contact-bonded parts.

References

[1] S. Pellicori, "Optical bonding agents for IR and UV refracting elements," in *Proc. SPIE 1535, Passive Materials for Optical Elements*, San Diego, 1991.

[2] Q. Y. Tong and U. Gösele, Semiconductor Wafer Bonding: Science and Technology, John Wiley & Sons, Inc., 1999.

[3] R. Stengl, T. Tan and U. Gösele, "A Model for the Silicon Wafer Bonding Process," *Jpn. J. Appl. Phys.,* vol. 28, no. 10, p. 1735–1741, 1989.

[4] Y. Backlund, K. Ljungberg and A. Soderbarg, "A suggested mechanism for silicon direct bonding from studying hydrophilic and hydrophobic surfaces," *J. Micromech. Microeng,* vol. 2, no. 3, p. 158–160, 1992.

[5] D.-H. Gwo, "Hydroxide-Catalyzed Bonding,". United States of America Patent 6548176B1, 15 April 2003.

[6] W. P. Maszara, "Silicon-On-Insulator by Wafer Bonding: A Review," *J. Electrochem. Soc.,* vol. 138, no. 1, p. 341, 1991.

[7] F. Fournel, X. Baillin, S. Cheramy, P. Leduc and L. Sanchez, "Method for Direct Bonding with Self-Alignment using Ultrasound". United States of America Patent 10,438,921B2, 18 October 2019.

[8] J. J. Wright and D. E. Zissa, "Optical Contacting for Gravity Probe Star Tracker," National Aeronautics and Space Administration (NASA), 1984.

[9] M. Phelps, M. M. Reid, R. Douglas, A. M. v. Veggel, V. Mangano, K. Haughian, A. Jongschaap, M. Kelly, J. Hough and S. Rowan, "Strength of hydroxide catalysis bonds between sapphire, silicon, and fused silica as a function of time," *Phys. Rev. D,* vol. 98, no. 12, p. 122003, 2018.

[10] S. Aston, M. Barton, A. Bell, N. Beveridge, B. BLand, A. Brummitt, G. Cagnoli, C. Cantley, L. Carbone, A. Cumming, L. Cunningham, R. Cutler, R. Greenhalgh, G. Hammond, K. Haughlan, T. Hayler, A. Hepstonstall, J. Heefner and D. Hoyland, "Update on quadruple suspension design for Advanced LIGO," *Class. Quantum Grav,* vol. 29, no. 23, p. 235004, 2012.

[11] A.-M. A. v. Veggel and C. J. Killow, "Hydroxide catalysis bonding for astronomical instruments," *Advanced Optical Technologies,* vol. 3, no. 3, 2014.

[12] T. Turner and P. Casnedi, "Novel Bonding Technology Improves Optical Assemblies," *EuroPhotonics,* Mar 2013.

[13] D. A. Girou, B. Landgraf, R. Guenther, M. J. Collon and M. W. Beijersbergen, "Bond strength of 3D-stacked monocrystalline silicon X-ray mirrors," in *5th International Workshop on Low Temperature Bonding for 3D Integration (LTB-3D)*, Tokyo, 2017.

[14] B. Landgraf, R. Gunther, G. Vacanti, N. Barriere, M. Vervest, D. Girou, A. Yanson and M. Collon, "Direct Bonding of Multiple Curved, Wedged, and Structured Silicon Wafers as X-Ray Mirrors," *ECS Transactions,* vol. 75, no. 9, pp. 331-338, 2016.

[15] G. DeVine, B. Ware, D. M. Wuchenich, R. E. Spero, W. M. Klipstein and K. McKenzie, "Techniques for Solution-Assisted Optical Contacting," *NASA Tech Briefs,* p. 36, May 2012.

[16] T. Plach, K. Hingerl, S. Tollabimazraehno, G. Hesser, V. Dragoi and M. Wimplinger, "Mechanisms for room temperature direct wafer bonding," *Journal of Applied Physics,* vol. 113, no. 9, p. 094905, 2013.

[17] C. Ventosa, F. Rieutord, L. Libralesso, C. Morales, F. Fournel and H. Moriceau, "Hydrophilic low-temperature direct wafer bonding," *Journal of Applied Physics,,* vol. 104, no. 12, p. 123524, 2008.

[18] W. Maszara, G. Goetz, A. Caviglia and J. McKitterick, "Bonding of silicon wafers for silicon-on-insulator," *Journal of Applied Physics,* vol. 64, no. 10, pp. 4943-4950, 1988.

[19] B. Muller and A. Stoffel, "Tensile strength characterization of low-temperature fusion-bonded silicon wafers," *J. Micromech. Microeng.,* vol. 1, no. 3, p. 161–166, 1991.

[20] S. N. Farrens, J. R. Dekker, J. K. Smith and B. E. Roberds, "Chemical Free Room Temperature Wafer To Wafer Direct Bonding," *J. Electrochem. Soc,* vol. 142, no. 11, p. 3949, 1995.

[21] Q.-Y. Tong and U. Gösele, "A Model of Low-Temperature Wafer Bonding And Its Applications," *J. Electrochem. Soc.,* vol. 143, no. 5, p. 1773, 1996.

[22] W. P. Maszara, B. Jiang, A. Yamada, G. A. Rozgonyi, H. Baumgart and A. J. R. d. Kock, "Role of surface morphology in wafer bonding," *Journal of Applied Physics,* vol. 69, no. 1, p. 257–260, 1991.

[23] Q.-Y. Tong, "Thickness Considerations in Direct Silicon Wafer Bonding," *J. Electrochem. Soc.,* vol. 142, no. 11, p. 3975, 1995.

[24] J. Dyson and W. Hirst, "The True Contact Area Between Solids," *Proc. Phys. Soc. B,* vol. 67, no. 4, p. 309–312, 1954.

[25] A. Sanz-Velasco, P. Amirfeiz, S. Bengtsson and C. Colinge, "Room Temperature Wafer Bonding Using Oxygen Plasma Treatment in Reactive Ion Etchers With and Without Inductively Coupled Plasma," *J. Electrochem. Soc.,* vol. 150, no. 2, p. G155, 2003.

[26] J. N. Israelachvili, Intermolecular and Surface Forces, Burlington: Elsevier Science, 2011.

[27] H. D. Ackler, R. H. French and Y.-M. Chiang, "Comparisons of Hamaker Constants for Ceramic Systems with Intervening Vacuum or Water: From Force Laws and Physical Properties," *Journal of Colloid and Interface Science,* vol. 179, no. 2, pp. 460-469, 1996.

[28] D. B. Asay and S. H. Kim, "Evolution of the Adsorbed Water Layer Structure on Silicon Oxide at Room Temperature," *J. Phys. Chem. B,* vol. 109, no. 35, p. 16760–16763, 2005.

[29] V. Larrey, G. Mauguen, F. Fournel, D. Radisson, F. Rieutord, C. Morales, C. Bridoux and H. Moriceau, "Adhesion Energy and Bonding Wave Velocity Measurements," *ECS Transactions,* vol. 75, no. 9, pp. 145-152, 2016.

[30] M. J. Matthewson and H. J. Mamin, "Liquid Mediated Adhesion of Ultra-Flat Solid Surfaces," *MRS Proc.,* vol. 119, p. 87, 1988.

[31] N. Tas, T. Sonnenberg, H. Jansen, R. Legtenberg and M. Elwenspoek, "Stiction in surface micromachining," *J. Micromech. Microeng.,* vol. 6, no. 4, pp. 385-397, 1996.

[32] A. W. Adamson and A. P. Gast, Physical chemistry of surfaces, New York: Wiley, 1997.

[33] J. Haneveld, N. R. Tas, N. Brunets, H. V. Jansen and M. Elwenspoek, "Capillary filling of sub-10nm nanochannels," *Journal of Applied Physic,* vol. 104, no. 1, p. 014309, 2008.

[34] B. Mielniczuk, T. Hueckel and M. S. E. Youssoufi, "Evaporation-induced evolution of the capillary force between two grains," *Granular Matter,* vol. 16, no. 5, p. 815–828, 2014.

[35] J. Desomberg, F. Fournel, H. Moriceau, A. Roule, E. Barthel and F. Rieutord, "Influence of water diffusion in deposited silicon oxides on direct bonding of hydrophilic surfaces," *Microsystem Technologies,* vol. 24, pp. 801-808, 2018.

[36] F. Fournel, V. Larrey, F. Rieutord, C. Morales, C. Bridoux, G. Mauguen and S. Lobo, "Impact of Multiple Debonding on Adhesion Energy," *ECS Transactions,* vol. 86, no. 5, pp. 49-53, 2018.

[37] D. Feijoó, Y. J. Chabal and S. B. Christman, "Silicon wafer bonding studied by infrared absorption spectroscopy," *Appl. Phys. Lett.,* vol. 65, no. 20, p. 2548–2550, 1994.

[38] M. K. Weldon, Y. J. Chabal, D. R. Hamann, S. B. Christman, E. E. Chaban and L. C. Feldman, "Physics and chemistry of silicon wafer bonding investigated by infrared absorption spectroscopy," *J. Vac. Sci. Technol. B,* vol. 14, no. 4, p. 3095, 1996.

[39] J.-P. Gallas, J.-M. Goupil, A. Vimont, J.-C. Lavalley, B. Gil, J.-P. Gilson and O. Miserque, "Quantification of Water and Silanol Species on Various Silicas by Coupling IR Spectroscopy and in-Situ Thermogravimetry," *Langmuir,* vol. 25, no. 10, p. 5825–5834, 2009.

[40] S. Y. Venyaminov and F. G. Prendergast, "Water (H2O and D2O) Molar Absorptivity in the 1000–4000 cm−1Range and Quantitative Infrared Spectroscopy of Aqueous Solutions," *Analytical Biochemistry,* vol. 248, no. 2, p. 234–245, 1997.

[41] C. M. Chiang, B. R. Zegarski and L. H. Dubois, "First observation of strained siloxane bonds on silicon oxide thin films," *J. Phys. Chem.,* vol. 97, no. 27, p. 6948–6950, 1993.

[42] E. K. Plyer, "Infrared Spectra of Methanol, Ethanol, and n-Propanol," *Journal of Research of the National Bureau of Standards (NIST),* vol. 48, 1952.

[43] R. A. Lemons and C. F. Quate, "Acoustic microscope—scanning version," *Appl. Phys. Lett.,* vol. 24, no. 4, p. 163–165, 1974.

[44] H. G. Tattersall, "The ultrasonic pulse-echo technique as applied to adhesion testing," *J. Phys. D: Appl. Phys.,* vol. 6, no. 7, p. 819–832, 1973.

[45] B. W. Drinkwater, R. S. Dwyer-Joyce and P. Cawley, "A study of the interaction between ultrasound and a partially contacting solid—solid interface," *Proc. R. Soc. Lond. A,* vol. 452, no. 1955, p. 2613–2628, 1996.

[46] R. S. Dwyer-Joyce, B. W. Drinkwater and C. J. Donohoe, "The measurement of lubricant–film thickness using ultrasound," *Proc. R. Soc. Lond. A,* vol. 459, no. 2032, p. 957–976, 2003.

[47] A. Hunter, R. Dwyer-Joyce and P. Harper, "Calibration and validation of ultrasonic reflection methods for thin-film measurement in tribology," *Meas. Sci. Technol.,* vol. 23, no. 10, p. 105605, 2012.

[48] M. Tedjini, F. Fournel, H. Moriceau, V. Larrey, D. Landru, O. Kononchuk, S. Tardif and F. Rieutord, "Interface water diffusion in silicon direct bonding," *Applied Physics Letters,* vol. 109, no. 11, p. 111603, 2016.

[49] F. Rieutord, S. Tardif, I. Nikitskiy, F. Fournel, M. Tedjini, V. Larrey, C. Bridoux, C. Morales, D. Landru and O. Kononchuk, "Water Transport Within Silicon Direct Bonding Gap," *ECS Transactions,* vol. 86, no. 5, pp. 39-47, 2018.

[50] S. Mack, H. Baumann and U. Gösele, "Gas development at the interface of directly bonded silicon wafers: investigation on silicon-based pressure sensors," *Sensors and Actuators A: Physical,* vol. 56, no. 3, p. 273–277, 1996.

[51] C. Duan, R. Karnik, M.-C. Lu and A. Majumdar, "Evaporation-induced cavitation in nanofluidic channels," *Proc. Natl. Acad. Sci.,* vol. 109, no. 10, pp. 3688-3693, 2012.

[52] N. R. Tas, P. Mela, T. Kramer, J. W. Berenschot and A. v. d. Berg, "Capillarity Induced Negative Pressure of Water Plugs in Nanochannels," *Nano Lett.,* vol. 3, no. 11, p. 1537–1540, 2003.

[53] B. Bao, S. Zandavi, H. Li, J. Zhong, A. Jatukaran, F. Mostowfi and D. Sinton, "Bubble nucleation and growth in nanochannels," *Phys. Chem. Chem. Phys.,* vol. 19, no. 12, pp. 8223-8229, 2017.

[54] X. X. Zhang and J.-P. Raskin, "Low-temperature wafer bonding: a study of void formation and influence on bonding strength," *J. Microelectromech. Syst.,* vol. 14, no. 2, p. 368–382, 2005.

[55] K. M. Davis and M. Tomozawa, "Water diffusion into silica glass: Structural changes in silica glass and their effect on water solubility and diffusivity," *Journal of Non-Crystalline Solids,* vol. 185, no. 3, p. 203–220, 1995.

[56] R. H. Doremus, "Oxidation of silicon by water and oxygen and diffusion in fused silica," *J. Phys. Chem.,* vol. 80, no. 16, p. 1773–1775, 1976.

[57] S. M. Sze and K. K. Ng, Physics of semiconductor devices, Hoboken: Wiley-Interscience, 2007.

[58] A. Zouine, O. Dersch, G. Walter and F. Rauch, "Diffusivity and Solubility of Water in Silica Glass in the Temperature Range 23-200C," *Phys. Chem. Glasses: Eur. J. Glass Sci. Technol. B,* vol. 48, no. 2, p. 85–91, 2007.

[59] S. A. Campbell, "Thermal Oxidation," in *Fabrication Engineering at the Micro- and Nanoscale*, New York, Oxford University Press, 2013, pp. 74-106.

[60] C. Vogt, K. Laihem and C. Wiebusch, "Speed of sound in bubble-free ice," *Journal of Acoustical Society of America,* vol. 124, no. 6, pp. 3613-3618, 2008.

[61] B. V. Antohe and D. B. Wallace, "The determination of the speed of sound in liquids using acoustic resonance in piezoelectric tubes," *Meas. Sci. Technol.,* vol. 10, pp. 994-998, 1999.

[62] O. Cramer, "The variation of the specific heat ratio and the speed of sound in air with temperature, pressure, humidity, and CO2 concentration," *Journal of the Acoustical Society of America,* vol. 93, no. 5, pp. 2510-2516, 1993.

[63] A. Picard, R. S. Davis, M. Gläser and K. Fujii, "Revised formula for the density of moist air (CIPM-2007)," *Metrologia,* vol. 45, no. 2, pp. 149-155, 2008.

[64] C. Wang, Y. Liu and T. Suga, "A Comparative Study: Void Formation in Silicon Wafer Direct Bonding by Oxygen Plasma Activation with and without Fluorine," *ECS Journal of Solid State Science and Technology,* vol. 6, no. 1, pp. 7-13, 2016.

[65] A. F. M. Leenaars, J. A. M. Huethorst and J. J. V. Oekel, "Marangoni drying: A new extremely clean drying process," *Langmuir,* vol. 6, no. 11, p. 1701–1703, 1990.

[66] I.-S. Chang and J.-H. Kim, "Development of clean technology in wafer drying processes," *Journal of Cleaner Production,* vol. 9, no. 3, p. 227–232, 2001.

[67] K. E. Petersen, "Silicon as a mechanical material," *Proc. IEEE,* vol. 70, no. 5, p. 420–457, 1982.

[68] D. L. Smith, Thin-Film Deposition: Principles and Practice, Boston: McGraw-Hill, 1995.

[69] S. Vincent, I. Radu, D. Landru, F. Letertre and F. Rieutord, "A model of interface defect formation in silicon wafer bonding," *Appl. Phys. Lett.,* vol. 94, no. 10, p. 101914, 2009.